RTCVD synthesis of carbon nanotubes and their wafer scale integration into FET and sensor processes

Thesis presented to apply for the degree of Doctor in Electronic Engineering
at the Universitat Autònoma de Barcelona

by,

Iñigo Martín Fernández

Instituto de Microelectrónica de Barcelona
Centro Nacional de Microelectrónica
IMB-CNM (CSIC)

Philippe Godignon

(Advisor)

Research Professor

Instituto de Microelectrónica de Barcelona
Centro Nacional de Microelectrónica
IMB-CNM (CSIC)

David Jiménez Jiménez

(University tutor)

Associate Professor

Universitat Autònoma de Barcelona
UAB

Editor: Consejo Superior de Investigaciones Científicas (CSIC)

RTCVD synthesis of carbon nanotubes and their wafer scale integration into FET and sensor processes / by Iñigo Martín Fernández – Cerdanyola del Vallès / Consejo Superior de Investigaciones Científicas (CSIC) and Universitat Autònoma de Barcelona (UAB), 2010. Thesis

Cover design: Iñigo Martín Fernández
Front cover photo:
SEM image of an array of multi-walled carbon nanotubes / @ Jordi Llobet Sixto
Back cover photos:
SEM image of carbon nanotubes and zeolite crystals / @ Iñigo Martín Fernández
SEM image of a passivated carbon nanotube transistor / @ Xavier Borrisé Nogué
Optical image of a carbon nanotube modified electrode / @ Iñigo Martín Fernández

Philippe Godignon, Research Professor at the *Instituto de Microelectrónica de Barcelona – Centro Nacional de Microelectrónica* (IMB-CNM, CSIC)

CERTIFIES:

That the thesis entitled “RTCVD synthesis of carbon nanotubes and their wafer scale integration into FET and sensor processes” was carried out by Mr. Iñigo Martín Fernández under his supervision within IMB-CNM.

Cerdanyola del Vallès, September 2010.

Prof. Philippe Godignon

A mi bici y mi aventurero,
por nuestras viejas andanzas
y por las que quedan por llegar

Agradecimientos

Cuando hablé por primera vez con Philippe Godignon y me preguntó qué me parecía lo que me estaba planteando, creo que le dije algo así como que bien, que trabajaría para conseguirlo. Y trabajando trabajando hemos ido llegando. Por lo que he aprendido a su lado y por todo con lo que he compartido con él aparte de los nanotubos (y del grafeno) tiene y tendrá todo mi afecto.

Pero si bien he tenido un director, he tenido la suerte de contar con otros dos padrinos, el Prof. Francesc Pérez y el Prof. Emilio Lora, que me han transmitido su experiencia, que siempre se han preocupado de que me encuentre en las mejores condiciones y con los que he pasado, y también me han hecho pasar, momentos entrañables y muy divertidos. Muchas gracias a los dos.

Además he tenido otros acompañantes. Los principales han sido el Dr. Narcis Mestres, con su "otro método", la Dra. Mª José Esplandiú, con sus consejos, sus ánimos y su energía, la Dra. Gemma Gabriel, con su interés y toda su ayuda, y la Dra. Gemma Rius con la que compartí los tramos más abruptos del recorrido. Y, por supuesto, esta tesis no habría sido posible sin los que "han trabajado para mí": todo el personal de las Salas Blancas sin los que sólo la mitad del trabajo se habría completado; los mecánicos y el personal de mantenimiento que solucionaron todos los contratiempos con el equipo de los nanotubos; los que me ayudaron con la encapsulación y, sobre todo, los que me ayudaron tanto con la caracterización eléctrica y electroquímica. A todos ellos y al resto del personal del CNM, muchas gracias por tratarme tan bien.

Por otro lado, de estos años van a ser inolvidables los *brainstormings* con los Prof. Avelino Corma y Hermenegildo García (que fueron más bien tempestades) e, indudablemente, también lo serán los meses que pasé en Hsinchu, en el grupo del Dr. Ting, por lo bien que me acogieron, porque la experiencia fue fascinante, y porque nunca acumularé tantas fotos de otro viaje como de aquellos pocos meses en Taiwan.

Pero aparte de los nanotubos estos años han sido mucho más. He sido Iñigo, i-ñigo, iñi, iñaki, el de amarillo, Yushchenko, Argiñano, el independentista, rojo... y alguna cosa más que... y todo ha dado lugar a momentos memorables.

Por un lado, creo que fui muy afortunado al "aterrizar" en el despacho E1-12. Sólo espero haber devuelto algo de todo lo que he recibido de los que ocuparon y ocupan aquel espacio (aunque sea sólo un poco ya será mucho). Y también creo que he sido muy afortunado con la generación CNM con la que me ha tocado vivir (Sergio, Irene, Guillermo, Giordano, Nuria, Neus, Olga, Juan Pablos, Javi, Rafa, Jorge, Gemma…), porque son muy buena gente y por todo lo que me han hecho pasar. Con ellos he vivido muchos de los momentos más divertidos, tristes, especiales e intensos de estos años en el día a día dentro del CNM, en congresos, durante escapadas, entre cervezas, en fiestas y en muchos otros actos sociales.

Y también he sido muy afortunado "fuera del CNM"; por vivir en lugares característicos de BCN y por compartirlos con amigos como Ibai y Cedric (y también con Juantxo), por re-encontrarme con viejos

amigos y por hacer muchos otros nuevos (los Erasmus, los barceloninos, los diseñadores, los donostiarras,…). Había Imaginado muchas cosas antes de venir a Barcelona pero con esta *troupe* cualquier previsión previa quedó sobradamente superada hace mucho tiempo.

Para terminar, quiero darles las gracias a Miguel y a Coro, a Coro y a Miguel, a los *aitas*, porque ellos me han ayudado y encauzado para que llegue a ser lo que soy, a Elena porque los hermanos se quieren mucho aunque no se lo digan todos los días, y a Laura, por nuestra gran aventura y por las que queden por llegar.

Cerdanyola del Vallès, septiembre de 2010

Contents

Motivation

Carbon nanotubes (CNTs) are tubular molecules which diameters may be smaller than one nanometre and which walls are formed of single carbon atoms layers that are arranged in a honey comb lattice. Because of their high aspect ratio, they may be considered as one-dimensional materials since their length is typically in the order of the micrometers, in combination with their properties, which are conferred by their structural arrangement, CNTs are a very attractive material for a wide range of applications.

In the frame of micro- and nanotechnology, CNTs have been demonstrated to be very promising for the fabrication of devices and systems for nanoelectronics, sensors or NEMS. However, standardised processes for their fully controlled synthesis and their successful integration into those systems are still challenging.

Objective

This thesis was conceived to advance on the wafer scale integration of CNTs into micro- and nanodevices. The work that is presented in this document deals with process engineering, device design, device fabrication and device characterization. Two major goals have been pursued:

- To acquire the knowhow on the synthesis of CNTs by rapid thermal chemical vapour deposition (RTCVD) to develop recipes to synthesize certain in structure CNTs and certain in morphology CNT arrays.
- The wafer scale integration of CNTs into devices with different functionalities and technological processes by conventional fabrication processes.

The work was mainly performed at the *Instituto de Microelectrónica de Barcelona* (IMB-CNM, CSIC)[*]. This is the first thesis at the Institute to be fully devoted to CNTs and to cover from CNT synthesis optimization to CNT based device design, fabrication and characterization.

Structure of the document

This document is divided in four sections which are sub-divided in 10 chapters. The first section is introductory and the others summarise the work that has been developed on the optimization of the synthesis of CNTs and on their wafer scale integration. The general conclusions of the work are presented just afterwards. Finally, two annexes, on the scientific production and on other devices that are being developed are included at the end of the document.

The introductory section aims, on the one side, to introduce CNTs, what CNTs are been used for and which are the main challenges on their integration into micro- and nanodevices (Chapter 1), and, on the other side, to describe the experimental methods that are used along the document (Chapter 2).

[*] Henceforth, IMB-CNM, IMB or CNM are used without distinction to refere to IMB-CNM, CSIC.

The section on the optimization of the CVD synthesis of CNTs summarizes the acquired expertise on the synthesis of CNTs by thermal CVD when using different catalyst materials. This section is divided in three chapters.

- Chapter 3 introduces the CVD synthesis mechanism of CNTs and the main parameters that need to be taken into account when designing a process.
- Chapter 4 addresses the optimization of the CVD synthesis of CNTs by materials based on conventional CNT catalysts, and studies the constricted in diameter and directed in orientation growth of single-walled CNTs by microporous crystals.
- Chapter 5 is devoted to the optimization of the CVD synthesis of CNTs based on non-conventional CNT catalysts, in particular, platinum. This chapter serves also to introduce the synthesis of a CNT-graphene composite.

The section on the wafer scale integration of single CNT devices presents the results that have been attained on the fabrication of devices based on CNT-transistor-like structures. This section is divided in three chapters.

- Chapter 6 briefly reviews the electrical characteristics of the CNTs and that of the CNT field effect transistor (CNT-FET) and the state of the art and challenges on their fabrication.
- Chapter 7 is devoted to the development of a process based on conventional steps for the wafer scale fabrication of tens of thousands of CNT-FET structures and for the development of a procedure for their automatic testing and statistical evaluation.
- Chapter 8 presents an upgrade of the process in Chapter 7 for the fabrication of (bio)electrochemical sensors based on CNT-FETs. This upgrade includes a passivation procedure so that the CNTs are the only element of the sensor to be depassivated.

The section on the wafer scale integration of high densities of CNTs deals with the modification of previously reported devices for bio-sensing applications by the integration CNTs on their electrodes. This section is divided in two chapters.

- Chapter 9 overviews the most relevant aspects on the (bio-)electrochemical sensing with devices based on electrodes and the improvements that CNTs may confer to these devices.
- Chapter 10 presents the bio-sensing devices where the CNTs are to be integrated, describes the CNT integration process, analyses the mechanical, electrical and electrochemical characteristics of the CNT modified electrodes and compares them with those from the previously developed electrodes.

The author's contribution to the work

Unless somehow remarked, the author is responsible for every task that is described in this document. In particular:

- CNT synthesis: the author is responsible for every CVD process, characterization and discussion related to CNT synthesis except for the preparation of some of the catalyst materials, TEM, EDX, XRD and some of the SEM characterizations. Researchers from the *Instituto de Tecnología Química* (ITQ, CSIC) were responsible for the preparation of the ferrocene, ferritin and the platinum based particles, as well as for the synthesis of the zeolite

crystals. Dr. Gemma Gabriel was responsible for the synthesis of the magnetite particles. Dr. Maria José Esplandiu from the *Centre d'Investigació Nanociència i Nanotecnologia* (CIN2-CSIC) gave support on the preparation of the ferric nitrate based solutions. Raman characterization of the CNTs was supervised by Dr. Narcis Mestres from the Institut de *Ciència de Materials de Barcelona* (ICMAB). Prof. Jyh-Hua Ting and Prof. Philippe Godignon supervised every task at the National Nano Device Laboratories (NDL) at Taiwan, and at CNM, respectively.

- Single CNT applications: the author is responsible for the design, for the optimization of the non-conventional fabrication steps, for the supervision of the whole fabrication processes and for the characterization of the devices. The E-beam lithographic process was optimised together with Dr. Xavier Borrisé. Mr. Marc Sansa is responsible for the programme for the automatic testing. Prof. Philippe Godignon, Prof. Emilio Lora-Tamayo and Prof. Francesc Perez-Murano supervised the design, the fabrication and the characterization of the devices.

- High density of CNT applications: the author is responsible for the optimization of the CNT integration process into the devices from the *Grupo de Aplicaciones Biomédicas* (GAB) at CNM and for their mechanical, electrical and electrochemical characterization. Manipulation of the probes in the Focus Ion Beam system to measure the conductivity of the CNT modified electrodes was done by Mr. Jordi Llobet. Researchers from GAB supported the electrochemical measurements. The fabrication was supervised by Prof. Philippe Godignon and the characterization Prof. Philippe Godignon together with Dr. Gemma Gabriel.

Research projects

Reported in this document experiments were developed in the frame of three main projects: CRENATUN, SENSONAT and a joint project between CNM and NDL. The author also contributed to 4 projects from different GICSERV calls to access the Integrated Micro and Nano Cleanroom facility of CNM.

- CRENATUN (*Crecimiento unidireccional de nanotubos de carbono para su integración en dispositivos y circuitos electrónicos*), Ref. 200550F0151, lasted from 2005 to 2008. The project aimed to demonstrate the viability of growing CNTs using meso- and micro- structured materials to achieve oriented CNTs in a way that would be compatible with CMOS processes. The project was led by CNM and also involved researchers from ITQ and ICMAB.

- SENSONAT (*Sensores y electrodos basados en nanotubos de carbono*), Ref. NAN2004-09306-C05-01, lasted from 2005 to 2009. The objective of this project was to explore the possibility of fabricating new nanotechnological concepts and to contribute to the development and pre-industrialization of electronic devices with living organisms and biological systems interface. The project was led by CNM and also involved researchers from ICMAB, *Universitat Autònoma de Barcelona* (UAB), *Universitat Rovira i Virgili* (URV) and *Universidad Miguel Hernandez* (UMH).

- The project entitled "Near Ohmic Contact Between Metal Electrodes and Single-Wall Carbon Nanotubes Grown with Nickel Silicide Catalysts", Ref. 2007TW0005, lasted from 2008 to 2009. Its objective was to investigate and to develop ohmic contacts between metallic electrodes and synthesized by CVD single-walled CNTs. This project was developed by CNM together with NDL, the National Central University (NCU) and Chia Yi University (NCYU), all of them at Taiwan.

Financial support

The Author acknowledges the financial support that he received from CRENATUN and the I3P action through a postgraduate (I3P-BPG2005) and a pre-doctorate (I3P-BPD-2006) grants.

Scientific production

Developed tasks have, until now, led to the publication of 6 peer reviewed articles and 3 conference proceedings, and to the presentation of 22 contributions to national and international conferences, 7 of which being oral presentations. Refer to Annex 1 for a detailed description of the scientific production.

SECTION 1:
INTRODUCTORY SECTION

Index of Section 1

1
Brief introduction to carbon nanotubes

Carbon nanotubes (CNTs) are an allotrope of carbon just as amorphous carbon, diamond, fullerenes or graphene. A CNT is a tubular structure which walls are formed of carbon atoms that are arranged in a honeycomb lattice structure.

CNTs came to prominence in 1991 after the paper of Sumio Iijima on the formation helical carbon structures [1]. Since then, big efforts have been devoted to explore their exceptional properties and to demonstrate different applications (Figure 1.1). As scientists will take advantage of these properties and will develop standardised CNT synthesis processes and CNT based technologies, CNTs may become an important building block of the future nanosciences and nanotechnologies.

Figure 1.1: Journal covers on different advances related to CNTs.

1.1 Types of carbon nanotubes

CNTs are usually understood as the rolling of a graphene sheet, which is a monolayer of carbon atoms that are arranged in a sp^2 configuration (Figure 1.2-a). The distance between 2 neighbour carbon atoms on this lattice, $a_{c\text{-}c}$, is 1.42 Å. CNTs are classified in two groups depending on the number of walls they are formed of. Thus, a CNT is single-walled (SW) or multi-walled (MW) if it is formed of a single layer (Figure 1.2-b and Figure 1.2-c) or of more than one concentric layers (Figure 1.2-d to Figure 1.2-f), respectively.

1.1.1 Single-walled carbon nanotubes

The diameter of a SWCNT can range between 0.42 Å [4] and ~2 nm and its length may reach up to several tens of millimetres [5]. The structure of a SWCNT is determined by the way the graphene sheet rolls to form the tube, which is called the chiral vector (C_h) (Figure 1.3-a). This vector can be

represented by a pair of indexes (n,m) that denote the number of unit vectors along two directions in the honeycomb crystal lattice of graphene. Then, $C_h=n\cdot a_1+m\cdot a_2$. SWCNTs are classified according to these (n,m) indexes (Figure 1.3-b): if m=0, the SWCNT is named “zig-zag”, if m=n the SWCNT is identified as “armchair” and, for the other cases, the SWCNT is labelled as “chiral”. The properties of a SWCNT, specially their electronic structure, depend on their structure. (The electronic structure of the SWCNTs is reviewed in chapter 7.)

1.1.2 Multi-walled carbon nanotubes

As they have been defined above, MWCNTs are CNTs that are formed by more than one coaxial rolled graphene sheets. The distance between two of these layers is 3.4 Å, though it may slightly vary depending on the number of layers the MWCNT is formed of. The diameter of a MWCNT can be as small as 1.1 nm and as big as several tens of nanometres.

MWCNTs are often classified according to their graphitization. Thus, if the walls of a MWCNT are parallel to the axis, the CNT will be labelled as a MWCNT (Figure 1.2-e) but, if its walls are not completely parallel to the CNT axis, it will be identified as a bamboo like MWCNTs (Figure 1.2-f).

1.2 Properties of carbon nanotubes

The 1D aspect ratio of the CNTs in combination with the ordered structure of their walls, confer to them exceptional properties. For example, regarding their electrical characteristic, MWCNTs are metallic and SWCNTs can behave as metallic or semiconducting depending on their chirality (the electrical properties of CNTs are discussed in Chapter 6). For detailed descriptions on the properties of the CNTs refer to references [7, 8].

1.3 Synthesis of carbon nanotubes

CNTs are usually synthesised either by arc discharge, laser ablation or chemical vapour deposition (CVD).

- Arc discharge consists in applying a discharge between two electrodes so that the graphitic material on one of them sublimates to form the CNTs [9]. This technique can be optimised for the synthesis of SW and MWCNTs but normally results, also, in the synthesis of other CNT allotropes
- Laser ablation consists in vaporising the graphitic material from an electrode by a pulsed laser in an inert gas ambient and may result in the synthesis of SW and MWCNTs depending on the composition of the electrode [10]. Laser ablation is the technique that results in the CNTs that are most perfect in structure.
- CVD synthesis of CNTs is based on the decomposition of a carbon containing gas and its restructuration at a particle that acts as the catalyst. Hence, the catalyst particle is mandatory for the synthesis to take place. Furthermore, the structure of the catalyst particle determines the structure of the CNT to be synthesised. This particularity of CVD synthesis of the CNTs is of significance because it implies that the structure of the CNT can be tuned by controlling the structure of the catalyst particle it grows from, and because a selective deposition of the catalyst particle results in the selective synthesis of the CNT. For a detailed description of the CVD growth mechanism by CVD refer to Chapter 3.

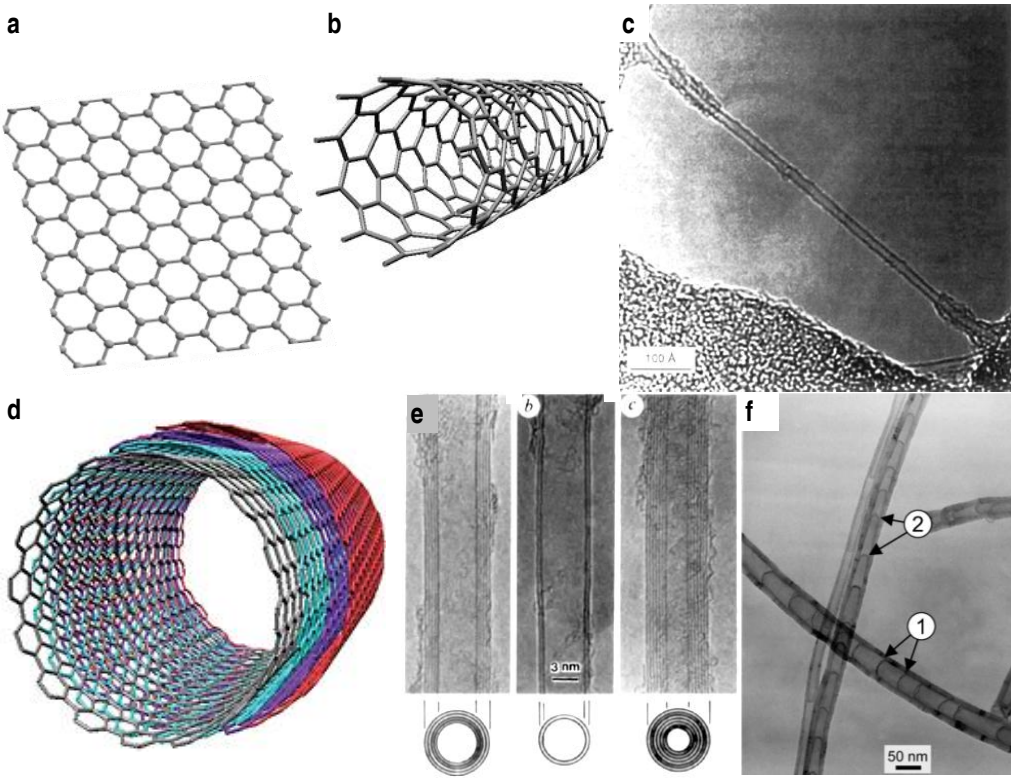

Figure 1.2 (a) Schematic of a graphene sheet. (b-c) Schematic and TEM image of a SWCNT. (d-f) Schematic of a MWCNT and TEM image of different diameter MWCNTs and of bamboo like MWCNTs, respectively. Scale bars in (c), (e) and (f) are 100 Å, 3 nm and 50 nm, respectively. TEM images in (c), (e) and (f) extracted from [2], [1], [3], respectively.

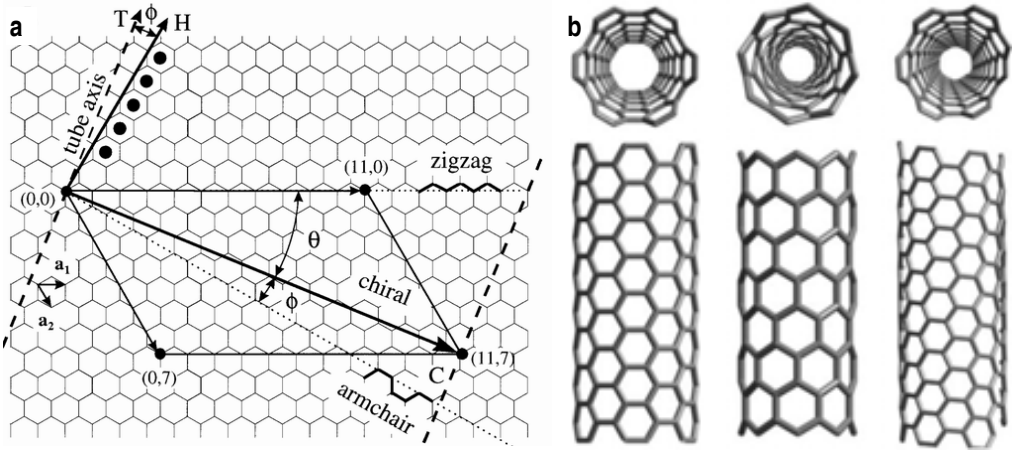

Figure 1.3: (a) Representation of the chiral vector on the graphene honeycomb lattice (extracted from [6]). (b) schematics of the three possible SWCNT morphologies: armchair (n=m), zig-zag (m=0) and chiral (n≠m, m≠0).

1.4 Applications

Most relevant applications in the frame of this thesis are those where CNTs are investigated for electronics, medicine or chemistry applications, in particular, those involving the fabrication of micro and nanodevices.

Interest on CNTs for nanoelectronics started in 1998 when the transistor effect was first observed on a single CNT [11, 12]. Since then, big efforts have been devoted to optimise the fabrication of these devices. Now, the fabrication of prototypes of IC circuits based on semiconducting SWCNTs is possible [13]. Actual CNT field effect transistors (CNT-FET) exhibit transport properties that are comparable and even superior to those of the metal-oxide semiconductor (MOS)FET that is used as the building block of most of the current electronics [14]. Thus, the CNT-FET may be considered as a very promising alternative to replace the MOSFET when its scaling would not be possible any more [15]. Additionally, their optical characteristics make of the semiconducting SWCNTs a very attractive material for the integration of optic applications on the electronics. On the other side, the integration of metallic SWCNTs and MWCNTs, which can carry very high current densities, is being explored for interconnections.

Integration of CNTs into devices for biology has demonstrated, for example, that CNTs may boost the electrical signals from neurons [16, 17]. However, a big controversy arises on the use of CNTs for certain bio-applications since the bio-compatibility of CNTs has not been resolved yet [18, 19]. In this sense, as electrical transport on CNTs is very sensitive to ambient conditions and as they can be easily functionalised and doped, CNT based sensors can be fabricated so that they are made selective for the detection of a chemical [20] or for biodetection [21, 22].

Besides, CNTs are extensively used for the fabrication of NEMS as, because of their dimensions and of their structure, they exhibit superior capacities as oscillators [23, 24] and for the fabrication of other structures such as nanomotors [25, 26]. For example the highest mass resolution was achieved with a mass spectrometer based on a double-walled CNT [24]. But apart from these, other actuators such as memory cells [27] or MEMS based on a 3D patterning of very dense CNT layers [28] have also been demonstrated. Another promising field for CNTs is their use as field emitters for the fabrication of displays [29].

Perspective

Regarding the nanotechnologies, even if prototypes have been demonstrated for diverse applications, the fabrication of the devices is still challenging because of two main hints that need to be overcome.

The first challenge is the standardised synthesis of the CNTs, since now it is not possible to assure growth of a certain structure SWCNT or that of a MWCNT with precise inner and outer diameters. In this sense, the development of procedures to sort the CNTs according to their structure [30, 31] and observing that under some particular synthesis conditions the chirality of the SWCNTs can be somehow adjusted [32, 33] are encouraging.

The second challenge concerns CNT positioning on a surface. Even if different procedures are being tested and that some have already been demonstrated, as for CNT synthesis, there is still no standard procedure to control the location of both edges of the CNTs at wafer level when different orientations of the CNTs are required. This problem has been partially solved by the directed growth of the CNTs on quartz substrates and by developing device architectures based on arrays of CNTs, but it is still problematic when the location of single CNTs needs to be controlled.

Consequently, a big effort is still needed to fully understand CNT synthesis and to improve CNT integration. As it has been above pointed out, based on recent studies, controlling the structure of a CNT may become feasible by CVD in the near future and, additionally, CVD is the CNT synthesis technique which is the most compatible with the integration of CNTs. In the next years we will witness if the great potentials of CNTs can finally be transferred to the fabrication of devices.

References

1. S. Iijima, Helical Microtubules of Graphitic Carbon, Nature, 1991. **354**(6348): p. 56-58.
2. D.S. Bethune, C.H. Kiang, M.S. Devries, G. Gorman, R. Savoy, J. Vazquez, and R. Beyers, Cobalt-Catalyzed Growth of Carbon Nanotubes with Single-Atomic-Layerwalls, Nature, 1993. **363**(6430): p. 605-607.
3. C.J. Lee, S.C. Lyu, Y.R. Cho, J.H. Lee, and K.I. Cho, Diameter-controlled growth of carbon nanotubes using thermal chemical vapor deposition, Chemical Physics Letters, 2001. **341**(3-4): p. 245-249.
4. N. Wang, Z.K. Tang, G.D. Li, and J.S. Chen, Single-walled 4 angstrom carbon nanotube arrays, Nature, 2000. **408**(6808): p. 50-51.
5. X. Wang, Q. Li, J. Xie, Z. Jin, J. Wang, Y. Li, K. Jiang, and S. Fan, Fabrication of Ultralong and Electrically Uniform Single-Walled Carbon Nanotubes on Clean Substrates, Nano Letters, 2009. **9**(9): p. 3137-3141.
6. J.W.G. Wildoer, L.C. Venema, A.G. Rinzler, R.E. Smalley, and C. Dekker, Electronic structure of atomically resolved carbon nanotubes, Nature, 1998. **391**(6662): p. 59-62.
7. M. Meyyappan, *Carbon nanotubes: science and applications*. 2005, New York: CRC Press LLC.
8. A. Jorio, G. Dresselhaus, and M.S. Dresselhaus, Carbon Nanotubes: Advanced Topics in the Synthesis, Structure, Properties and Applications. 2008, New York: Springer.
9. C. Journet, W.K. Maser, P. Bernier, A. Loiseau, M. Lamy de la Chapelle, S. Lefrant, P. Deniard, R. Lee, and J.E. Fischer, Large-scale production of single-walled carbon nanotubes by the electric-arc technique, Nature, 1997. **388**(6644): p. 756-758.
10. W.K. Maser, E. Muñoz, A.M. Benito, M.T. Martínez, G.F. De La Fuente, Y. Maniette, E. Anglaret, and J.L. Sauvajol, Production of high-density single-walled nanotube material by a simple laser-ablation method, Chemical Physics Letters, 1998. **292**(4-6): p. 587-593.
11. R. Martel, T. Schmidt, H.R. Shea, T. Hertel, and P. Avouris, Single- and multi-wall carbon nanotube field-effect transistors, Applied Physics Letters, 1998. **73**(17): p. 2447-2449.
12. S.J. Tans, A.R.M. Verschueren, and C. Dekker, Room-temperature transistor based on a single carbon nanotube, Nature, 1998. **393**(6680): p. 49-52.
13. Z.H. Chen, J. Appenzeller, Y.M. Lin, J. Sippel-Oakley, A.G. Rinzler, J.Y. Tang, S.J. Wind, P.M. Solomon, and P. Avouris, An integrated logic circuit assembled on a single carbon nanotube, Science, 2006. **311**(5768): p. 1735-1735.
14. P. Avouris, Z.H. Chen, and V. Perebeinos, Carbon-based electronics, Nature Nanotechnology, 2007. **2**(10): p. 605-615.
15. International Technology Roadmap Semiconductor, www.itrs.net
16. E.W. Keefer, B.R. Botterman, M.I. Romero, A.F. Rossi, and G.W. Gross, Carbon nanotube coating improves neuronal recordings, Nature Nanotechnology, 2008. **3**(7): p. 434-439.
17. G. Cellot, E. Cilia, S. Cipollone, V. Rancic, A. Sucapane, S. Giordani, L. Gambazzi, H. Markram, M. Grandolfo, D. Scaini, F. Gelain, L. Casalis, M. Prato, M. Giugliano, and L. Ballerini, Carbon

nanotubes might improve neuronal performance by favouring electrical shortcuts, Nature Nanotechnology, 2009. **4**(2): p. 126-133.

18. C.A. Poland, R. Duffin, I. Kinloch, A. Maynard, W.A.H. Wallace, A. Seaton, V. Stone, S. Brown, W. MacNee, and K. Donaldson, Carbon nanotubes introduced into the abdominal cavity of mice show asbestos-like pathogenicity in a pilot study, Nature Nanotechnology, 2008. **3**(7): p. 423-428.

19. S.Y. Hong, G. Tobias, K.T. Al-Jamal, B. Ballesteros, H. Ali-Boucetta, S. Lozano-Perez, P.D. Nellist, R.B. Sim, C. Finucane, S.J. Mather, M.L.H. Green, K. Kostarelos, and B.G. Davis, Filled and glycosylated carbon nanotubes for in vivo radioemitter localization and imaging, Nature Materials, 2010. **9**(6): p. 485-490.

20. J. Kong, N.R. Franklin, C.W. Zhou, M.G. Chapline, S. Peng, K.J. Cho, and H.J. Dai, Nanotube molecular wires as chemical sensors, Science, 2000. **287**(5453): p. 622-625.

21. M.T. Martínez, Y.C. Tseng, N. Ormategui, I. Loinaz, R. Eritja, and J. Bokor, Label-free DNA biosensors based on functionalized carbon nanotube field effect transistors, Nano Letters, 2009. **9**(2): p. 530-536.

22. Z.C. Sanchez-Acevedo, J. Riu, and F.X. Rius, Fast picomolar selective detection of bisphenol A in water using a carbon nanotube field effect transistor functionalized with estrogen receptor-α, Biosensors and Bioelectronics, 2009. **24**(9): p. 2842-2846.

23. D. Garcia-Sanchez, A.S. Paulo, M.J. Esplandiu, F. Perez-Murano, L. Forro, A. Aguasca, and A. Bachtold, Mechanical detection of carbon nanotube resonator vibrations, Physical Review Letters, 2007. **99**(8): p. art. no. 085501

24. K. Jensen, K. Kim, and A. Zettl, An atomic-resolution nanomechanical mass sensor, Nature Nanotechnology, 2008. **3**(9): p. 533-537.

25. A.M. Fennimore, T.D. Yuzvinsky, W.-Q. Han, M.S. Fuhrer, J. Cumings, and A. Zettl, Rotational actuators based on carbon nanotubes, Nature, 2003. **424**(6947): p. 408-410.

26. A. Barreiro, R. Rurali, E.R. Hernandez, J. Moser, T. Pichler, L. Forro, and A. Bachtold, Subnanometer Motion of Cargoes Driven by Thermal Gradients Along Carbon Nanotubes, Science, 2008. **320**(5877): p. 775-778.

27. J.E. Jang, S.N. Cha, Y.J. Choi, D.J. Kang, T.P. Butler, D.G. Hasko, J.E. Jung, J.M. Kim, and G.A.J. Amaratunga, Nanoscale memory cell based on a nanoelectromechanical switched capacitor, Nature Nanotechnology, 2008. **3**(1): p. 26-30.

28. Y. Hayamizu, T. Yamada, K. Mizuno, R.C. Davis, D.N. Futaba, M. Yumura, and K. Hata, Integrated three-dimensional microelectromechanical devices from processable carbon nanotube wafers, Nature Nanotechnology, 2008. **3**(5): p. 289-294.

29. K.A. Dean, A new era: Nanotube displays, Nature Photonics, 2007. **1**(5): p. 273-275.

30. M.S. Arnold, A.A. Green, J.F. Hulvat, S.I. Stupp, and M.C. Hersam, Sorting carbon nanotubes by electronic structure using density differentiation, Nature Nanotechnology, 2006. **1**(1): p. 60-65.

31. A. Nish, J.-Y. Hwang, J. Doig, and R.J. Nicholas, Highly selective dispersion of single-walled carbon nanotubes using aromatic polymers, Nature Nanotechnology, 2007. **2**(10): p. 640-646.

32. A.R. Harutyunyan, G. Chen, T.M. Paronyan, E.M. Pigos, O.A. Kuznetsov, K. Hewaparakrama, S.M. Kim, D. Zakharov, E.A. Stach, and G.U. Sumanasekera, Preferential Growth of Single-Walled Carbon Nanotubes with Metallic Conductivity, Science, 2009. **326**(5949): p. 116-120.

33. W.H. Chiang and R.M. Sankaran, Linking catalyst composition to chirality distributions of as-grown single-walled carbon nanotubes by tuning NixFe1-x nanoparticles, Nature Materials, 2009. **8**(11): p. 882-886.

2
Experimental methods

The work presented in this thesis deals with the integration of CNTs into silicon planar technologies. These technologies consist in selectively adding and/or removing layers to/from the surface of a wafer, typically silicon, in order to have a certain device fabricated. Developed tasks involved CNT synthesis optimization, CNT integration into device fabrication and device fabrication and characterization.

This chapter is divided in two main sections. The first section is devoted to CNT synthesis and device fabrication whereas the second section is devoted to CNT metrology and device testing.

2.1 Carbon nanotube synthesis and device fabrication

This section describes the capabilities that were used for the fabrication of the devices. Special attention is given to the description of the CVD systems that were used for CNT synthesis optimization.

2.1.1 Carbon nanotube synthesis

CNT synthesis was the process to be most performed and optimised during the period of this thesis. Chemical Vapour Deposition (CVD) was used as the CNT growth procedure because it is one of the best known synthesis techniques and, mainly, because it allows selective growth of specific in structure CNTs directly on a substrate.

A CVD process consists in depositing on a surface a material that is the resultant of the reaction between different gas reactants under specific conditions, for example, thermal, pressure or plasma conditions. CVD growth mechanism of CNTs is discussed in detail in Chapter 3.

Two different CVD systems were employed for CNT growth, both of the systems being thermal CVDs.

A) JetStar 100ST Rapid Thermal CVD

The JetStar 100ST is a CVD system from Jipelec. This was the system to be mainly used during the thesis period. Pictures of the system are shown in Figure 2.1-a,b. The RTCVD system is installed at the *Laboratori d'Ambient Controlat* (LAC) of the UAB [1].

This RTCVD was not intended for CNT synthesis. Therefore, it had to be modified (new gas lines had to be installed) to perform CNT growth. The RTCVD technique and, in particular, this RTCVD system, differs from the usually used in research systems for CNT synthesis on two main characteristics [2].

First difference is that this system is "rapid thermal". This implies that heating is not achieved by means of resistances but by means of infrared lamps, which makes the heating and cooling of the samples much faster. This characteristic allowed the study of synthesis parameters such as the temperature ramp and catalyst activation in a way that is not possible by a conventional thermal CVD

system. However, because of the heating strategy, processes should not last more than 10 minutes at synthesis temperature to prevent the system from being damaged.

Second, whereas typically used for CNT synthesis chambers are 2 inch in diameter quartz tubes, the chamber of the JetStar 100ST allows processing up to 4 inch wafers. This characteristic of the CVD is very important since it made compatible CNT synthesis with the other microfabrication processes that were performed at CNM's clean room.

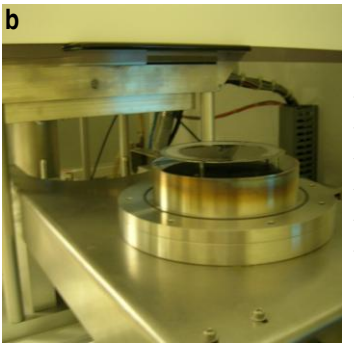

c

Max. temp	1200ºC
Max. heating	30ºC/s
Max. vacuum	10^{-6} Torr
Gases	CH_4, H_2, N_2O, SiH_4, Ar, N_2
Sample size	Up to 4" wafers

Figure 2.1: Pictures of (a) the JetStar 100ST RTCVD system and (b) detail of the chuck. (c) Table summarizing the main specifications of the system.

The main characteristics of the RTCVD system are listed in Figure 2.1-c. The silane (SiH_4) and nitrous oxide (N_2O) are primitive gas lines for silicon and silicon oxide growth and deposition. These gases were not used in the CNT synthesis processes in this document.

B) EasyTube ET1000

The EasyTube *ET1000* from FirstNano (Figure 2.2-a) is a typical in configuration, used for CNT synthesis, atmospheric thermal CVD system. It consists of a 2 inch in diameter horizontal quartz tube that is heated by means of resistances that are located along it. The main characteristic of this system is that it incorporates the possibility of applying an electric field to direct growth of the CNTs by means of two metallic needles. The specifications of this systems are listed in Figure 2.2-b. This CVD is installed at the National Chiao Tung University's (NTCU) Nano Facility Center [3].

b

Max. temp	950ºC
Max. heating	~ 1ºC/s
Max. vacuum	Atmospheric
Gases	CH_4, $C2H_4$, H_2, NH_3, Ar, N_2
Sample size	Up to 2 x 2 cm^2 chips
Capacity to grow aligned CNTs	Yes

Figure 2.2: (a) Picture of the EasyTube ET1000 system. The inset shows the 2 inch quartz chamber, the quartz sample holder and a silicon chip before the CVD process. (b) Summary the main specifications of the system.

2.1.2 Micro- and nanofabrication of devices

Devices were fabricated in clean room environment. Main fabrication took place at CNM's Integrated Micro and Nanofabrication Clean Room (ICTS) [4]. Some fabrication processes also took place at LAC. Samples involved in the project with Taiwan were fabricated at NDL's Clean Room facilities.

A) IMB-CNM's Integrated Micro and Nanofabrication clean room

IMB-CNM's clean room, which is 1,500 m^2, has the capability of fabricating CMOS integrated circuits and includes specific for microsystems and nanofabrication processes. The clean room is divided in rooms that are class 100 or class 1,000. Standard wafer diameter at the time the Thesis was developed was 4 inch.

The Clean Room and its complementary laboratories, the Device Packaging Laboratory and the Electrical Characterization Laboratory, form the Micro and Nanofabrication Clean Room which is recognized as one of the "Singular Scientific and Technological Infrastructures" (ICTS) by the Spanish Government.

During this thesis most of the used standard clean room fabrication process steps were performed under the *comanda* state. This means that the processes were performed by clean room staff under the supervision of the author. Non standard processes were developed and performed by the author. Used processes are listed during the descriptions of the CNT synthesis and device fabrication schemes.

B) UAB's Laboratori d'Ambient Controlat facility

UAB's Cleanroom facility, LAC, is the ancient clean room of CNM. The facility is 173 m^2. Main fabrication capabilities of the laboratory consist of a mask aligner, a spinner, six furnaces, three benches, a RIE, a PECVD and a RTCVD.

The RTCVD equipment was the main system to be used for CNT synthesis. The photolithography capabilities, the benches, the RIE system and some of characterization equipments were mainly used for the CNT catalyst material preparation, deposition and patterning.

C) NDL's clean room facilities

This facility has a total extension of 3,500 m^2. The facility is divided in three rooms which are class 10, class 100 and class 10,000 respectively. NDL facilities are complemented by NCTU's Nanofabriction Facility Center which was the previous NDL fabrication facility. The author performed the processes on the catalyst preparation, on the synthesis of the CNT and supervised the rests of the process steps.

2.2 Carbon nanotube and device characterization

The characterization techniques have been divided in two groups: the techniques used to observe the CNTs and the techniques used to evaluate the fabricated devices. Unless otherwise stated, the equipments were manipulated by the author.

2.2.1 CNT metrology

CNT synthesis was normally evaluated by means of Scanning Electron Microscopy (SEM), Atomic Force Microscopy (AFM) and/or Raman Spectroscopy (Raman). Other techniques were also used occasionally to assess specific characteristics of the growth process.

A) Scanning Electron Microscopy

SEM was the most often used technique to evaluate CNT synthesis. SEM imaging is quick and non destructive. However, SEM imaging at high energies has been demonstrated to generate defects on the walls of the CNTs and, thus, to decrease the Raman signal [5, 6].

A LEO 1530 SEM microscope that had been complemented for lithographic means with a RAITH ELPHY PLUS controller and software was used for CNT characterization. This SEM was equipped with two secondary electron detectors: an in-lens detector and a conventional secondary electron detector. A JSM-6500F SEM microscope from JEOL was used during the internship at NDL. This system included back-scattered and secondary-electron detectors. Samples up to six inch could be entered in both systems.

Under some specific SEM conditions (for low accelerating voltages) and if CNTs are in contact with a silicon oxide substrate, they are highlighted because of substrate discharging around them. This characteristic was very useful, for example, when low densities of CNTs were synthesized on silicon oxide substrates (Figure 2.3). This way, although they appear to be quite thick, the diameters of the SWCNTs in the images are not larger than 2 nm.

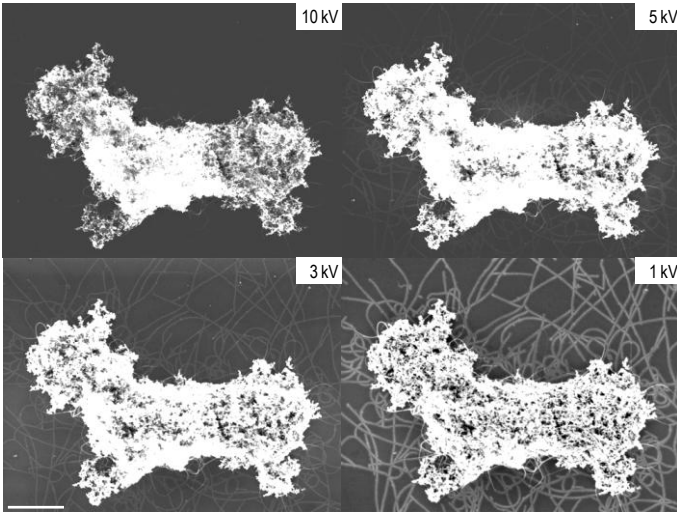

Figure 2.3: Set of SEM images of synthesized on silicon oxide SWCNTs. The doggy shaped volume is the catalyst material the SWCNTs grew from. Th e SWCNTs in contact with the substrate become more visible as the accelerating voltage is diminished. Scale bar is 1µm. The image at 1 kV was awarded with an Honourable Mention at Micro Nano Graph Contest that was held during the 35th International Conference on Micro & Nano Engineering (MNE09) [7].

B) Atomic Force Microscopy

Atomic Force Microscopy (AFM) was most used to evaluate the distribution, the length and the diameter of the synthesized CNTs. Regarding the measurement of the diameter of the CNTs, it must be noticed that AFM does not serve to get their exact diameter but an approximated one (typically ±0.2 nm). Profile measurements will depend on the measurement conditions (especially on the tip pressure on the CNT) and also on the roughness of the sample the CNT is deposited on.

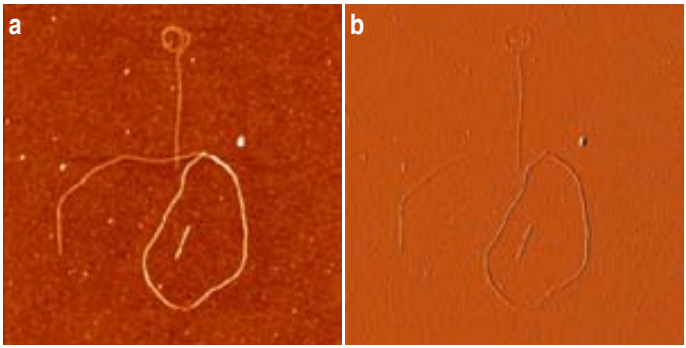

Figure 2.4: (a) Topographic and (b) amplitude AFM images of three SWCNTs. The SWCNTs had been synthesized on a silicon oxide substrate out of iron based catalyst particles by CVD. X,Y: 5 µm; Z: 2.5 nm (a), 300 mV (b).

Installed at the ICTS of IMB AFM system is from Veeco. The AFM system consisted of a Nanoscope IV controller and Dimension 3100 head. The AFM was usually operated in tapping mode and topographic and amplitude images were normally recorded.

The topographic and the amplitude AFM images in Figure 2.4-a,b show the synthesis of three SWCNTs out of iron particles on a silicon oxide substrate. The diameters of the SWCNTs were measured to be between 0.6 and 0.8 nm. Sections equals to 1.3 nm were measured where the SWCNTs had rolled (top and right side sections).

C) Raman Spectroscopy

Raman spectroscopy lays on the inelastic scattering of monochromatic light produced by vibrational, rotational, and other low-frequency modes in a system. The laser light interacts with phonons or other excitations in the system, resulting in the energy of the laser photons being shifted up or down. It is a non destructive, quick and easy to implement technique.

Raman spectroscopy of CNTs has been demonstrated to be a very powerful tool for their characterization [8]. Representative spectra of SW- and MWCNTs are shown in Figure 2.5. Although the observed resonances are similar to those from other allotropes of carbon, they serve to identify CNTs univocally. Moreover, in the case of SWCNTs, resonances can even be related to their atomic structure. The most relevant resonance peaks are:

- **G resonance peak**: This peak appears on every CNT at frequencies around ~1,585 cm^{-1}. On SWCNTs, the G peak is double and the separation between the two peaks depends on the electric characteristic of the SWCNT. The G peak on MWCNTs is unique and broader than on SWCNTs peak.
- **Radial Breathing Mode (RBM) resonance peak**: This resonance mode is characteristic of SWCNTs even if it may also be observed on very few layers MWCNTs. It appears at frequencies lower than 600 cm^{-1}. This resonance is associated to a coherent vibration of the carbon atoms in the radial direction, as if the CNT was “breathing”. The inset on the left in Figure 2.5 shows the resonances in the RBM from a high amount of SWCNTs. The RBM frequency of a SWCNT can be related to its diameter and, moreover, to its (n,m) indexes [9].
- **Disorder peak (D)**: This resonance peak is indicative of defects on the walls of the CNT and of amorphous carbon deposition. It appears at frequencies around 1350 cm^{-1}.
- **G’ peak** (also known as 2D): This peak, which appears around 2700 cm^{-1}, is a second order resonance peak of D peak. It is indicative of the graphitization of the walls of the CNTs.

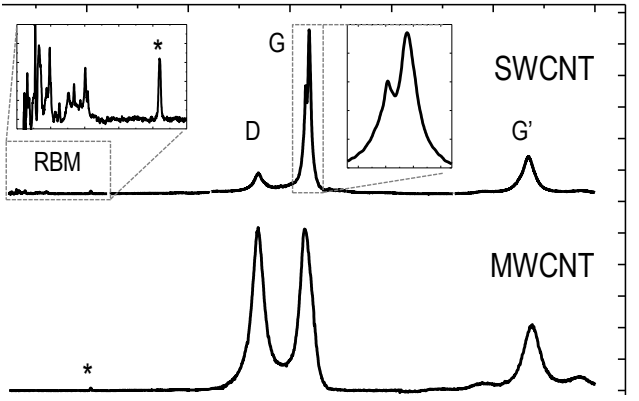

Figure 2.5: Raman spectra of SWCNTs and MWCNTs showing the most relevant Raman resonant peaks.The peaks that are marked with an asterisk are related to the silicon form the substrate.

A Horiba Ivon Jobin T64000 Raman system was employed to perform the Raman analyses. The red (647.1 nm) and green (514.5 nm) laser lines the ones to most often used in the experiments. Laser spot size was usually set to 1 μm in diameter. The laser power on the sample was set depending on the density of CNTs on the sample. If CNT density was low, laser power on the sample was normally set between 1 and 2 mW. On the contrary, if CNT density was high, laser power on the sample was set bellow 1 mW, typically between 0.75 and 0.9 mW.

D) Other CNT characterization techniques

Apart from SEM, AFM and Raman spectroscopy, X-ray spectroscopy, Transmission Electron Microscopy (TEM) and Energy Dispersive X-ray spectroscopy (EDX) were also used to evaluate the nickel silicide phase CNTs grow from (sectionr 4.4), to observe the structure of the synthesized CNTs (section 5.2) and to assess the composition of the CNT composite (section 5.3), respectively.

Used TEM systems, a Hitachi H-7000 and a JEOL JEM-2011, were installed at the Servei de Microscòpia of the UAB [10]. Installed at NDL X-ray diffraction system was a X'Pert PRO MRD from PANanalytical. EDX measurements were performed with a LEO 1530 SEM system that is installed at the Electron Microscopy Lab at ICMAB [11]. These equipments were not operated by the author.

2.2.2 Device characterization

Device fabrication steps were validated using standard procedures such as optical microscopy, SEM, AFM, ellipsometry or 4-point measurements. This section, however, does not present these techniques but those that were used to evaluate the characteristics of the fabricated devices. In addition, it only focuses on the techniques that the author used in his experiments.

A) Electrical characterization

The electrical characterization of a device consists in measuring its electrical characteristics when an electrical excitation is applied. Two different probe systems and parameter analyzers are used in the next chapters.

The first setup is used in chapters 7 and 8 for the electrical characterization of the wafer scale fabricated CNT-FET devices. The setup consisted in a semiautomatic PA200 system from SÜSS Microtech and a 41000 Series Integrated Parametric Analysis and Characterization Environment from

Agilent. The system from Agilent included a module to place a probe card (B2220A), a commutation matrix with 24 pins (B2201A), 4 SMUs (B2201A) and a semiconductor parameter analyzed (4284A).

The second setup is used to evaluate the resistance of a CNT layer that had been grown perpendicular to the surface of the sample (Chapter 10). As the probes had to be positioned in a very controlled way to avoid any damage on the CNT layer, the probes that are installed inside CNM's FIB system (a 1560XB Cross Beam FIB system from Zeiss) had to be used. Electrical measurements were performed with a B1500A semiconductor analyser from Agilent. The FIB system was operated by the process engineer.

B) Electrochemical characterization

Electrochemistry is a branch of chemistry that deals with the study of the interfacial charge transfer processes at a system [12, 13]. Electroimpedance spectroscopy and cyclic voltammetry are used in Chapter 10 for the study of the CNT modified electrodes.

(i) Impedance spectroscopy

Electrochemical impedance spectroscopy was used to measure the frequency response of the CNT modified electrodes to compare them with previously developed electrodes.

Impedance measurements were conducted using a commercial impedance analysis system (SI 1260 from Solartron Analytical). A physiological saline solution (0.9% sodium chloride, with a nominal resistivity of 71.3 Ωcm at 298 K) and a commercial platinum electrode were used as the solution and as the reference electrode, respectively. Independent measurements were conducted for each electrode couple, recording the impedance modulus and phase at several discrete frequencies. The excitation signal was designed to be similar to the one that would be recorded or that would be used to stimulate a tissue. It consisted in a 100 mV AC signal (V_{DC}=0V) that increased from 10Hz to 100 kHz.

(ii) Cyclic voltammetry

Cyclic voltammetry is based on the measurement of the current response to a potential waveform with a triangular aspect that is applied to an electrode. This technique is usually used to analyze redox reactions though, the measurements in chapter 10 were performed with no species in the solution to calculate the capacitance of the CNT modified electrodes.

Cyclic voltammetry measurements were performed with a microAutolab Type III potentiostat galvanostat instrument from Metrohm Autolab. A silver wire and a commercial platinum electrode were used as the reference and the auxiliary electrodes, respectively. Physiological saline solution (0.9 % sodium chloride, with a nominal resistivity of 71.3 Ωcm at 298 K) was used in the experiments.

References

1. Laboratori d'Ambient Controlat-UAB, http://www.uab.es/l-ambient-controlat.
2. S. Wolf and R.N. Tauber, Silicon Processing for the VLSI Era, Vol. 1: Process Technology: Lattice Press.
3. Nano Facility Center - National Chiao Tung University, http://www.nfc.nctu.edu.tw/english/index.htm.
4. Integrated Micro and Nanofabrication Facility - Instituto de Microelectrónica de Barcelona, http://www.icts.cnm.es.
5. B.W. Smith and D.E. Luzzi, Electron irradiation effects in single wall carbon nanotubes, Journal of Applied Physics, 2001. **90**(7): p. 3509-3515.
6. S. Suzuki, K. Kanzaki, Y. Homma, and S.Y. Fukuba, Low-acceleration-voltage electron irradiation damage in single-walled carbon nanotubes, Japanese Journal of Applied Physics, Part 2: Letters, 2004. **43**(8 B): p. L1118-L1120.
7. 35th International Conference on Micro & Nano Engineering (MNE'09), http://www.mne09.org.
8. M.S. Dresselhaus, A. Jorio, M. Hofmann, G. Dresselhaus, and R. Saito, Perspectives on Carbon Nanotubes and Graphene Raman Spectroscopy, Nano Letters, 2010. **10**(3): p. 751-758.
9. A. Jorio, R. Saito, J.H. Hafner, C.M. Lieber, M. Hunter, T. McClure, G. Dresselhaus, and M.S. Dresselhaus, Structural (n, m) determination of isolated single-wall carbon nanotubes by resonant Raman scattering, Physical Review Letters, 2001. **86**(6): p. 1118-1121.
10. Servei de Microscòpia - Universitat Autònoma de Barcelona, http://sm.uab.es/
11. Electron Microscopy Lab - Institut de Ciència de Materials de Barcelona, http://www.icmab.es/icmab/scientific-technical-services/electron-microscopy-lab.html
12. A.J. Bard and L.R. Faulkner, *Electrochemical Methods: Fundamentals and Applications*. 2001, New York: John Wiley & Sons.
13. V.S. Bagotsky, *Fundamentals of electrochemistry*. 2006, Hoboken: John wiley & Sons.

SECTION 2:
OPTIMIZATION OF THE SYNTHESIS OF CARBON NANOTUBES BY RTCVD

Achieving control over CNT synthesis is the first step towards the fabrication of CNT based devices. In this sense, this section summarizes the acquired expertise in the frame of CNT synthesis.

Chemical vapour deposition (CVD) is the technique that was selected for CNT synthesis since it allows growth of the CNTs directly on the surface of the sample and since it is the technique that is most compatible with device micro- and nanofabrication. Among the different CVD techniques, thermal CVD was selected as the most appropriate one to achieve the synthesis of the desired in structure CNTs for the planned applications.

At this point, it has to be remarked that the aim of the developed tasks was not to perform fundamental studies on the CNT synthesis mechanisms, which are still under discussion, but to investigate a set of methods for the wafer scale synthesis of different in structure CNTs so that they could be integrated into the novel devices that are described in the next sections.

This section, then, summarises the acquired expertise on the wafer scale synthesis of CNTs when using different conventional and non-conventional CNT catalyst materials. Moreover, directed growth of the CNTs is addressed by the application of an electric field and by the use of microporous materials and a CNT-graphene composite is pesened.

Index of Section 2

3
Synthesis of carbon nanotubes by CVD techniques

CVD is, among the most extended techniques for CNT synthesis, the only technique that allows the synthesis of CNTs directly on a substrate. Furthermore, as a catalyst particle needs to be involved in the growth of the CNTs, by the pre-deposition of the catalyst particles at selective locations on the substrate, the selective synthesis of the CNTs may be achieved. This particularity of the CVD synthesis of CNTs is of great interest as it allows CNTs to be directly integrated into the fabrication of micro- and nano- devices.

Besides this device fabrication concern, the most important characteristic about CVD synthesis of CNTs is that, by controlling the structure (size and composition) of the catalyst material, CNTs with controlled diameter and structure may be grown if the CVD conditions are optimised. However, there are still many unknown aspects related to CNT synthesis that need to be elucidated before total control over the synthesis process is attained.

This chapter reviews briefly the CNT growth mechanism as it is nowadays understood and some strategies to achieve a controlled synthesis of CNTs. A final section has been included as a prospective.

3.1 Carbon nanotube growth mechanism

CNT synthesis is a very complex process since it relies on reactions that are still not perfectly understood. Attaining control over the synthesis of the CNTs requires the optimization of a large number of parameters that involve from the catalyst formation and deposition on the samples prior to CNT growth, to the removal of the process gases once the growth of the CNTs has finished.

This section reviews CNT growth mechanism and the parameters that govern CNT synthesis: the catalyst particle, the gases that are involved in the process and the conditions at which the reactions take place.

3.1.1 CNT growth scheme

CNTs may grow according to two different schemes: tip-growth and base-growth (Figure 2.3) [1]. In both cases, a catalyst nanoparticle is first introduced into the chamber. Then, a carbon feed is furnished and, when the particle is saturated with carbon, the CNT starts to grow. If the nanoparticle separates from its original position as the CNT grows, growth will be identified as tip-growth, whilst, if the nanoparticle stays in contact with the substrate, growth will be identified as base-growth. The reason for a CNT to grow according to either mechanism is not fully confirmed although it has mainly been attributed to the interaction between the nanoparticle and the substrate [2].

What, at the moment, is still under discussion is the carbon saturation and the CNT beginning to grow mechanisms. Recently, Hofmann and Lin took advantage of their capability to observe CNT growth

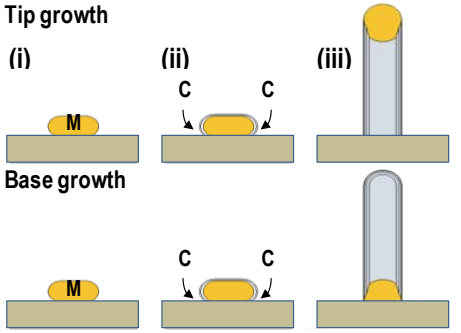

Figure 3.1: Scheme of the CVD growth of a CNT: (i) deposited on the substrate catalyst particle; (ii) the particle catalyzes the formation of a carbon crust; (iii) growth of the CNT.

inside a TEM [3, 4] to demonstrate that the catalyst particle remains crystalline during CNT synthesis and that carbon diffusion takes place at the outer shells of the nanoparticle but not through the bulk material. Additionally, they also observed that different in structure CNTs (SWCNTs and bamboo CNTs) presented very different growth mechanisms (Figure 3.2-a). More recently, Marchand used a field emission microscope to image the growth of SWCNTs [5]. His experiments revealed an atom by atom growth that matched the "Screw Dislocation Model" proposed by Ding (Figure 3.2-b) [6].

3.1.2 The catalyst material

Iron, nickel and cobalt are the metals that are most often used (conventional) as CNT catalysts in CVD processes. It has been demonstrated that the use of a conventional catalyst in combination with optimised parameters of the CVD process can lead to the synthesis for both SW- and MWCNT in any of the different possible layer configurations. This includes, for example, isolated CNTs, spaghetti or forest like configurations. However, despite the fact that CNTs grow out of the iron, nickel or cobalt nanoparticles, it has been demonstrated that addition of other materials such as Pt, Ru or Mo may enhance CNT formation by improving the reaction yield or by decreasing the temperature at which formation takes place [7, 8].

Apart from acting as co-catalyst materials, it has been demonstrated that non conventional metals may also nucleate CNT growth (Figure 3.3-a) [9-12]. It has been suggested that formation of the CNT out of a certain in composition metal particle will depend on the electronic structure of the metal and on its capability to form a stable carbide [9]. Besides metals, synthesis of CNTs out of other materials based nanoparticles, such as silicon carbide, silicon, germanium, alumina, zirconia or even from carbon, has also been demonstrated (Figure 3.3-b) [13-17]. In fact, SWCNT synthesis from another

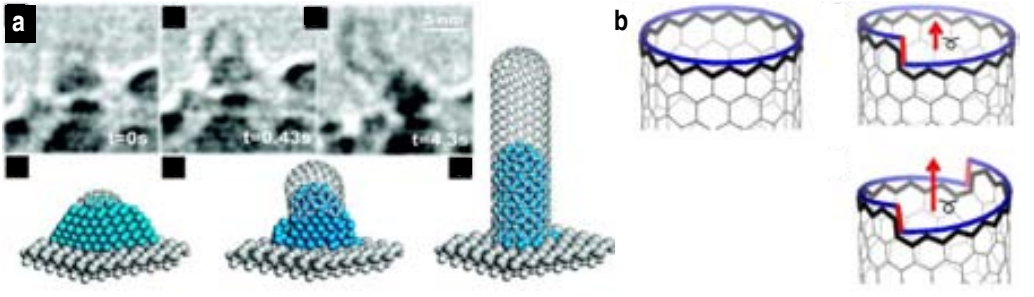

Figure 3.2: (a) TEM image sequence of the base-growth of a nickel catalyzed CNT and schematic of the process according to the recorded images [3]. (b) Screw dislocation growth mechanism of a CNT depending on their chiral structure [6].

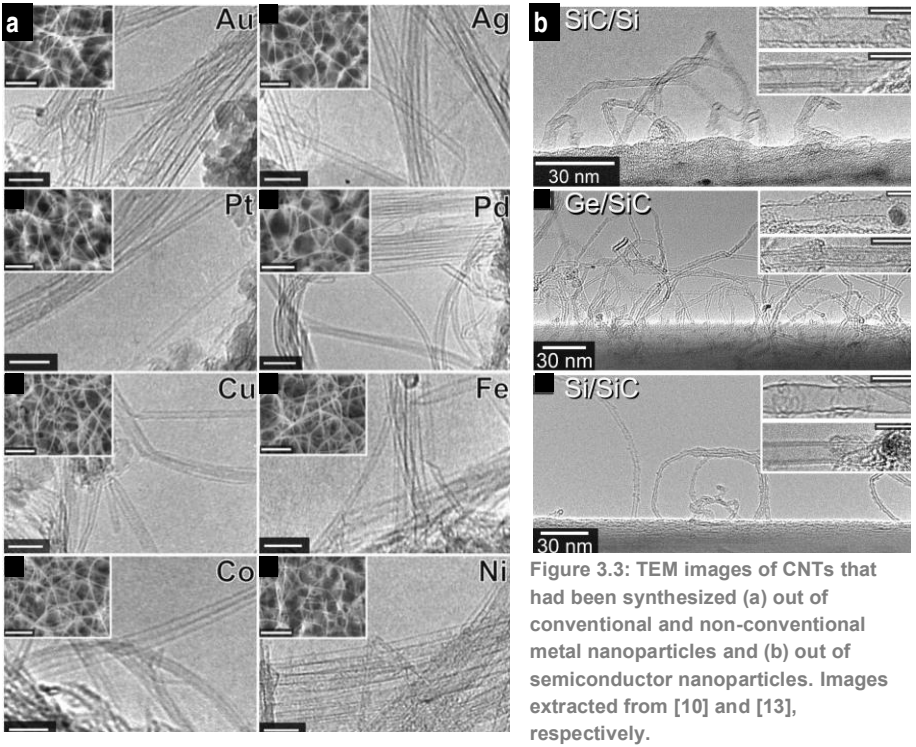

Figure 3.3: TEM images of CNTs that had been synthesized (a) out of conventional and non-conventional metal nanoparticles and (b) out of semiconductor nanoparticles. Images extracted from [10] and [13], respectively.

SWCNT section [18] and synthesis of CNTs on substrates where no catalyst had been deposited has even been reported [19].

Synthesis of CNTs out of such a range of materials opens the possibility to adapt the catalysts for the application the CNTs will be used for. This way, the use of particles which are no-metals could be very useful, for example, for the fabrication of nanoelectronics to avoid metal contamination during fabrication. Similarly, other metals, such as platinum, which is considered bio-compatible, could avoid the use of purification treatments to remove the catalyst particles in bio-sensing applications or could be used in catalysis experiments [20].

The catalyst material is normally deposited on the surface of the sample either from a solution containing catalyst material colloids [10, 12, 13, 21] or by depositing a catalyst layer by means of a vacuum process such as sputtering or evaporation, or by electroplating [22-25].

In the first case, the catalyst material is most often composed of a nitrate or a carbonate and the solution is usually deposited by drop casting or by spin coating. Deposited on the surface salt colloids are reduced by heating or calcination to form an oxide compound that is further reduced with hydrogen or by thermal decomposition to obtain the metallic catalytic islands the CNTs finally grow from. This catalyst deposition procedure is normally used for the deposition of small in diameter particles to achieve synthesis of SWCNTs and, usually, results in an uneven distribution of catalyst particles on the sample.

In the second case, a very high in purity catalyst material layer, typically thinner than 10 nm, is deposited on the surface of the sample. Then, by heating up the sample, the catalyst layer breaks because of the strong cohesive forces and because of the increased surface mobility to form the

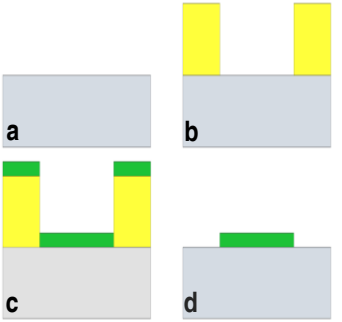

Figure 3.4: Scheme of the local deposition of catalyst material on a sample by means of photolithography. (a) Sample. (b) Patterned sample after a photolithographic process. (c) Deposition of the catalyst material. The material is deposited on the whole surface of the sample. (d) Sample after the lift-off of the catalyst material.

metal aggregate islands the CNTs grow from. The diameter and the distribution of the metal islands depend on the catalyst layer thickness. The thicker the layer, the bigger and more disperse the metal aggregates will be. This catalyst preparation procedure is more scalable, reproducible and compatible with the processes that are usually used in micro- and nanofabrication than the previous one. However, it is more expensive.

The catalyst material can be deposited on the whole surface of the sample or selectively by using a patterning technique [23, 26-28]. The scheme of a local deposition of the catalyst material by means of lithography (positive resist) is shown in Figure 3.4.

3.1.3 CNT synthesis conditions

In combination with the catalyst material, CVD synthesis conditions determine the structure of the CNT to be synthesized. The CVD CNT synthesis process is usually divided in two steps: the catalyst activation step and the CNT growth step. The catalyst activation step consists in increasing the temperature up to the growth temperature as well as in favouring the formation of appropriate in morphology catalyst islands. The CNT growth step is where the CNT synthesis takes place. During this step a carbon containing gas is made to flow into the chamber and the conditions are generated for it to decompose and for the CNTs to grow.

A) Process gases

Different carbon containing gases have been demonstrated for CNT synthesis, being methane (CH_4) [11, 21], acetylene (C_2H_2) [2, 22, 25, 29], ethylene (C_2H_4) [26, 30] and ethanol (C_2H_5OH) [10, 11, 13, 23] the ones to be most often used. The use of one or other gas depends on the desired CNT structure. For example if “best” in structure CNTs are to be synthesized, a gas to synthesize the CNTs at a higher temperature and at a slower growth rate, such as, methane, will be selected [[21]]. On the other hand, if a high CNT growth rate is to be achieved, then acetylene or ethylene will be chosen [30].

Apart from the carbon containing gases, other gases are equally important in the synthesis process. Hydrogen and ammonia are often used to reduce the catalyst material during the catalyst activation step when using iron based or nickel based materials [25]. Hydrogen plays, moreover, an important role as regulator of the carbon feeding process to the catalyst particle. Oxygen [31], water vapour [30] and helium [32] have also been demonstrated to play a similar role during CNT growth step. In the case of water vapour, Hata demonstrated that by injecting a well controlled amount of water vapour during the CNT synthesis step, saturation of the particle can be minimized. SEM image in Figure 3.5 shows that up to 2.5 millimetre height CNT layers may be synthesized for very restrictive substrate, catalyst layer and CVD process setups.

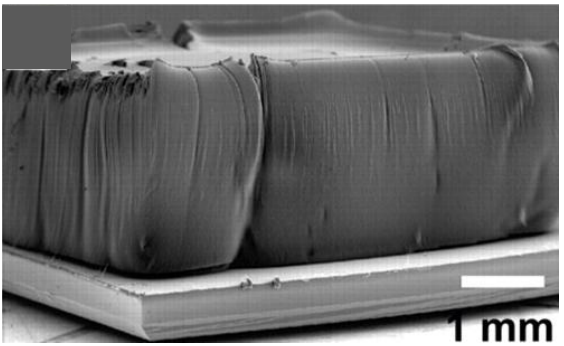

Figure 3.5: Picture of a 2.5 mm-tall SWNT forest on a 7 x 7 mm^2 silicon chip [30].

B) CVD technique

Thermal CVD and Plasma Enhanced (PE)CVD are the two CVD techniques that are most often used in the synthesis of CNTs. Two main differences can be highlighted between both techniques.

First, when plasma contributes to the CNT synthesis reaction, the thermal energy that is required for the reactions to accomplish diminishes and so, growth of the CNTs can take place at lower temperatures. The synthesis of CNTs at lower temperatures, however, implies that the structure of the CNTs to be grown will be less perfect than that of those CNTs that are synthesized at higher temperatures. The suitability of using a PE or a thermal CVD system to grow the CNTs will depend on the application the CNTs are intended for. In the case of SWCNTs to form the channel of a CNT transistor, for example, as very low in defect SWCNTs are desirable, a thermal CVD system will be used for the synthesis.

Second, the electric field that is applied to generate the plasma in the PECVD processes induces an alignment of the synthesized CNTs in the direction of the field [29]. This alignment of the CNTs is different from the alignment that can be achieved when using a thermal method when the catalyst islands are close from each other [22, 30, 33] as vertical alignment of even isolated MWCNTs is achievable. This characteristic of the PECVD method is of interest, for example, in field emission applications.

C) CNT synthesis dependence on the temperature

As it has been mentioned in the previous sections, the temperature at which CNTs are synthesized depends on the gases that are involved in the reaction and on the technique that is used to grow the CNTs. Carbon nano fibre synthesis at temperatures as low as has 120ºC have been reported for a

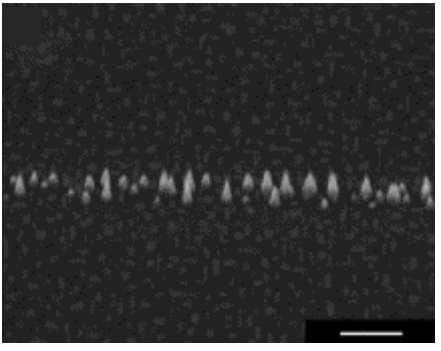

Figure 3.6: SEM image of vertically aligned carbon nanofibers grown with diluted acetylene from e-beam patterned nickel lines at 120 °C. A tilt angle of 40° was used for imaging. Scale bar is 500 nm. [34]

PECVD process involving pre-deposited nickel layers as catalyst material and acetylene and ammonia as process gases [34]. These carbon nano fibres (Figure 3.6) are short MWCNTs that appear to be defective.

3.2 Carbon nanotube synthesis optimization

The fact that the CNT formation process is still not completely understood is hindering CNT integration into devices. The main challenges are related to achieving control over the structure of the synthesized CNTs and achieving control over their positioning on the wafer so that determined in structure CNTs can be integrated into a certain application.

This section is a brief overview on the strategies that can be used to succeed on the synthesis of certain in structure CNTs.

3.2.1 Controlling the structure of the CNTs

Control over the synthesis of either SW- or MWCNTs is achieved by controlling the diameter of the island the CNT grows from. This way, normally, if the catalyst island is smaller than 2 nm, SWCNT synthesis will normally be achieved. On the contrary, if the catalyst island is bigger than 2 nm, a MWCNT will be obtained. The diameter of the catalyst island depends on the morphology of the material that is used as catalyst and on the catalyst pretreatments.

In the case of MWCNTs, their structure can be tuned by changing the CVD conditions. If processes at low temperatures and involving plasma are applied, bamboo-like in structure MWCNTs will be more likely to be synthesized whereas, if high temperature processes are applied, synthesis of higher in wall graphitization MWCNTs will be achieved.

In the case of SWCNTs, tuning their chirality is still under discussion. It has recently been demonstrated that by perfectly controlling the composition of the catalyst material or under certain process gases conditions, the chirality of the SWCNTs can be preselected [32, 35].

3.2.2 Controlling the orientation of the CNTs

Achieving control over the position of one of the edges of a CNT is possible by a selective deposition of the catalyst material. However, achieving control over the other edge of the CNT is not possible unless some strategy is adapted.

Vertical alignment of isolated MWCNTs or of a dense CNT layers (SW or MW) can be achieved if synthesis is performed in a PECVD system [29] or, when thermal processes are applied, if a dense enough distribution of the catalyst particles is deposited [22, 30, 33].

Orientation of the CNT growth in a direction parallel to the substrate has been demonstrated by different methods. It is well established that CNTs can be oriented according to the direction of the process gases during growth [36] or by applying an electric field [37]. One of the most promising alternatives, however, is to grow the CNTs on quartz or on sapphire substrates as, in those cases, levels of alignment can be controlled to better than 0.01° over CNT lengths of up to the millimetre scale [38, 39]. This is due to the fact that CNTs orient along molecular-scale topological grooves that exist in certain directions on the surface of these substrates. However, when CNTs are grown on these substrates, a CNT transfer procedure from those wafers to the wafers where the devices are to be fabricated has normally to be performed. Other approaches that have been discussed are the use of pre-patterned trenches to serve as CNT growth guides [40] and the porosification of pre-patterned silicon to serve as growth orientation guide [41].

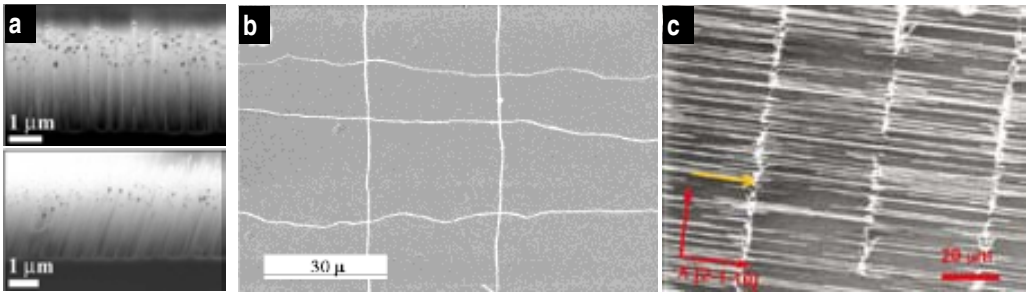

Figure 3.7: (a) Perpendicular to the substrate and tilted growth of MWCNTs by PECVD [29]. (b) Synthesis of oriented SWCNTs by means of the process gases direction in a two step CVD process. SWCNTs growing in one direction were synthesized in a first CVD process and then the sample was turned 90º to perform the second CVD synthesis process [36]. (c) SWCNT synthesis on a quartz substrate [38]. Scale bars are 1, 30 and 20 µm in (a-c) respectively.

Challenges

The fact that control over the structure of the SW and MWCNTs has still not been completely solved is hindering CNT integration into wafer scale fabricated micro- and nanodevices and systems. However, the efforts on the optimization of the catalyst materials will lead to succeed in adjusting CNT synthesis to every application the CNTs are so promising for. Because of the synthesis hitch, other approaches to preselect specific in structure CNTs are being developed. In this sense, separation of SWCNTs by density differentiation [42], which allows differentiating even between different in chirality SWCNTs, is very promising.

Regarding the positioning of the CNTs on the substrates, their orientation in a determined direction has already been resolved. However, now it is not possible to grow CNTs that are oriented in different directions on a same CVD process and at wafer level. At the moment, the only technique that allows positioning the CNTs according to any direction is dielectrophoresis [43]. This technique is, however, limited for high integration and complex in structure device fabrication as a magnetic field needs to be generated locally at each position where the CNTs are to be deposited.

4
Optimization of the RTCVD synthesis of carbon nanotubes by conventional catalyst materials

The first step for the development of a CNT based technology is to achieve control over their synthesis. CVD was selected to accomplish these tasks because of its benefits for controlling the structure of the CNTs and their position on the sample.

This chapter focuses on CNT synthesis optimization when using conventional CNT catalyst materials, that is, iron, nickel and cobalt. These materials are known as conventional because of their proved capacity for CNT synthesis and because they are the materials that are most often used. The chapter is divided in four blocks.

The first block of the chapter is devoted to the understanding of the CNT synthesis process. In this section, iron nitrate particles are used as catalyst material. Developed tasks deal with catalyst preparation and deposition and with CVD conditions to achieve growth of CNTs on different types of samples.

The second block deals with the study of other particles based on iron as possible catalyst materials. The aim of this section is to evaluate if other iron based catalysts could be used to achieve the synthesis of similar in and/or different structure CNTs than in the previous chapter.

The third block is devoted to analyse the possibility of using microstructured crystals to solve the problems related to controlling the structure of SWCNTs and their growth direction.

The last block addresses the synthesis of directed CNTs between pre-patterned catalyst islands out of a nickel silicide compound as a route to improve the CNT-metal contact.

4.1 Carbon nanotube RTCVD synthesis by ferric nitrate

The first developed tasks were related to the understanding of the CNT synthesis process and to evaluate the possibility of growing different in structure CNTs by the RTCVD technique. These studies were accomplished by using ferric nitrate as CNT catalyst material.

Ferric nitrate was selected as catalyst material because it is based on iron (a conventional CNT catalyst material) and because it is one of the most commonly used iron based CNT catalyst materials [21, 44]. Ferric nitrate is not, however, the material the CNTs grow from. When the catalyst solution is prepared, the iron nitrate particles decompose and the iron reacts with oxygen in the environment to form iron oxide particles. Afterwards, these particles are normally further reduced in a hydrogen environment during the first stages of the CVD process and then used to nucleate CNT growth.

The results that are presented in this block were used to address the optimization of the CNT catalyst solution preparation and deposition on the substrate, the study of the influence of the catalyst morphology and the RTCVD parameters on the structure of the obtained CNTs, and checking CNT growth on different materials that are frequently used in micro- and nanofabrication.

4.1.1 Catalyst solution preparation and deposition on silicon oxide substrates

Catalyst solution recipe is similar to that reported by Hafner [44]. In order to prepare a 100 ppm solution, typically, 4 mg of ferric nitrate (Iron (III) nitrate nonahydrate; 99.99% trace metals basis; Ref.: 254223; Aldrich) were diluted in 40 ml of isopropyl alcohol. For the solution to be homogeneous, it was shacked for several minutes. The catalyst solution was prepared each time the catalyst was going to be deposited to avoid the formation of colloids because of the solution storage. The catalyst material was kept in a dessicator to prevent its degradation.

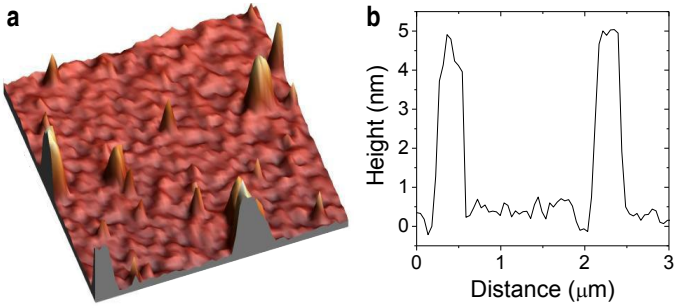

Figure 4.1: Topographic AFM image of iron nitrate particles deposited on a silicon oxide substrate. (a) 3D image of a 850 nm x 850 nm area. Z: 10 nm. (b) Profile of two 4 nm in diameter catalyst particles.

Figure 4.1 shows AFM images of iron nitrate particles deposited on a silicon oxide substrate. Figure 4.1-a is a topographic 3D image of an 850 nm x 850 nm area were several particles had been deposited. The biggest particles correspond to particle aggregates. Figure 4.1-b is a topographical section of two 4 nm catalyst particles. Deposited catalyst particles were typically between 2 and 6 nm in diameter though bigger aggregates, such as the ones in Figure 4.1-a, were occasionally observed. Measured particle diameters are in correspondence with the reported in literature diameters [44].

Two different catalyst deposition approaches were analyzed: drop casting and spin coating. Deposition was studied for silicon oxide samples up to 2 inch in diameter. Best results were obtained for spin coating deposition at 500 rpm for 60 s. These parameters, however, did not assure a fully homogeneous on the whole surface deposition. This is due to the fact that no special treatment was

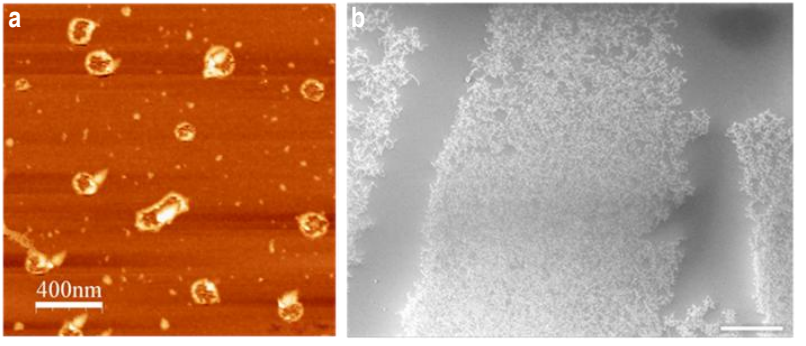

Figure 4.2: (a) AFM image of the catalyst material aggregates formed during the drying of the catalyst solution. (b) SEM image showing that CNT synthesis was not homogeneous when the catalyst deposition

applied to the surface of the samples to assure a good wetting when depositing the catalyst material. Figure 4.2 shows two examples of an irregular catalyst deposition: Figure 4.2-a is an image on the formation of particle aggregates during the drying of the sample on a chip and Figure 4.2-b shows a non homogeneous growth of CNTs on a sample after the catalyst material had been deposited at 3,000 rpm.

4.1.2 The CNT synthesis process

The CVD recipes for the synthesis of CNTs are normally composed of two main steps: the catalyst activation and the CNT growth. Apart from these two main steps, recipes include two more steps for the chamber conditioning and the chamber cooling (Figure 4.3).

1. The **chamber conditioning** is the step where chamber conditions are generated to arrive to the catalyst activation step. This step consists of several pump-purge cycles and a temperature increase up to the temperature where activation of the catalyst starts (Ta). Only inert gases are used in this step.
2. The **catalyst activation** consists in modifying the catalyst morphology to form the catalyst particles the CNTs grow from. In this step, the temperature is increased to the synthesis temperature (Ts) and the gases to activate the catalyst particles are injected.
3. The **CNT synthesis** consists in generating the conditions for the CNTs to grow. During this step, carbon containing gases and other gases that regulate the CNT formation reaction are injected to achieve their synthesis.
4. The **chamber cooling** step is the step where the process gases are cut, only inert gases are injected, and the chamber is cooled down to ambient temperature. The process ends with a pump-purge sequence to remove any process gas remaining in the chamber.

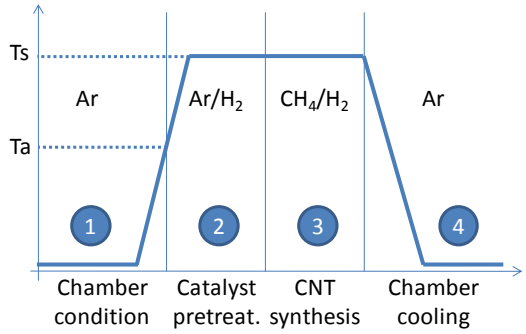

Figure 4.3: Schematic of a CNT synthesis recipe. The process is composes of four steps. The schematic shows the gases that are usually used in each step. Ta and Ts are the activation temperature and the synthesis temperature, respectively.

Methane (CH_4) was used as the carbon containing gas and hydrogen (H_2) for the catalyst material activation and for the CNT synthesis regulation. Argon (Ar) and nitrogen (N_2) were used as supporting gases and as the main gases during the chamber conditioning and chamber cooling steps, respectively. Synthesis temperature was set around 800ºC according to the pyrolysis of methane [45] and activation temperature to 500ºC. Because of the CVD system being *rapid thermal*, processes did not last more than 10 minutes at the synthesis temperature.

4.1.3 Influence of the CNT synthesis parameters

The influence of three CVD process parameters on the synthesis of the CNTs was evaluated: the synthesis temperature, the methane:hydrogen ratio and the hydrogen activation of the catalyst.

A) Influence of the synthesis temperature

The influence of the temperature was analysed for processes ranging between 700 and 900ºC. Figure 4.4 shows the influence of the synthesis temperature on the obtained CNT density. Included AFM images are representative images of the growth characteristic. AFM characterization of the synthesized nanotubes determined they were SWCNTs. Shown average diameters were calculated by measuring tens of SWCNTs. Measured values for the diameters of the SWCNTs on a sample were typically ± 0.5 nm the average diameter. No evident tendency is observe on the CNT diameter evolution.

Regarding CNT density below 750ºC no CNT growth was observed as methane decomposes at a temperature around 750ºC at the process pressure [45]. 800ºC was the temperature at which the highest synthesis density was achieved (Figure 4.4). This temperature was set as the reference temperature when designing new synthesis recipes.

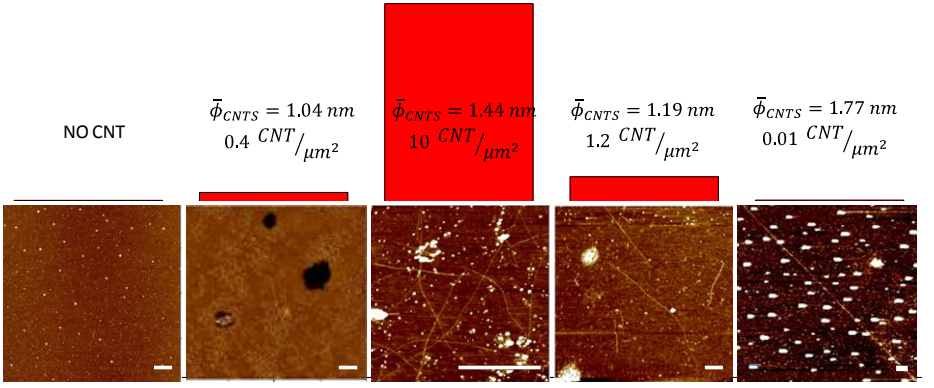

Figure 4.4: Influence of the synthesis temperature on the density of the SWCNTs. The AFM images are representative images of the CNT synthesis at each temperature. Scale bars are 1 µm. Z: 5 nm.

At 900ºC synthesis of "ultra-long" SWCNT was achieved. CNT lengths of up to 1.6 mm were characterised. This length involves a growth rate of 6.25 µm/s. This synthesis characteristic is similar to that reported in [46, 47] and it is attributed to an enhancement of the kinetics of the carbon diffusion through the catalyst particle. Enhanced kinetics explains how SWCNTs grow straight. The abrupt curvature of the SWCNTs may be due to defects on the surface or to the interaction of the SWCNTs with other catalyst particles or even with another SWCNT [39]. Apart from the "ultra-long" growth, enhanced diffusion may also be the reason for the decrease in the SWCNT density, as it is easier for the particles to become saturated with carbon.

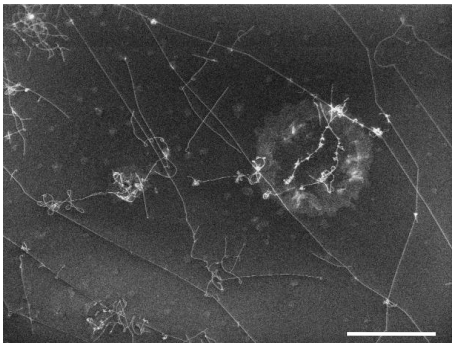

Figure 4.5: SEM image of ultra long SWCNTs. Scale bar is 100 µm.

B) Influence of the hydrogen:methane ratio

Hydrogen plays two roles during the CNT growth step: it regulates the CNT growth reaction and it serves to purify the already synthesized material.

In the first case, hydrogen reacts with the carbon atoms from the hydrocarbon after its pyrolysis and so, it regulates the growth speed and inhibits the catalyst particle saturation. Authors from ref. [48, 49] suggested that there exists a hydrogen ratio threshold that must be overcome for the CNTs to grow. Moreover, they also suggest that there exists a maximum concentration above which growth density decreases because of not enough carbon atoms reaching to the particle for the CNTs to form.

In the second case, hydrogen reacts with the amorphous carbon that is deposited on the substrate or surrounding the CNTs. As an example, Vivechand [50] used a hydrogen reflux at 1000ºC to purify MWCNTs. In other works it has also been pointed out that a high hydrogen flux during the CNT synthesis step leads to CNTs that are thicker in diameters because the thinner in diameter CNTs are removed by the hydrogen [31].

Figure 4.6 shows the influence of the hydrogen:methane ratio on the synthesized CNT density and on the morphology of the CNTs when the ratio is between 0 and 60% when performing RTCVD processes. The processes were, in all cases, performed at 800ºC and hydrogen was used to reduce

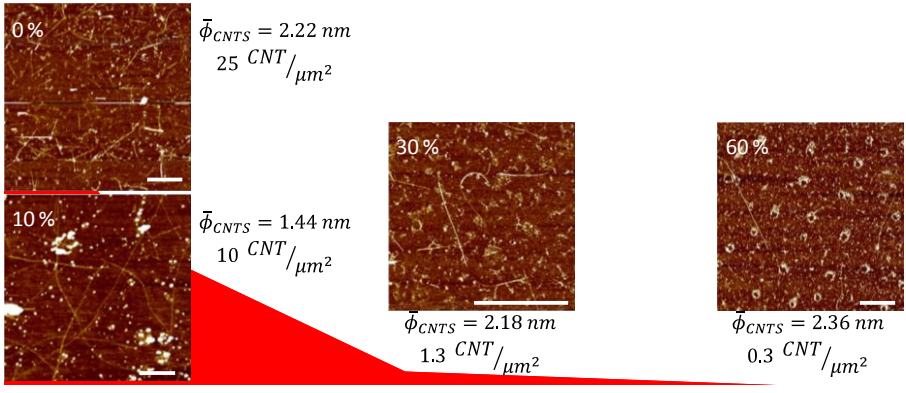

Figure 4.6: Influence of the hydrogen:methane ratio on the density of SWCNTs. Scale bars and Z scale of the AFM images are 1 µm and 5 nm, respectively.

the catalyst material prior to the growth step. The experiments demonstrated SWCNT synthesis in the whole examined range. Regarding synthesized CNT density, it decreases as the hydrogen ratio increased. In addition, the diameter of the CNTs that had been synthesised with higher hydrogen ratios tend to be bigger than those for low hydrogen ratios (the average diameter for the 0% process is neglected because the obtained in that case CNTs seemed to be detached from the surface of the sampe). These results corroborate those reported in [31].

When no hydrogen was included to the growth step, synthesis resulted in SWCNTs that were shorter than in the rest of the cases. This can be related to quicker particle saturation with carbon.

C) Influence of the hydrogen activation on the morphology of the catalyst particles

The morphology of the catalyst particles when the CNT growth starts, determines the structure of the CNTs to be formed. Different studies have addressed the analyses on the gases and temperatures of the activation step when using iron based particles [44, 51, 52]. In these cases, two different aspects were analysed: the influence of hydrogen on the catalyst material and its influence on the synthesis of the CNTs.

Regarding the diameter of the particles, hydrogen reduced particles were smaller than the not reduced ones, 2.25 nm vs. 2.7 nm. This result, however, should not be taken into consideration since particles were measured in ambient conditions after the activation process and so, they must have reacted again to form iron oxides.

Regarding the SWCNTs, their density after the process without hydrogen activation was higher than

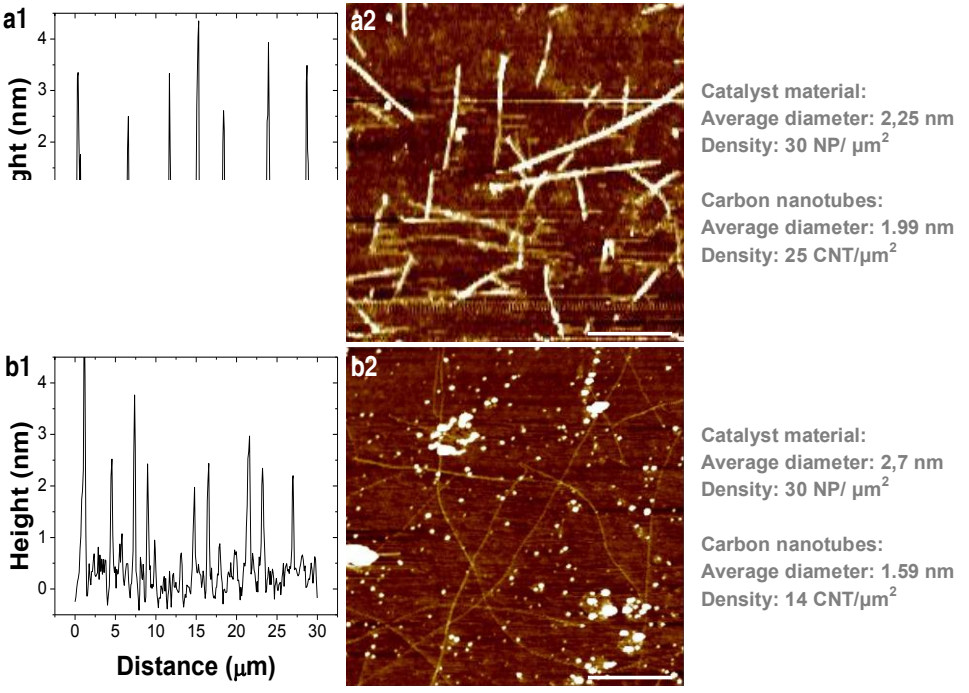

Figure 4.7: Catalyst activation influence on the catalyst material and on the synthesis of CNTs. (a1,b1) AFm obtained profile of the particle topography. (a2,b2) topographic AFM images of synthesized SWCNTs for the non-including hydrogen activation and for the hydrogen including activation processes, respectively. Scale bars are 500 nm. Z amplitude in a2 and b2 is 5 nm.

for the process with hydrogen activation. However, synthesized CNTs were shorter, larger in diameter and did not grow parallel to the surface according to SEM imaging.

4.1.4 Catalyst particle morphology and density influence

The morphology and the concentration of catalyst particles on the surface determine the structure of the CNTs [44, 52-54] and the morphology of the synthesized CNT layer [22].

A) Influence of the catalyst particle diameter

As described previously, the diameter of the CNT is directly related to the diameter of the catalyst particle it grows from. This way, if SWCNT synthesis has been demonstrated out of particles that are 3 to 6 nm in diameter (after they are reduced in hydrogen the iron nitrate modifies its structure to iron nanoparticles that are 2 nm in diameter or smaller), MWCNT synthesis is expected out of bigger particle aggregates.

The experiment consisted in comparing the previous results with the synthesis of CNTs when using iron based particles that were ~20 nm in diameter under the same synthesis conditions. This catalyst material consisted of the normally used iron particles that were left to form aggregates.

SEM images in Figure 4.8 show attained CNT synthesis when using the usually employed iron nitrate particles (Figure 4.8-a) and the catalyst aggregates (Figure 4.8-b). Images show that, in the first case, SWCNTs were synthesised whereas, in the second case, MWCNTs were obtained. Therefore, these images evidence that the diameter of the CNT depends on the diameter of the catalyst island it grows from.

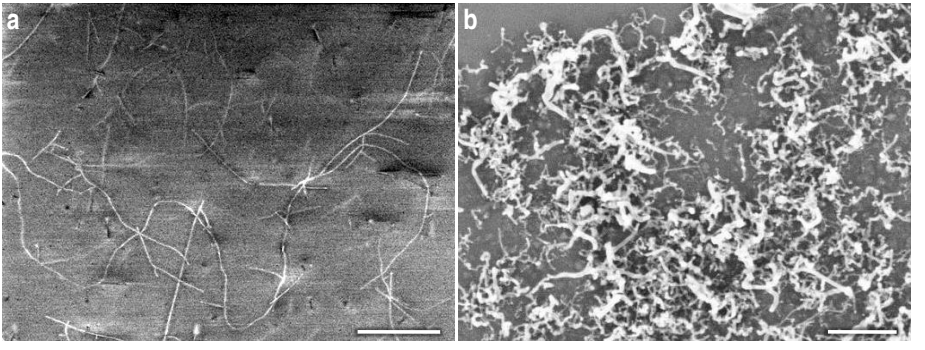

Figure 4.8: Influence of the catalyst particle diameter on the structure of the synthesized CNTs. (a) Synthesis of SWCNTs by few nanometre in diameter catalyst particles. (b) Synthesis of MWCNTs by tens of nanometre in diameter catalyst particles MWCNTs.

B) Influence of the catalyst particle density

CNT synthesis on samples where different catalyst particle concentrations had been deposited demonstrated that the synthesized CNT density is related to the catalyst particle density on the sample. However, it also demonstrated that there is a maximum for the iron catalyst particle density, above which, particles merge and form bigger in diameter CNTs (MWCNTs) but not higher in density SWCNT layers (Figure 4.9). The catalyst aggregate formation inhibition would have been possible if a strategy to increase surface roughness would have been taken. For example, it has been

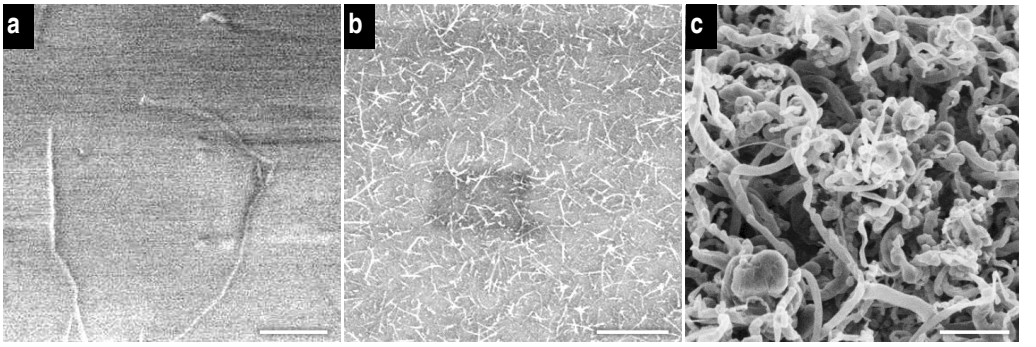

Figure 4.9: SEM images on the influence of the catalyst particle density on the structure and on the morphology of the CNT layer when. (a-c) CNT synthesis when catalyst was deposited from a 50, 200 or 400 ppm in concentration catalyst solution, respectively. Scale bars are 1μm.

demonstrated that deposition of an aluminium oxide thin layer increases the surface roughness and may lead to very high in density CNT synthesis [22, 30, 55].

4.1.5 CNT synthesis on different substrates

It was of great interest, from a technological point of view, to check the possibility to synthesize CNTs on different materials from silicon oxide that are also frequently used in micro- and nanofabrication. These experiments consisted in depositing ferric nitrate particles on those substrates and in trying different growth conditions.

A) CNT synthesis on silicon substrates

Silicon is the material that is most often used in micro- and nanotechnologies and so, it was found to be of interest to analyse CNT synthesis on this substrate.

In principle, lower CNT synthesis densities were expected because of a possible diffusion of iron into silicon and because of the reaction between iron and silicon to form iron disilicide ($FeSi_2$) [56], However, characterization of the samples revealed that SWCNT synthesis on silicon was comparable with that obtained on silicon oxide. Figure 4.10 shows also that circular shaped catalyst aggregates were formed during the catalyst deposition step. This was related to a non-optimised for silicon hydrophobicity catalyst deposition.

For more extensive discussion on the synthesis of CNTs out of silicide materials refer to Section 4.4.

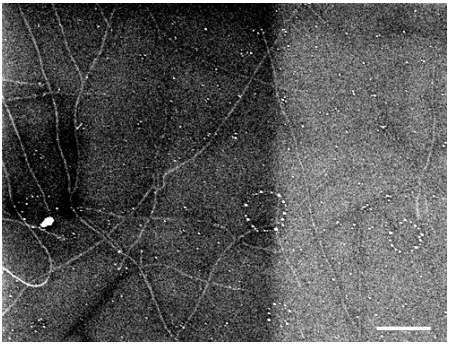

Figure 4.10: Synthesis of SWCNTs out of ferric nitrate particles on a silicon substrate. Scale bar is 1 μm.

B) CNT synthesis on silicon carbide substrates

Silicon carbide is an emerging semiconductor material that, compared to silicon, presents superior properties for power devices and that could also be used to fabricate CNT-based devices [57, 58]. Regarding CNT synthesis on silicon carbide, it has already been demonstrated that the silicon face on a silicon carbide sample can be sublimated to grow a vertically aligned CNT layer [59]. In this case, however, the approach consisted in checking CNT growth as it is normally done on silicon oxide substrates.

The SEM image in Figure 4.11 shows that SWCNT synthesis was attained similarly to silicon. SEM imaging of the samples revealed that CNT synthesis was concentrated at defects on the structure of the samples. This must have been due to a non-optimised catalyst material deposition. Regarding the CNT growth mechanism, in this case, it was tip growth, as the particles at the end of the CNTs are clearly observed. The fact that metal diffusion is lower in the case of silicon carbide than for silicon should improve CNT synthesis efficiency on this substrate. The different interactions between the SWCNTs and the substrate may also be the reason for their non-straight growth.

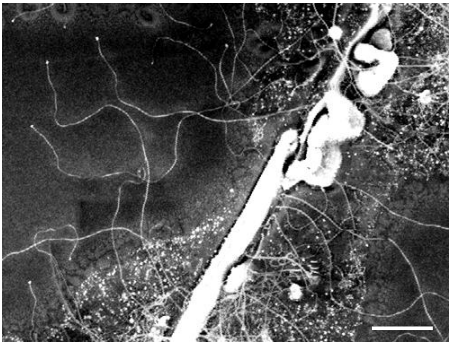

Figure 4.11: Synthesis of SWCNTs out of ferric nitrate particles on a silicon carbide substrate. Scale bar is 1 µm.

C) CNT synthesis on silicon nitride substrates

Silicon nitride is a material that is often used in microelectronics as passivation layer as it is hydrophobic. Figure 4.12 shows that CNT synthesis on silicon nitride was achieved. Synthesised in this case CNTs were MW (according to SEM images their diameters were between 50 and 60 nm) and their distribution was not homogeneous on the sample. The growth characteristic being different from that obtained on silicon oxide samples (where a homogeneous distribution of SWCNT had been synthesised) was attributed to the different wettability characteristics of the samples. This way, catalyst deposition on silicon nitride resulted in a non-uniform distribution of the catalyst material and in the formation of particle aggregates that led to the formation of MWCNTs instead of SWCNTs.

Optimization of the catalyst deposition parameters for silicon nitride by taking into account its hydrophobic characteristic should lead to the synthesis of CNTs in an analogous way as on silicon oxide.

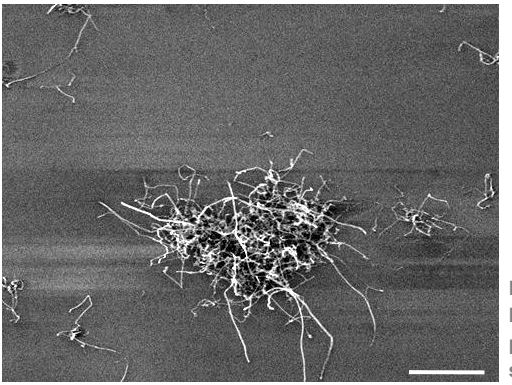

Figure 4.12: Synthesis of MWCNTs by ferric nitrate particles on a silicon nitride substrate. Scale bar is 2 µm.

D) CNT synthesis on platinum substrates

CNT synthesis on platinum was analysed because it is one of the most often used material for electrode and for bio-sensing device fabrication. Platinum is bio-compatible and it is stable up to very high temperatures. As no reaction between iron and platinum were expected, the approach consisted in depositing the catalyst material directly on the platinum surface.

AFM and SEM imaging of the fabricated samples (Figure 4.13) showed an increase of the roughness of the platinum surface and the formation of elongated shaped structures that seemed to be embedded in the substrate. Raman and EDX characterization of the samples gave evidence of carbon deposition but it was not possible to certify CNT formation.

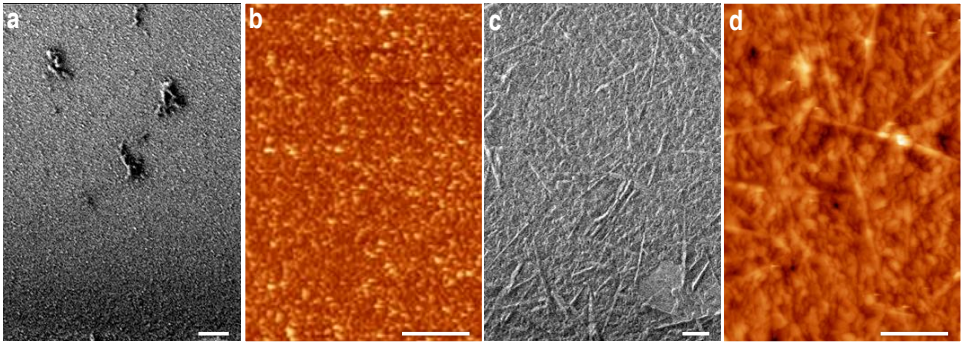

Figure 4.13: SEM (a,c) and AFM (b,d) characterization of the catalyst material on the platinum surface before (a,b) and after (c,d) the synthesis process. Scale bars are 1 µm. Z scale in the AFM images is 75 nm.

CNT synthesis on platinum substrates is the basis for the fabrication of the CNT-integrated multi-electrode devices which are presented in Chapter 10. For this reason and since a bio-compatible material would be more appropriate for the application, other approaches based on the use of platinum based catalyst materials were analysed (Chapter 5).

E) CNT synthesis on mica substrates

Mica was analysed as a substrate for CNT synthesis because of the flatness of its surface due to the highly perfect cleavage. The experiments showed that the mica sheets exfoliated when the process temperature reached 600ºC. Because of this, other type of CVD systems for low temperature

synthesis of CNTs, such as PECVD, or the use of carbon containing gases that decompose at temperature lower than 600ºC should be used on this substrate type.

CNT synthesis on quartz and sapphire were not studied because they are the materials that are already known for this purpose [38, 39].

4.1.6 Conclusions on the synthesis optimization by ferric nitrate

These sections have served to establish the bases for the synthesis of CNTs by the RTCVD technique when using iron nitrate as catalyst material.

Regarding ferric nitrate it must be highlighted that it was demonstrated to be an appropriate material for the synthesis of SWCNTs. However, it was also evidenced that, most probably because the ambient conditions affecting the catalyst solution preparation and the catalyst deposition, synthesis of the CNTs was not always reproducible.

The first experiments on the CVD process determined the appropriate conditions for the RTCVD synthesis of the CNTs. The optimal temperature was established to be 800ºC, hydrogen activation was determined to be necessary and the hydrogen:methane ratio during the CNT step was demonstrated to regulate the CNT density on the sample. This way, if low density of CNTs are to be synthesised, the hydrogen:methane ratio will be high whereas if a high density of CNTs is to be obtained, the hydrogen:methane ratio will be low. Apart from the CVD process parameters, the fact that the morphology of the catalyst particle affects the morphology of the CNTs has also been corroborated.

Besides the CVD conditions, the possibility of synthesising CNTs on other substrates different from silicon oxide, such as silicon, silicon carbide and silicon nitride has also been proved. Synthesis on platinum and mica are still under discussion.

4.2 Carbon nanotube synthesis by other iron based catalyst solutions

Once the influence of the CNT synthesis parameters had been understood, other iron based particles and compounds were studied as possible CNT catalysts. In this manner, magnetite, ferrocene, ferritin and a ferric nitrate-molybdenum-alumina composite particle were studied. Additionally, CNT synthesis from iron-cobalt catalyst particles embedded zeolite crystals was also evaluated. However, because of the objective of those studies were different from those of this section, they have been included in another section of this chapter (Section 4.2.5). This section focuses, then, on achieving the growth of CNTs out of the above mentioned catalyst materials and on discussing their suitability for the fabrication of devices.

The different catalyst materials that are used in this section where not prepared by the author in all cases: the magnetite particles were synthesised by Dr. Gemma Gabriel from IMB; the ferrocene and ferritin particles were synthesised by researches from the group of Prof. Avelino Corma and Prof. Hermenegildo García from ITQ; and the iron-molybdenum-alumina composite was prepared according to the guideline of Dr. Mª José Esplandiú from CIN2.

4.2.1 CNT synthesis by magnetite

According to reference [60], 4 nm in diameter magnetite (Fe_3O_4) particles may be reduced in hydrogen environments up to 1.7 nm in diameter iron particles that are appropriate for SWCNT synthesis. In order to study the use of this material for CNT synthesis by the RTCVD technique, 4 nm in diameter magnetite particles were prepared as described in [61] (Figure 4.14).

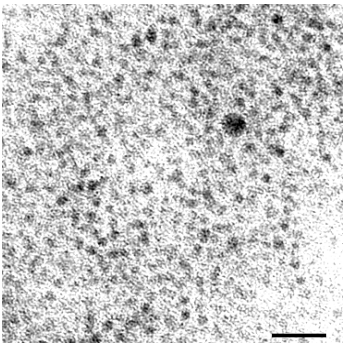

Figure 4.14: TEM image of the synthesized at IMB-CNM magnetite particles. Scale bar is 20 nm.

Several experiments were performed to analyse the differences between CNT synthesis from magnetite and CNT synthesis from iron nitrate but no significant conclusion was attained. Figure 4.16-a,b show the synthesis of low and high density of SWCNTs out of magnetite particles by switching the CVD process conditions, respectively.

SWCNT formation was confirmed by AFM and Raman spectroscopy. The diameters of the SWCNTs in Figure 4.16-a are 0.99 nm, 1.16 nm and 1.34 nm. Raman spectra of the sample in Figure 4.16-b

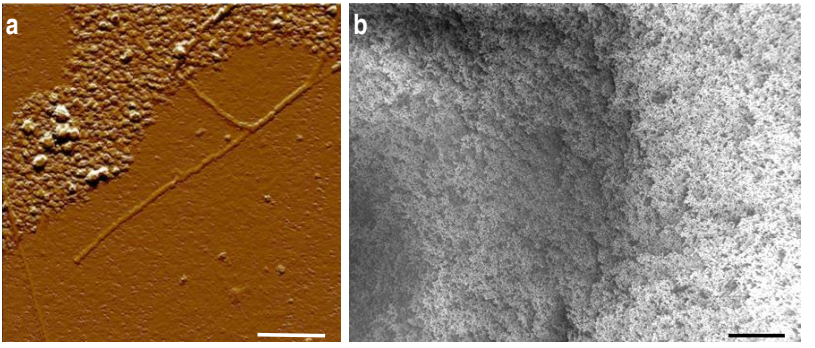

Figure 4.16: Images on the synthesis of SWCNTs by magnetite. (a) Phase AFM image on the synthesis of low density of SWCNTs. (b) SEM image on the synthesis of high density of SWCNTs. Scale bars are 200 nm and 100 µm, respectively.

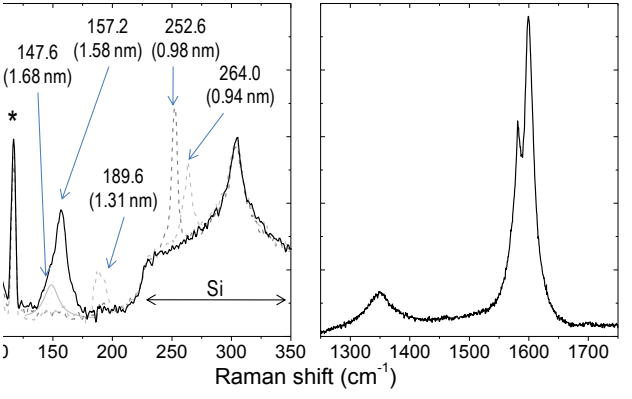

Figure 4.15: Raman spectra of the sample where high density of SWCNTs had been synthesized out of magnetite catalyst particles (Figure 4.16 (b)). Laser: 514.5 nm; X100; 0.85 mW.

show evidence of SWCNT formation as multiple resonances at RBM (100 - 300 cm^{-1}), double G peaks (~1,585 cm^{-1}) were observed and as the D peak (~1,350 cm^{-1}) was much less intense than the G peak [62]. The resonance at 313 cm^{-1} was related to the silicon from the substrate whereas the resonances in the RBM were related to SWCNTs with diameters between 0.94 and 1.68 nm. The resonance at 115 cm^{-1} corresponds to a plasma line.

4.2.2 CNT synthesis by ferrocene

Ferrocene ($C_{10}H_{10}Fe$) is an organometallic compound that consists of two cyclopentadienyl rings which are bounded on opposite sides of a central iron atom (Figure 4.17-a). Ferrocene is stable in air and sublimates in vacuum or at temperatures higher than 100ºC. It is soluble in organic solvents but not soluble in water. Ferrocene has been also demonstrated as an appropriate catalyst material for the synthesis of CNTs [28, 49].

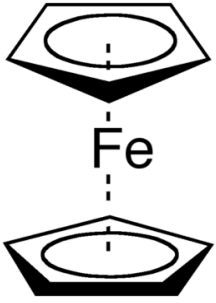

Figure 4.17: Schematic of the ferrocene molecule.

Different in concentration ferrocene containing solutions were prepared and deposited on previously PMMA patterned chips. Because of ferrocene being soluble in acetone and the acetone being used in the catalyst lift-off process, in order to inhibit iron removal from the patterned areas, a 30 nm thick gold layer was deposited on the catalyst to trap the particles. The AFM images on Figure 4.18 depict a 2 x 2 μm^2 and a 5 x 5 μm^2 patterned areas where ferrocene particles had been deposited. These images were obtained before and after metal deposition and lift-off, respectively. Figure 4.18-b shows that the ferrocene particles were completely covered by the metal layer.

Regarding the catalyst material morphology, AFM images revealed that the ferrocene aggregates were tents of nanometres. This way, the synthesis of MWCNTs was expected. If particles had been in the order of few nanometres, SWCNT could have been synthesised.

The SEM images in Figure 4.19 show the synthesis of MWCNTs on one of the test samples where

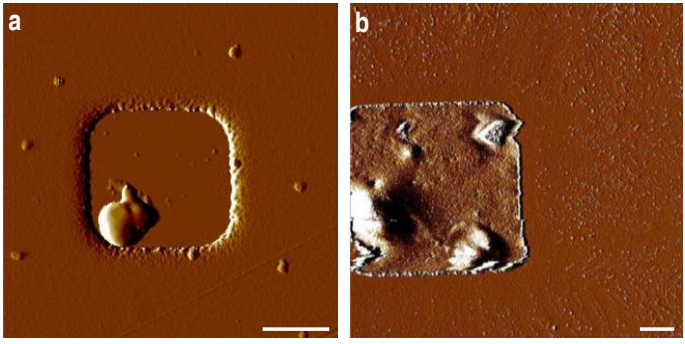

Figure 4.18: AFM images of PMMA patterned areas where ferrocene particles had been deposited. (a) AFM phase image of the patterning after the selective deposition of the catalyst material. (b) AFM phase image of the patterning after metal deposition and lift-off. Scale bars are 1 µm.

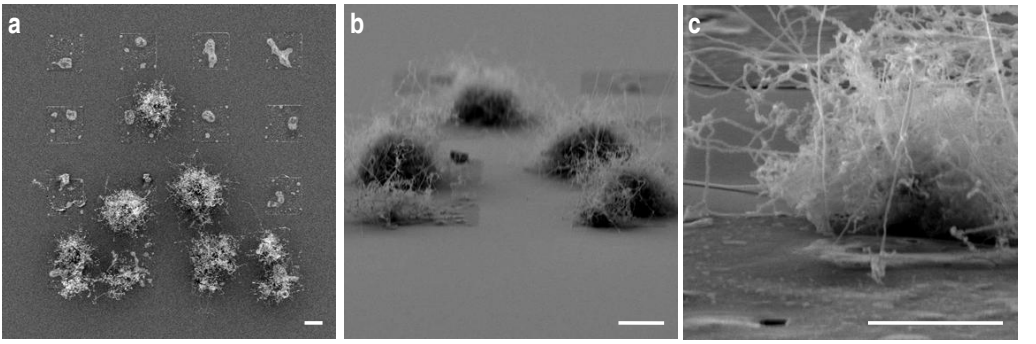

Figure 4.19: SEM images on the growth of CNTs out of ferrocene particles. (a) Top view of 10 x 10 μm^2 patterned areas. (b) Tilted view of the patterning in (a). (c) Tiled image of a detail of the MWCNTs that had grown out one of a ferrocene aggregate. Scale bars are 5 μm.

the CVD process parameters had been similar to those used for the synthesis of high density of CNTs when using ferric nitrate (800ºC; activation step including H_2; growth including CH_4 and H_2). Figure 4.19-a shows growth of high density of MWCNTs on part of the patterning. The fact that CNT synthesis was not observed on every patterned area was related to ferrocene particles not being deposited on every area and to a too thick metal coverage of some of the particles that may have acted as a barrier. Figure 4.19-b and Figure 4.19-c, which are tilted views of the CNTs in Figure 4.19-a, show that the synthesized CNTs were not arranged in spaghetti nor in forest configuration, but that their arrangement was chaotic.

Raman spectroscopy analyses of these CNTs (Figure 4.20) determined that are MW as a broad G (1,585 cm^{-1}) and disorder D (1,350 cm^{-1}) resonances were observed. The ratio between the disorder and G peaks, and the high in intensity D' (1,620 cm^{-1}) peak evidenced that the synthesized MWCNTs were defective [63].

Figure 4.20: Raman spectrum and peak decomposition of the synthesized out of ferrocene MWCNTs. Laser: 514.5 nm; X100; 0.92 mW.

4.2.3 CNT synthesis by ferritin

Ferritin was analysed as a possible catalyst material for growth of CNTs because of the non-compatibility of ferrocene with the lift-off processes. The capability of ferritin to nucleate growth of CNTs is similar that of the previously discussed iron based materials [64-67]. Figure 4.21 shows the structure of the horse spleen ferritin complex and a TEM image of the used particles. Ferritin is

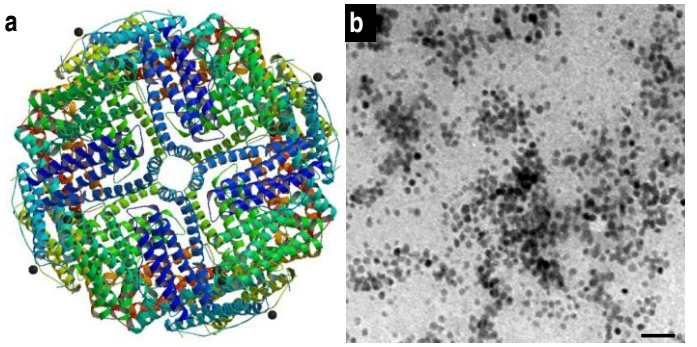

Figure 4.21: (a) Structure of the ferritin complex. (b) TEM image of the used for CNT growth particles. Scale bar is 50 nm.

composed of an iron core that is surrounded by a proteic shell that sublimes at temperatures higher that 60ºC. Ferritin is not soluble in acetone or in ethanol.

Ferritin from horse spleen [Ref.: 96701; Fluka] based solutions were prepared and deposited on previously pre-patterned samples. Because of excessive catalyst material, deposited at the patterning ferritin particles came out of the patterned areas during the lift-off process and re-deposited elsewhere.

Figure 4.22 shows attained results on the CNT synthesis optimization by RTCVD when using ferritin. Lighter in colour areas and structures are the synthesized MWCNTs. Figure 4.22-a shows part of the 10 x 10 μm^2 patterned areas. Out of the patterns light spots correspond to MWCNTs that grew from ferritin particles that had been removed from the patterns during the catalyst lift-off. Figure 4.22-b is the detail of one of the patterned areas in Figure 4.22-a. The catalyst material was deposited on the whole area of the patterns but higher particle densities were usually found on their borders. Figure 4.22-c is the magnified image of part of the MWCNTs in the pattern in Figure 4.22-b. The curly structure of the CNTs evidences that they were very defective.

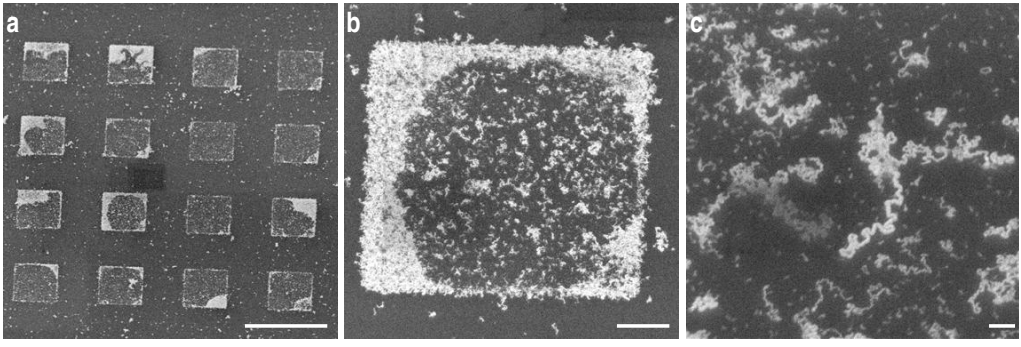

Figure 4.22: SEM characterization of the synthesized out of ferritin MWCNTs. (a) View of part of the 10 x 10 μm^2 patterning. (b) Detail of one of the patterned areas. (c) Detail of the synthesized MWCNTs. Scale bars are 20 µm, 2 µm and 200 nm in a, b and c, respectively.

4.2.4 CNT synthesis by iron-molybdenum-alumina particles

Ferric nitrate and molybdenum embedded alumina particles, henceforth Fe/Mo/Al_2O_3, is a catalyst complex that is often used in literature for SWCNT synthesis [21]. The catalyst particles are based on the same iron nitrate catalyst material as previously. Therefore, the catalyst original iron particles are

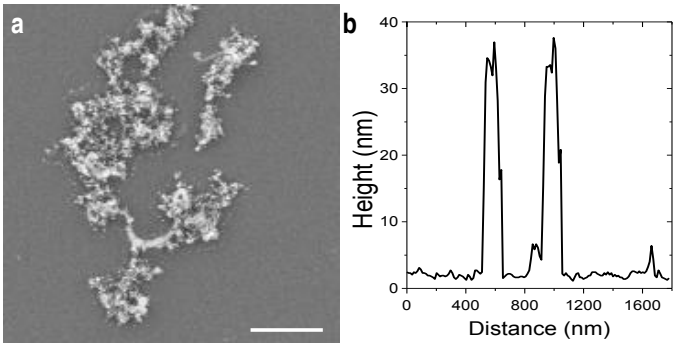

Figure 4.23: (a) SEM image of deposited on silicon oxide Fe/Mo/Al_2O_3 particles. (b) AFM measured topography of two particles. Scale bar in (a) is 1 µm.

between 3 and 6 nanometres and their iron core is around 2 nm. Molybdenum is incorporated to the catalyst complex because of its know capacity to improve the CNT synthesis efficiency [51]. Finally, the alumina particles, which are 35 to 50 nm in diameter, serve as a support for iron particles and molybdenum. Moreover, due to their roughness, they inhibit metal particle aggregation and favour SWCNT formation.

The first step of the catalyst solution preparation consists in mixing 60 mg of ferric nitrate (7782-61-8; Aldrich) with 3 mg of molybdenum acetate (17524-05-9; Aldrich) and 45 mg of alumina (1344-28-1; Degussa). Then, 45 ml of methanol are added to the particles. Finally, the solution is stirred for at least 8 hours. Each time the catalyst solution was to be deposited, the catalyst solution was ultrasonicated for, at least, one hour, to disaggregate any particle aggregates that could have formed during the solution storage. Figure 4.23-a is a SEM image of the catalyst composite after they had been deposited on a silicon oxide sample. Figure 4.23-b is the AFM profile of two complex particles. Their diameter is typically between 35 and 50 nm (that of the alumina particles).

The synthesis processes when using Fe/Mo/Al_2O_3 particles resulted in the growth of SWCNTs. As examples, Figure 4.24-a,b show suspended between particle aggregates SWCNTs and synthesized on silicon oxide SWCNTs, respectively.

The resonances at the RBM (100 – 350 cm^{-1}) in the Raman spectra of these CNTs (Figure 4.25) give evidence of the CNTs being SW. These resonances are related to SWCNTs with diameters between 0.77 nm and 1.73 nm. Besides the RBM, the G peak (1,585 cm^{-1}) is observed to be a double peak. The intensity of the disorder peak (1,350 cm^{-1}) being low with respect to G, and the G' (2,700cm^{-1})

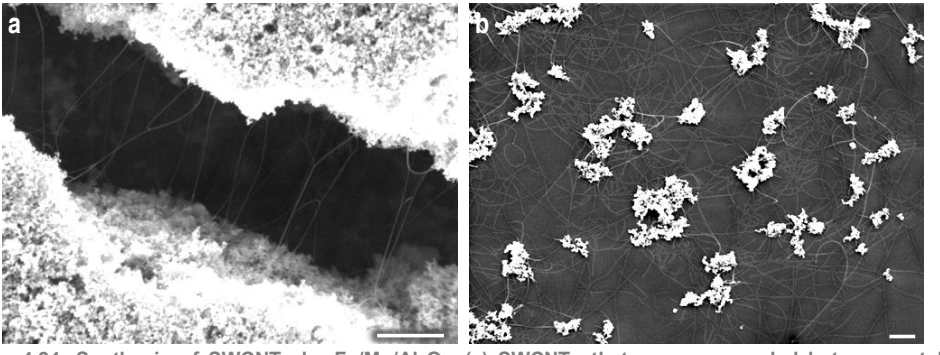

Figure 4.24: Synthesis of SWCNTs by Fe/Mo/Al_2O_3. (a) SWCNTs that grew suspended between catalyst particle aggregates. (b) SWCNTs that grew out of catalyst particles deposited on a silicon oxide substrate. Scale bars are 500 nm.

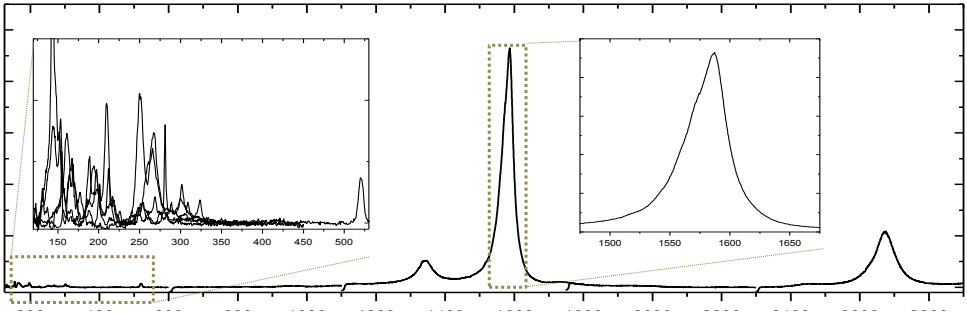

Figure 4.25: Raman spectra of the SWCNTs that had been synthesized out of Fe/Mo/Al_2O_3 particles. The insets show in detail the resonances in the RBM (100 – 350 cm^{-1}) and the G peak (1,585 cm^{-1}). Laser: 514.5 nm; X100; 1 mW.

peak being intense indicate a high degree of graphitization. Thus, a low density of defects is expected for the synthesised SWCNTs [68].

4.2.5 Conclusions on the synthesis optimization by other iron based catalyst materials

This section has explored the possibility and the convenience of using other iron based particles different from sole iron nitrate particles for the synthesis of CNTs.

The magnetite particles result in a CNT synthesis that is analogous to that achieved with the iron nitrate. Furthermore, CNT synthesis from magnetite was encountered to be more reproducible than the synthesis from ferric nitrate.

Efforts should be address to gain control over ferrocene and ferritin deposition in order to attain control over the synthesis of CNTs. Very dense growth of MWCNTs from ferrocene when the catalyst has been covered by a metal could of interest, for example, for the integration of CNTs into electrodes.

The Fe/Mo/Al_2O_3 catalyst has been demonstrated to result in a high yield of SWCNTs in the same way as the ferric nitrate. Moreover, this catalyst solution preparation is easy and, opposite to the only ferric nitrate based catalyst solution, the solution can be stored for several months without the CNT synthesis being affected and the synthesis still being very reproducible.

4.3 Directed and diameter constricted synthesis of single-walled carbon nanotubes by using zeolites as support material

Zeolites are micro-porous materials which pores are typically less than 1 nm in diameter and are periodically arranged in a certain direction [69, 70]. Thus, if the pores of zeolite crystals are used as a container for the CNT catalyst particles, they can determine the CNT diameter and can serve as guides for their growth [71-74]. Additionally, by placing the zeolites in a determined location and orientation on a substrate, control over SWCNT position and growth direction could be achieved (Figure 4.26). Therefore, success on the local deposition of zeolite crystals and on the synthesis of SWCNTs could lead to solve the two main challenges that hinder SWCNT integration into

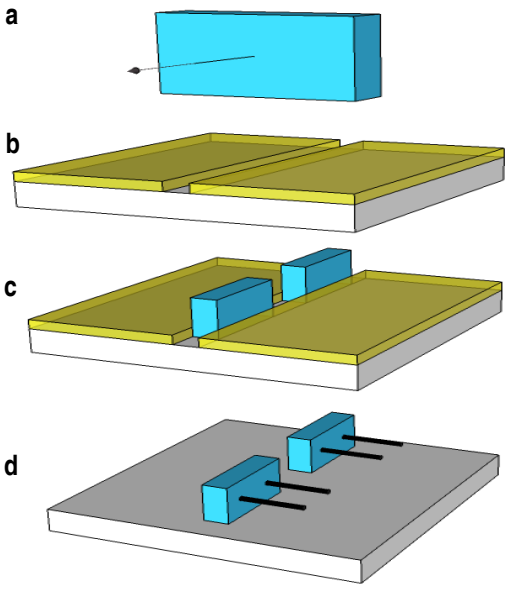

Figure 4.26: Strategy to synthesize localised on the substrate, oriented and diameter constricted SWCNTs. (a) Representation of a zeolite crystal and its pore direction. (b) Resist patterned substrate. (c) Oriented deposition of the zeolite crystals. (d) Resist lift-off and SWCNT synthesis.

nanoelectronic devices: achieving control over the chirality of the SWCNTs and over their position on the surface (Chapter 3),

This section summarises the experiments that were performed to analyse the viability of using zeolite crystals for the fabrication of devices based on SWCNTs. In particular, it is devoted to the optimization of CNT synthesis when placing the catalyst material inside two types of zeolite crystals:

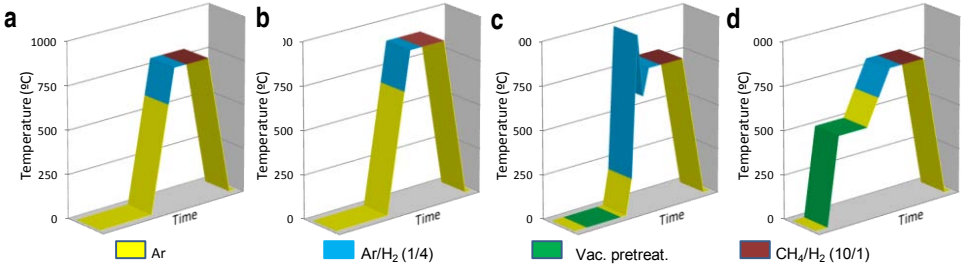

	P0	P1	P2	P3
Thermal pretreat.	No	No	No	No
Vacuum pretreat.	No	No	Yes	Yes
Catalyst activation	H_2	H_2	H_2 Dirac delta	H_2
CNT growth	CH_4/H_2 800ºC	CH_4/H_2 900ºC	CH_4/H_2 800ºC	CH_4/H_2 800ºC

Figure 4.27: Schematic of the four analysed CNT RTCVD synthesis processes. (a) Synthesis process at 800ºC including a pretreatment in hydrogen environment. (b) Synthesis process at 900ºC including a pretreatment in hydrogen environment. (c) Synthesis process at 800ºC including a vacuum pretreatment and a "Dirac delta" shaped pretreatment in hydrogen environment. (d) Synthesis process at 800ºC including a vacuum pretreatment at 500ºC and a pretreatment in hydrogen environment.

ALPO-5 and zeolites L. Despite the fact that they are different in structure, the main difference from a CNT synthesis point of view, laid on the manner the catalyst material was deposited inside the pores of the crystals. Zeolite crystals synthesis and catalyst material filling of the pores was performed at ITQ by the group of Prof. Avelino Corma and Prof. Hermenegildo García in the frame of CRENATUN project.

The CNT synthesis optimization considered previously presented results on CNT synthesis when using iron particles (section 4.1 and 4.2) and focuses on the influence of pretreatments and on the influence of the synthesis temperature. Four different processes was analysed (Figure 4.27).

The base process, P0, (Figure 4.27-a) consisted in a hydrogen activation of the catalyst and a synthesis step combining methane and hydrogen at 800ºC. The process modifications consisted in increasing the process temperature level to 900ºC, P1 (Figure 4.27-b), in introducing a vacuum pretreatment and modifying the activation pretreatment to resemble a "Dirac delta" function, P2 (Figure 4.27-c), and in introducing a high vacuum pretreatment at 500ºC, P3 (Figure 4.27-d).

4.3.1 CNT synthesis optimization by AlPO-5 zeolite crystals

AlPO-5 is a zeolite structure that has ordered channels which are 0.73 nm in diameter [75]. Figure 4.28-a is a schematic of the structure of the zeolite.

Although ALPO-5 crystals are normally obtained by precipitation of alumina and phosphate, in this case a minor amount of iron nitrate and cobalt nitrate (iron:cobalt atomic ratio 3:1) was purposely added together with aluminium nitrate to the phosphoric acid solution. In this way, when the solid was formed, certain crystallographic positions, typically occupied by aluminium, were isomorphically replaced by iron and cobalt to form the catalyst material inside the pores without affecting their crystalline structure.

The SEM image in Figure 4.28-b is representative of the ALPO-5 crystals morphology. The Raman spectra of the ALPO-5 crystals (Figure 4.28-c) showed no resonance at frequencies in the RBM of the CNTs. The resonance peak at 520 cm^{-1} corresponds to silicon.

A) CNT synthesis by ALPO-5 crystals

Even if optical observation of the samples after the synthesis processes showed, in general, a darkening of the crystals, only two CNT synthesis characteristics could be elucidated.

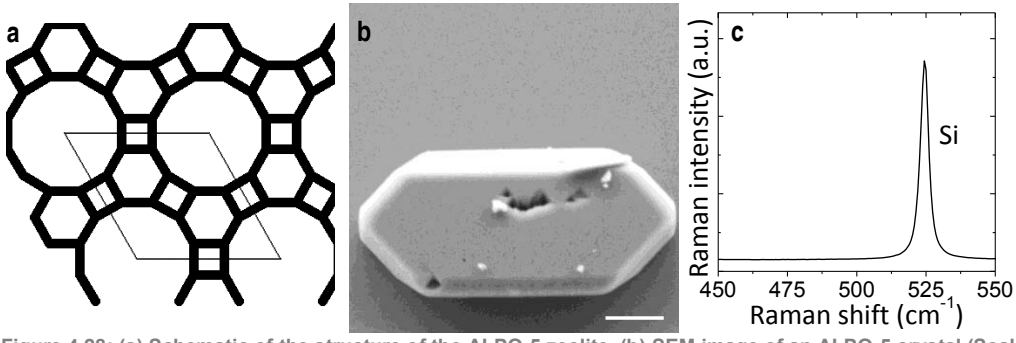

Figure 4.28: (a) Schematic of the structure of the ALPO-5 zeolite. (b) SEM image of an ALPO-5 crystal (Scale bar is 1 µm). (c) Raman spectra of ALPO-5 zeolites on a silicon substrate (laser: 514.5 nm; X100;0.75 mW).

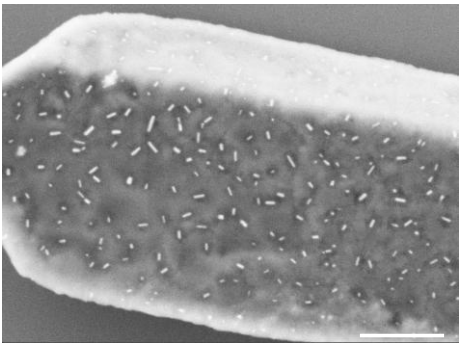

Figure 4.29: SEM image of an ALPO-5 crystal after a synthesis process at 800ºC including a pretreatment in hydrogen environment. The image shows high density of nano whisker-like structures on the surface of the crystal. Scale bar is 200 nm.

(i) CNT synthesis process when applying the base process

Representative results of the synthesis P0 process are shown in Figure 4.29. The SEM image of an ALPO-5 crystal shows the formation of high density of whiskers that come out of the crystal in every direction. Raman spectroscopy, on the contrary, gave no evidence of CNT synthesis as no peak related to CNT formation was found. However, even if no resonance was observed, because of the narrowness and their elongated aspect, synthesized structures can be assumed to be CNTs growing from the pores of the ALPO-5 crystal. The lack of CNT related resonances on the Raman spectra could be related to the low Raman signal intensity due to low density of crystals on the sample, to the faces of the crystals where the material had been synthesised not facing the laser or to a bad combination of the Raman parameters even if different conditions and samples were tested.

Apart from the discussion on the nature of the carbon structures, another discussion arises from the fact that the synthesized structures grew not only according to the direction of the pores of the crystal but also in other directions. In this sense, it was estimated that the non dehydration of the crystals before the synthesis process, in combination with the high thermal level during the process, may have generated defects on the zeolites structure that could result in the appearance of new pores in all the directions of the crystals.

(ii) CNT synthesis process including vacuum pretreatment

Figure 4.30 shows attained results when the P1 process was applied. Unlike in the previous case, this time SEM images (Figure 4.30-a) did not reveal the formation of any CNT structure (maybe because

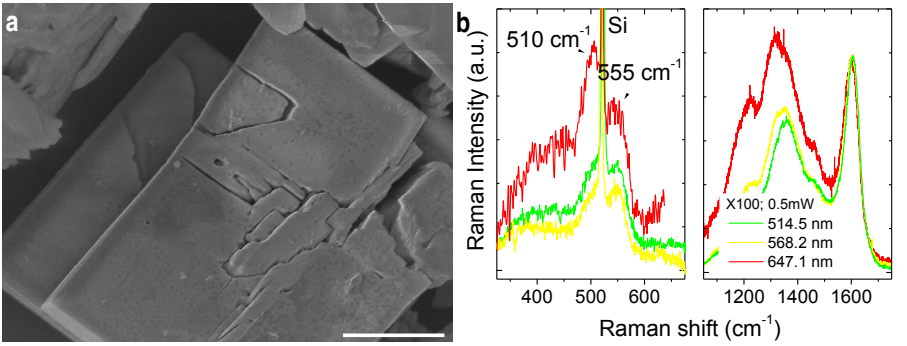

Figure 4.30: (a) SEM image of the ALPO-5 crystals showed no evidence of CNT synthesis after the P1 synthesis process. Scale bar is 1 µm. (b) Raman spectrum of the ALPO-5 crystals for three different laser lines showing resonances in the RBM. Laser: 514.5, 568.2 and 647.1 nm; X100; 0.5 mW.

of SWCNTs being too short to arrive to the surface of the zeolite or maybe because of non-optimised SEM conditions (check Section 2.2.1 for a discussion on the SEM characterization of the CNTs), whereas Raman spectroscopy (Figure 4.30-b) revealed the formation of very small in diameter SWCNTs. The resonance peaks at 510 and at 553 cm^{-1} were related to the 4.20 Å in diameter (4,2) SWCNT and to the 3.95 Å in diameter (5,0) SWCNT [76]. Obtained spectra were reproduced at ITQ. Additionally, these results are in good agreement with those reported in [74, 77, 78] where analogous Raman spectra are observed when synthesizing SWCNTs out of AlPO-5 crystals. The use of AFM to observe the SWCNTs on the zeolites was considered but was found to be not viable because of the orientation of the zeolites and because of their roughness.

4.3.2 CNT synthesis optimization by zeolite L crystals

Zeolites L are microporous aluminosilicate materials which pores are 0.75 nm in diameter [79]. An schematic of the structure of L-type zeolites is shown in Figure 4.31-a.

Three sets of zeolite L crystals were used to study CNT synthesis. Since the crystals from Set-1 were aimed for the first experiments, their size was smaller than 500 nm and they were not shape uniform. The zeolite crystals forming Set-2 and Set-3 (Figure 4.31-b) were synthesized in a more controlled ambient for the reactions to take place at low speed and, thus, these crystals were prismatic and several microns in length. The pores of these crystals were arranged parallel to the major axis of the crystal.

Iron and cobalt nitrates were used as catalyst material. Two different catalyst deposition procedures were employed. The catalyst was deposited by impregnation of the crystals from Set-1 and Set-2 until the weight of the iron:cobalt particles reached 2.5% of the total mass. Crystals were thoroughly rinsed in deionised water to remove any catalyst material on their surface. Catalyst material deposition on Set-3 was performed by ion-exchange to improve particle penetration into the pores of the zeolite L crystals. Rinsing of the crystals was, in this case, more aggressive than in the previous ones. This procedure was also repeated several times until the weight of the iron:cobalt particles reached 2.5% of the total mass.

The Raman spectra of the zeolite L crystals before CNT synthesis (Figure 4.28-c) showed two intense resonance peaks. The resonance at 520 cm^{-1} corresponds to the silicon from the substrate, whereas the resonance at 507 cm^{-1} was attributed to the zeolites L crystals.

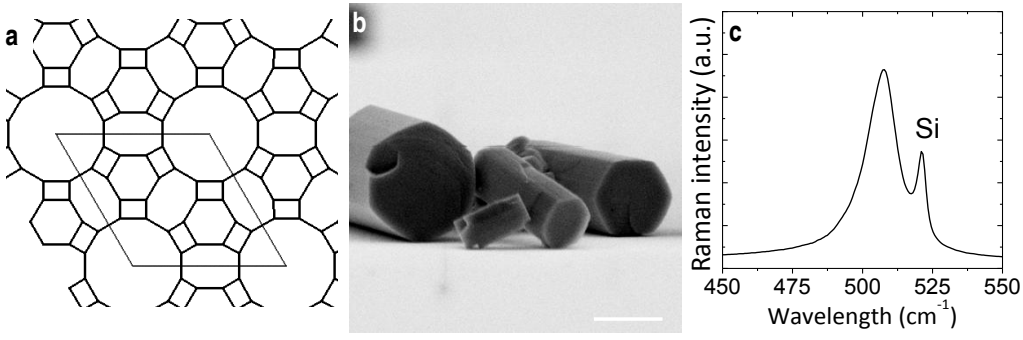

Figure 4.31: (a) Schematic of the structure of a L-type zeolite. (b) SEM image of deposited on silicon zeolite-L crystals from Set-2 (scale bar is 1 µm). (c) Raman spectrum of zeolite-L crystals on silicon. Laser: 514.5 nm; X100; 0.75 mW.

A) CNT synthesis by zeolite L crystals

As in the case of the synthesis of CNTs from ALPO-5 crystals, the darkening of the zeolite L crystals was typically observed after the synthesis process. When examining the samples by SEM and Raman spectroscopy four different structure syntheses were found. In some cases, the synthesis of SWCNTs or MWCNTs wase easily identified but, in the others, a definite conclusion was not attained.

(i) CNT synthesis process when applying the base process

SWCNTs grew from zeolites surface when the process including hydrogen activation and synthesis at 800ºC (P0) was applied. The SEM images in Figure 4.32 correspond to three different samples were zeolite L crystals from Set-1 to Set-3 had been deposited respectively. SEM images show, apart from the optimization of the morphology of the zeolite L crystals from Set-1 to Set-3, how catalyst deposition was optimised to achieve synthesis of higher density of SWCNTs from the catalyst material deposited inside the pores of the crystals but not on their crystal faces.

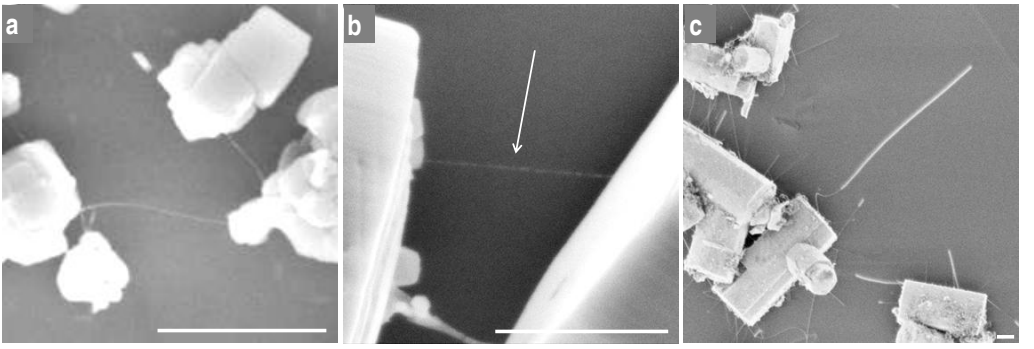

Figure 4.32: (a-c) SEM images of zeolite L crystals from Set-1, Set-2 and Set-3 after the P0 synthesis process. Scale bars are 500 nm.

SEM characterization of these and other analogous samples evidenced two main growth characteristics. First, SWCNTs tend to grow perpendicular to the surface of the crystal even if a few degree deviations are very often observed. Second, SWCNTs tend to grow in a particular direction but, after they get in contact with the substrate, they usually curve, most probably due to SWCNT-surface interactions.

Figure 4.33 are the Raman spectra at the RBM frequencies of a sample formed by zeolites from Set-1. The two resonance peaks at 175 cm^{-1} and at 272 cm^{-1} on the silicon resonance correspond to a

Figure 4.33: Raman spectra of the RBM frequencies of samples where Zeolite L crystals had been deposited after the P0 synthesis process. Laser: 514.5 nm; X100; 0.96 mW.

1.42 nm and to a 0.91 nm in diameter SWCNTs. The resonance at 120 cm^{-1} is a Plasma line. In general, Raman spectra of the CNTs on these samples certified synthesis of SWCNT. Measured diameters ranged between 0.45 to 1.5 nm. The biggest in diameter SWCNTs were observed on samples where crystals from Set-1 had been deposited. As these crystals were the less perfect in synthesis and catalyst deposition, it is possible that the biggest in diameters SWCNTs could correspond to SWCNTs that grew from catalyst particles located on the faces of the crystal, which were uncontrolled in morphology, rather than from particles inside the pores.

In order to determine the SWCNT growth starting point, a zeolite crystal was milled by means of E-beam (3 keV) around a SWCNT. Figure 4.34-a shows a zeolite crystal from which two SWCNTs had grown before the electron milling. Figure 4.34-b,c are SEM images of the E-beam milled area during and after the milling, respectively. SEM image in Figure 4.34-c looks deformed because of electron charging of the crystal. The image shows clearly that the CNT had grown from inside the crystal.

This result was positive to certify SWCNT growth from inside the crystal but evidenced that CNTs could find a path through the crystal structure to grow perpendicular to the pore direction instead of along it.

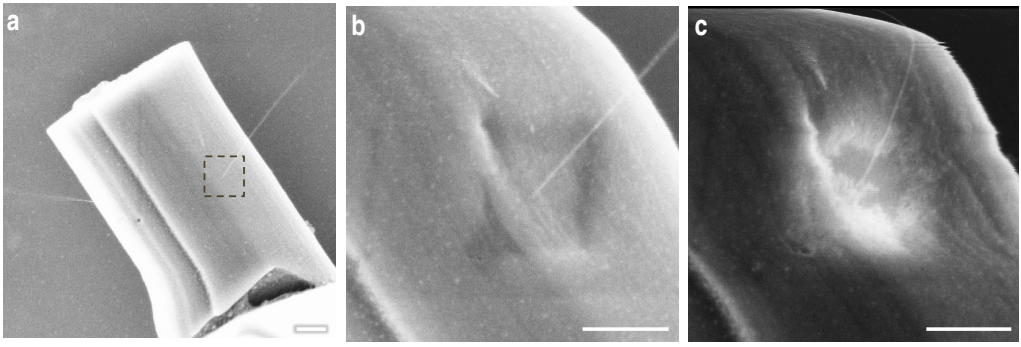

Figure 4.34: SEM images of the electron milling of a zeolite L crystal. (a) The zeolite crystal after the CNT synthesis process. The marked area is the area that was milled afterwards. (b) First stages of the electron milling. (c) Image of the milled area once the etching was over. Scale bars are 200 nm.

(ii) CNT synthesis process at 900ºC

It has been shown in Section 4.1.3 how the SWCNT growth kinetics were highly enhanced when the synthesis temperature is set to 900ºC, giving arise to SWCNTs that were “ultra-long”. In the case of zeolite L crystals, however, no such long SWCNT were found when applying process P1. On the other hand, it was observed that high density of filamentous carbon structures arose perpendicular to the crystal surface (Figure 4.35-a). These structures may correspond to SWCNTs. In this sense, although the Raman spectra of the samples were not totally conclusive (Figure 4.35-b), they suggest synthesized structures to be SWCNTs due to the resonances in the RBM, because the ratio between the D (~1,350 cm^{-1}) and the G (~1,585 cm^{-1}) peaks was low and because the G peak could be decomposed into a double peak. Their estimated diameter would be 5 Å according to the resonance peak at 498 cm^{-1} and the relationship between w_{RBM} and d_{CNT} [62].

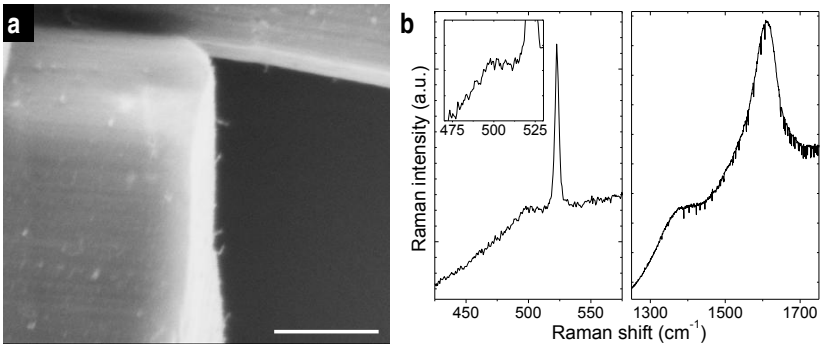

Figure 4.35: (a) SEM image and Raman spectra of zeolite crystals after the P1 synthesis process. The image shows filamentous structures perpendicular to the surface of the crystal. Scale bar is 200 nm. (b) Raman spectra of the synthesized material. Laser: 5145.5 nm; X100; 0.75 mW.

(iii) CNT synthesis process including "Dirac delta" activation

The process including the "Dirac delta" pretreatment, P2, was designed taking advantage of the rapid thermal capabilities of the RTCVD system (section 2.1.1). The pretreatment consisted in applying a very short power pulse to the heating lamps so that the temperature in the chamber increased from 500ºC up to 1000ºC in few seconds. After the pulse, the applied to the lamps power was set to attain the CNT growth step temperature (800ºC). During the pretreatment a H_2 was flown into the chamber.

The SEM Images in Figure 4.36 demonstrate the synthesis of a very high density (in comparison with the reported densities for P0 and P1 processes) of CNTs when applying the P2 process. Synthesized in this case CNTs were MW and their curved shape suggests they are defective in structure. These CNTs are bigger in diameter than the theoretical pore diameter of the zeolite, most probably because the high heating broke the crystal structure and catalyst particles merged to form bigger particles. In addition, damage on the zeolites may have generated new pores in the structure for the CNTs to come out of the crystal.

Besides the CNT structure, the fact that most of the MWCNT density is condensed on the edges of the crystals (Figure 4.36-b) gives evidence of a correct deposition of the catalyst material inside the pores of the crystals, and not on their surface.

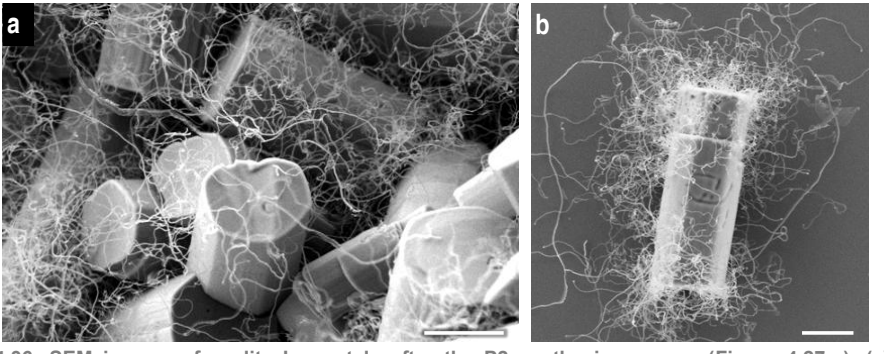

Figure 4.36: SEM images of zeolite L crystals after the P2 synthesis process (Figure 4.27-c). (a) High density of MWCNTs and Zeolite L crystals. (b) A single zeolite crystal showing higher CNT density at the edges of the crystal. Scale bars are 1 µm.

(iv) CNT synthesis process including vacuum pretreatment

When the 10 minute vacuum pretreatment at 500ºC is introduced in the synthesis process, P3, (Figure 4.27-d), carbon structures as the ones observed in Figure 4.37 are obtained. These structures, which grow perpendicular to the surface of the crystals and tend to grow according to the pore direction, have diameters and lengths in the order of hundreds of nanometres.

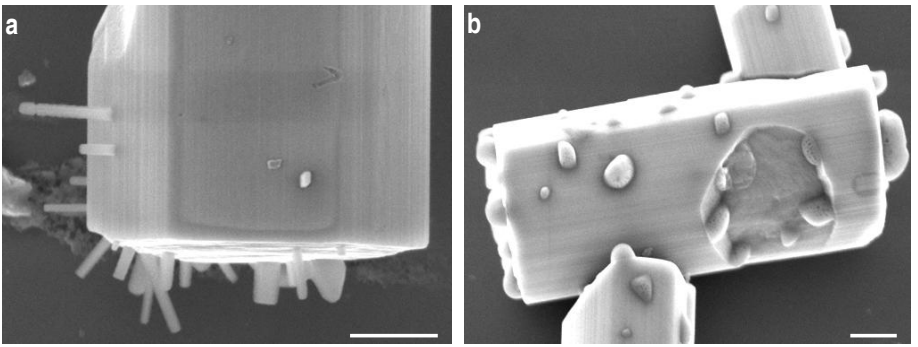

Figure 4.37: Zeolite L crystals after the P2 process. SEM images of the crystals show the formation of carbon structures. (a) The pillar shaped structures form perpendicular to the crystal surface. (b) Wider but shorter carbon structures on another zeolites crystal. Scale bars are 500 nm.

Figure 4.38 shows the Raman spectrum of a zeolite crystal after the synthesis process. Apart from the peaks related to silicon (313 cm^{-1} and 520 cm^{-1}) and the resonance peak related to zeolite L crystals (510 cm^{-1}) two other peaks were detected in the RBM at 475 cm^{-1} and 504 cm^{-1}. These resonances could correspond to the 0.52 nm and to 0.49 nm in diameter SWCNTs respectively. The fact that the peaks at high frequencies do not resemble the ones for a SWCNT can be due to amorphous carbon on the surface of the zeolite screening the resonances.

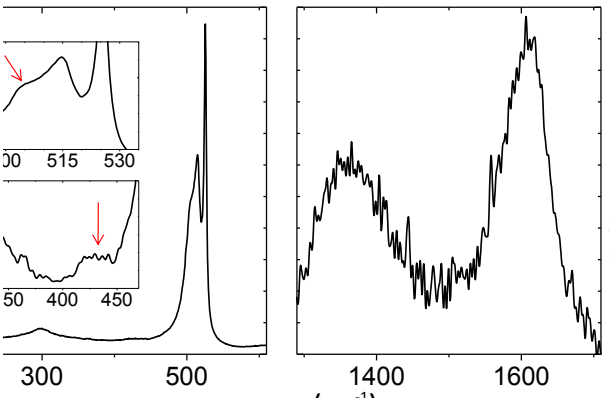

Figure 4.38: Raman spectrum at low and high frequencies of zeolites crystals after the P3 synthesis process. Insets, magnifications of the resonance peaks at 475 cm^{-1} and at 504 cm^{-1}. Laser: 514.5 nm; X100; 0.98 mW.

Disaggregation of the carbon structures

Figure 4.39 shows the disaggregation sequence of the synthesized carbon structures during their SEM imaging at 3 keV. The sequence shows how the fibre on the left is displaced during the first seconds. Then, it takes around 130 s to the fibre to completely disappear. The fibre on the lower side stands for more than 3 min. As time passes, the fibre looses stiffness until it collapses on the crystal

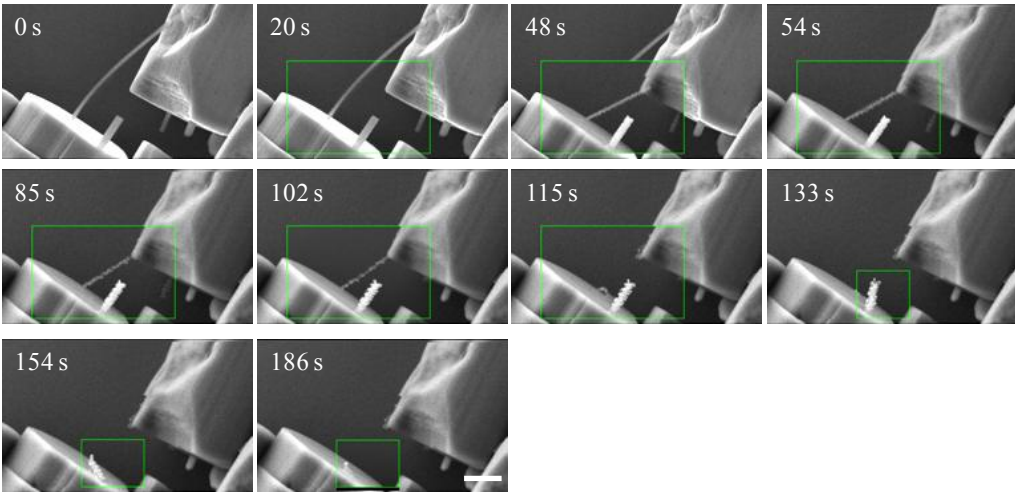

Figure 4.39: SEM images of the disaggregation sequence of the carbon structures that had been synthesized by a P3 RTCVD process. Scale bar is 500 nm.

surface. These observations suggest that the carbon structures could correspond to SWCNT bundles that debunddle because of the electron charging.

4.3.3 Conclusions on the synthesis of CNTs by zeolite crystals

These sections have explored the possibility of using two types of zeolite crystals (AlPO-5 and zeolite-L) to overcome the two main challenges on SWCNT integration into CNT-FET based devices: achieving the control over the growth direction and over the chirality of the SWCNTs. Synthesis of SWCNTs has been achieved when using both types of zeolites.

Regarding CNT synthesis from AlPO-5 crystals, evaluation of the synthesis was complicated because of the non uniform morphology of the zeolite crystals and because of the difficulties to find evidence of the growth results. Despite these hitches, synthesis of the smallest in diameter SWCNT has been achieved.

The prismatic and homogeneous morphology of the zeolite-L crystals eased evaluation of CNT synthesis. Growth of SWCNTs from inside the pores of the zeolites has been demonstrated when the catalyst is correctly deposited inside them. Hence, the diameters of these SWCNTs must be smaller than the pore of the zeolites. In these cases, it has been observed that the SWCNTs tend to align according to the orientation of the pores in the zeolite. However, when the SWCNTs get in contact with the substrate, they tend to curve.

4.4 Carbon nanotube synthesis by nickel silicide

The contact resistance between the CNTs and the metallic contacts when fabricating CNT based devices is an issue to which many studies have been addressed and that is still being improved [80, 81].

Nickel monosilicide (NiSi) is a compound material with a low sheet resistance that is being studied to improve interconnections in the frame of the most advanced CMOS technologies [82]. If nickel silicide could directly be used as the CNT catalyst material in device fabrication [83] a good contact between

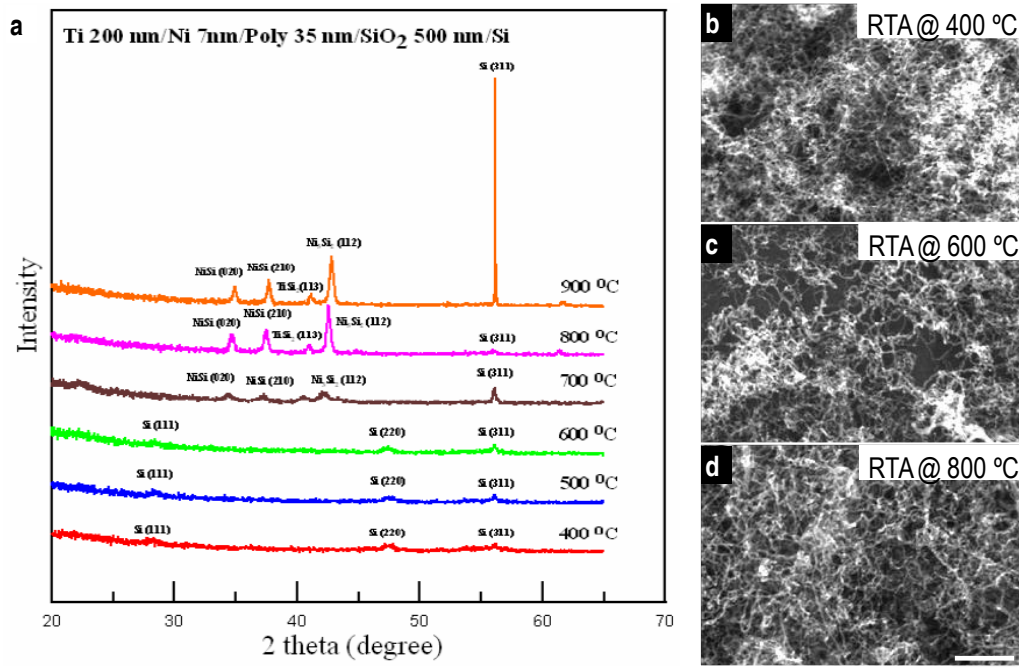

Figure 4.40: Previous studies on the formation of nickel silicide and on the synthesis of CNTs. (a) X-ray diffraction studies on the nickel silicide formation for a silicon / 500 nm silicon oxide / 35 nm poly-silicon / 7 nm nickel / 200 nm titanium multilayer configuration for different annealing temperatures. (b-d) synthesized MWCNTs after the nickel silicide formation at 400, 600 and 800ºC, respectively. Scale bars in (b-d) are 1 µm. Courtesy of Dr. J.H. Ting.

the CNT and the catalyst layer would be achieved and, thus, the performance of the devices would be optimised.

The study that is presented in this section was mainly carried out at the National Nanodevice Laboratories, NDL, in Taiwan, during an internship at Prof. Jyh-Hua Ting's group in the frame of a CNM - NDL collaborative exchange project. Prof. Ting's group had considerable expertise in the synthesis of CNTs out of silicide based compound materials. As example, Figure 4.40 shows some studies on the formation of nickel silicide for different thicknesses of the nickel and the poly-silicon layers and on the synthesis of MWCNTs out of the formed compound materials.

This section presents the advances on the synthesis of CNTs by thermal CVD and nickel silicide based catalyst materials. In particular, it focuses on the optimization of a thinner than previously used nickel silicide catalyst layer and on the optimization of the CNT synthesis conditions aiming to achieve the directed synthesis of SWCNTs across two metals. A monitor chip that the group had previously designed was used to accomplish the tasks.

4.4.1 Sample fabrication

The fabrication of the samples was divided into three main tasks: the test wafer and the test vehicle chip fabrication, the nickel silicide formation and the CNT synthesis.

A) Test vehicle chip fabrication

Figure 4.41 shows the schematics of the test vehicle and a table on the analysed multi-layers structure. The chip (Figure 4.41-a) was designed so that the CNTs grew only along the borders of the catalyst islands, which are shown more in detail in Figure 4.41-b and Figure 4.41-c. The lateral pads were designed as contacts to apply an electric field to direct CNT growth across the catalyst islands. Wires connecting the lateral pads and the device pads could be scratched after CNT synthesis to avoid short circuits during electrical characterization of the devices. Four square shaped areas had been included for an optical control of the nickel silicide formation and of the CNT synthesis.

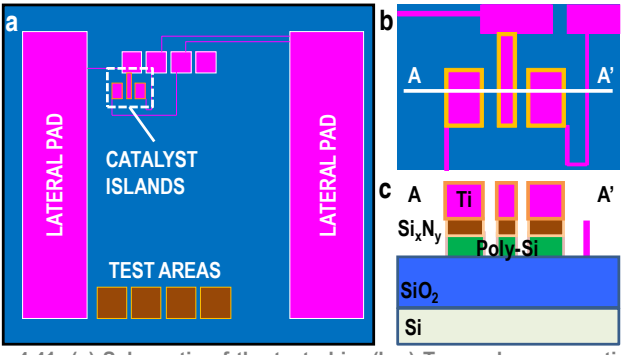

d

	Poly-Si (nm)	Ni (nm)	Ti (nm)
1	35	7	200
2	35	3	---
3	35	3	200
4	25	3	---
5	25	3	200
6	10	3	---
7	10	3	200
8	0	3	200

Figure 4.41: (a) Schematic of the test chip. (b-c) Top and cross section views of the catalytic islands. (d) Summary of the different poly-silicon / nickel / titanium configurations on the fabricated samples.

The first step of the technological process consisted in growing a 500 nm thick silicon oxide layer on the 6 inch silicon wafers. Then, different in thickness poly-silicon/nickel/titanium multi-layers (check the table in Figure 4.41) were deposited on each wafer[*]. Finally, the wafers devoted to device fabrication (wafers 1, 3, 5, 7 and 8) were patterned by means of photolithography and RIE. Non-patterned wafers (wafers 2, 4 and 6) were used to study the nickel silicide formation.

B) Nickel silicide formation

The nickel silicide forms by the diffusion of nickel and silicon. When a silicon/nickel multi-layer is heated above 450ºC a nickel monosilicide phase is formed and, when temperature overpasses 750ºC, nickel disilicide formation is obtained if enough silicon can be found on the sample. The nickel disilicide phase is stable up to temperatures higher than 900ºC [82].

Based on previously reported by the hosting group results on the formation of nickel silicide and taking into account achieved CNT synthesis, a new set of samples was prepared (samples type 2, 4 and 6 in the table in Figure 4.41) aiming, mainly, to achieve synthesis of small diameter CNTs. A rapid thermal annealing process with steady steps at two temperatures, 500ºC and 800ºC, was designed. The step at 500ºC aimed the formation of a uniform and homogeneous monosilicide layer and the step at 800ºC aimed to resemble the catalyst activation step of the CVD process. The annealing processes were performed in argon ambient.

Figure 4.42 shows the X-ray diffraction patterns for the three different poly-silicon / nickel configurations. The peaks were related in all cases, as expected, to the formation of nickel disilicide.

[*] Deposition of thinner poly-silicon and nickel layers was attempted without success because of equipment limitations.

Figure 4.42. X-ray diffraction analyses of three different poly-silicon/nickel multi-layer configurations after the rapid thermal annealing process.

C) CNT synthesis

Two different approaches of CNT synthesis were analysed. On the one side, expertise on SWCNT synthesis by RTCVD was applied for thermal CVD synthesis of SWCNTs by methane. On the other side, NDL's expertise on CNT synthesis was applied for the optimisation of the growth conditions by ethylene. Samples from wafers type 1, 3, 5, 7 and 8 from table in Figure 4.41 were used to perform these experiments.

4.4.2 CNT synthesis with methane

Different temperatures (between 800 and 900 ºC) and different process gases ratio (methane:hydrogen ratio between 5:1 and 1:0) were tested but no CNT growth was observed on the samples that were processed at NDL (Figure 4.43). However, the observation of carbon nanohorns like structures (Figure 4.43-b) suggested that, if persisted, the optimal CVD conditions could have been found. In fact, this was sustained by the fact that CNTs synthesis was achieved at CNM when using analogous substrates and analogous process parameters but the RTCVD system (Figure 4.45).

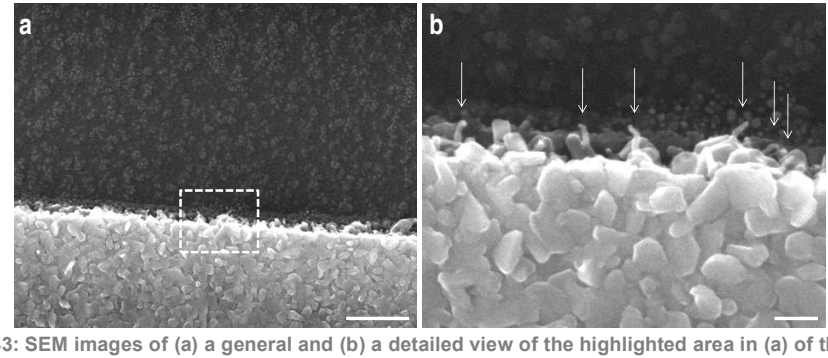

Figure 4.43: SEM images of (a) a general and (b) a detailed view of the highlighted area in (a) of the edge of a poly-silicon/nickel multi-layer after the CVD process. The higher in magnification image shows the formation of elongated short structures (they have been pointed out with an arrow). Scale bars are 500 nm and 100 nm, respectively.

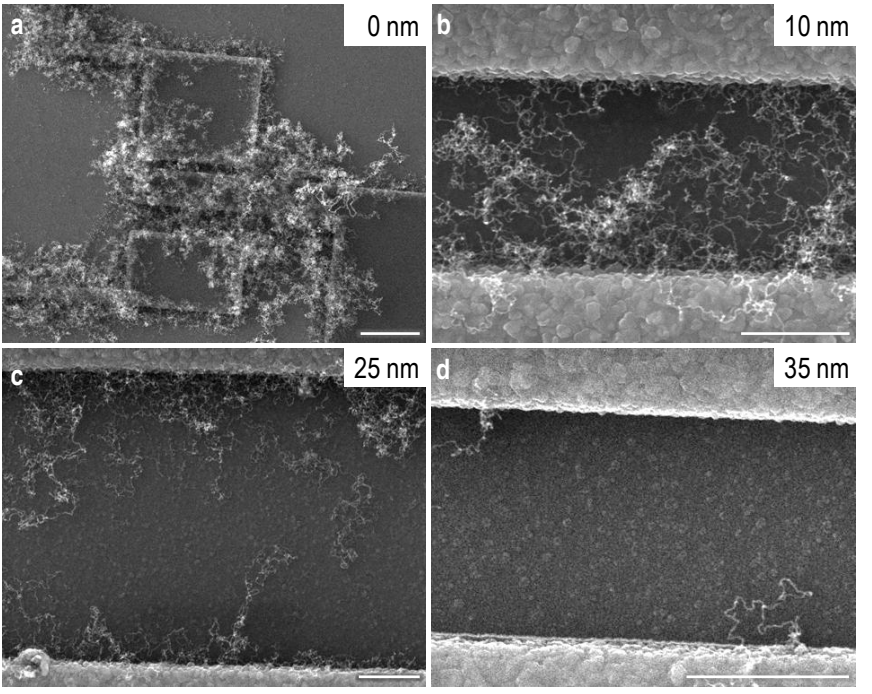

Figure 4.44: (a-d) SEM images on the synthesis of CNTs when the process includes ethylene and hydrogen during the CNT growth step and when the thicknesses of the nickel and the titanium layers are 3 and 200 nm thick, respectively, and the thickness of the poly-silicon layer is 0, 10, 25 or 35 nm in (a-d), respectively. Scale bars are 10 μm in (a) and 1 μm in (b-c).

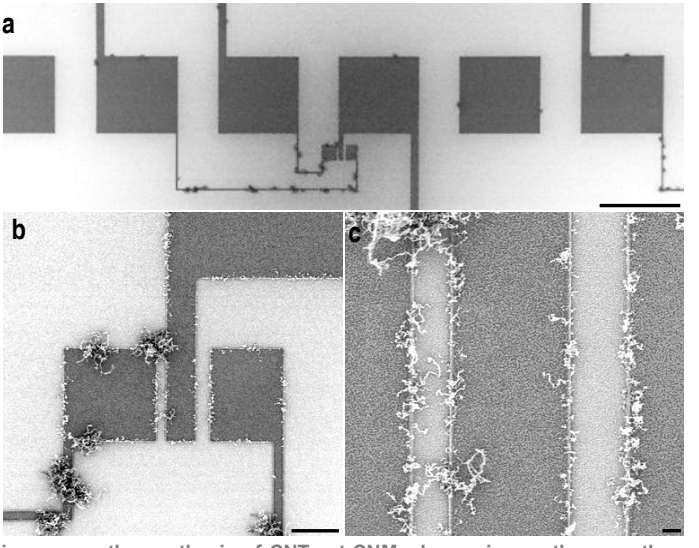

Figure 4.45: SEM images on the synthesis of CNTs at CNM when using methane as the carbon containing gas. (a) SEM image of a device. (b) Detail of the catalytic islands. (c) Higher in magnification image of the synthesized MWCNTs. Scale bars are 100 and 10 and 1 μm, respectively.

4.4.3 CNT synthesis with ethylene

The influence of the ethylene:hydrogen:nitrogen ratio during the CNT growth step and the influence of the thickness of the poly-silicon layer were found to be of great importance.

A) No nitrogen during the CNT growth step

Figure 4.44 shows SEM images on the synthesis of CNTs after a process at 750ºC with hydrogen activation of the catalyst material and an ethylene-hydrogen ratio equal to 1:20. The SEM images evidence that the density of CNTs is dependent on the thickness of the poly-silicon layer for these CNT growth conditions. The thicker the poly-silicon layer to form the catalyst material, the lower the synthesised CNT density. This dependence suggests that nickel diffuses into the silicon layer (which is in excess) and, because it gets fully embedded in silicon, it loses its capability to catalyze the growth of the CNTs. These observations are in agreement with the mechanism proposed by Esconjaregui [83].

Regarding the morphology of the synthesized CNTs, they were, in all cases, MWCNTs, and they presented defects on their structures as they did not grow straight but changing in direction continuously.

B) Nitrogen flow during the CNT growth step

Based on the previous experience of the hosting group, a process where nitrogen was injected during the growth step was designed to regulate the CNT density. The process was carried out at 750ºC, hydrogen was injected during catalyst activation step and the ratio between the ethylene, the hydrogen and the nitrogen during the catalyst growth step was set to 1:14:10.

The SEM characterization of the samples evidenced that nitrogen had a big influence on the synthesis of the CNTs since the obtained CNT morphology and distribution resembled, in all cases, that in Figure 4.44-d. Very low density of CNTs was formed. From these results, it was concluded that nitrogen reacted with the ethylene to form cyanide compounds and, thus, the carbon concentration in the chamber for the CNTs to grow diminished.

C) Directed growth of CNTs

Based on the above presented results, samples type 1 (35 nm poly-silicon / 3 nm nickel / 200 nm titanium) and the CVD process including nitrogen injection during the CNT growth step were selected for the directed growth of CNTs. During the CNT growth step, 5V were applied along the channels in order to direct the CNTs. Samples were positioned so that CNT growth direction was perpendicular to

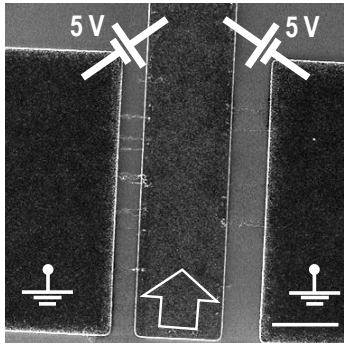

Figure 4.46: SEM image of the catalytic islands after a process where the CNT growth had been directed. Synthesized MWCNTs are the brighter lines between the islands. The voltage sources and the arrow have been drawn to illustrate the method for the directed growth of the CNTs. Scale bar is 5 µm.

the gas flow for it not to affect the growth direction of the CNTs.

Figure 4.46 shows the catalytic islands after the oriented CVD synthesis of the CNTs. CNTs are the brighter lines in between the catalytic layers. More CNTs were observed across the 2 µm gap than across the 3 µm gap because of the higher electric field (2.5 and 1.67 V/µm respectively).

The SEM images in Figure 4.47-a to Figure 4.47-c and the topographic AFM image in Figure 4.47-d show different MWCNTs bridging the catalyst islands. The CNTs tent to grow straight but they went off course because of interactions with the roughness of the substrate, which was attributed to under-etching of the catalyst layer. In many cases, it was found that CNTs growing from opposite sides of the gap collided (Figure 4.47-c). The diameter of the MWCNT in the AFM image (Figure 4.47-d) was measured to be 20 nm at the section that is marked on the image. The diameter of the CNTs was measured at that point since it seems to be in contact with the substrate.

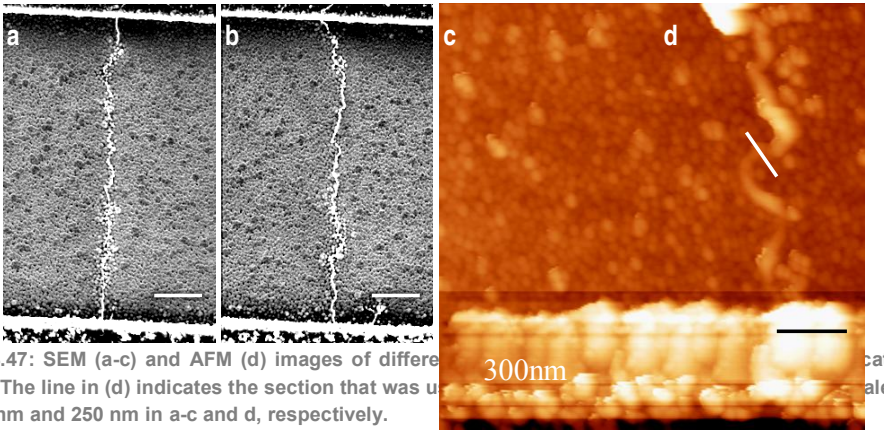

Figure 4.47: SEM (a-c) and AFM (d) images of differe catalytic islands. The line in (d) indicates the section that was u ale bars are 500 nm and 250 nm in a-c and d, respectively.

The high ratio between the intensities of the D peak (~1,350 cm^{-1}) and the G peak (~1,585 cm^{-1}) in the Raman spectrum of these MWCNTs (Figure 4.48) evidenced the formation of defective MWCNTs. This confirmed the SEM observations and was again evidenced by TEM observation of the MWCNTs. It has to be noted that the Raman spectrum in Figure 4.48 was computationally filtered because of a high noise level due to low signal intensity.

Current-voltage measurements were conducted with a 2 probe system and a semiconductor parameter analyser to evaluate the electrical response of the bridging CNTs. However, due to the non-uniformity of the samples no conclusion on the electric characteristic of the devices could be

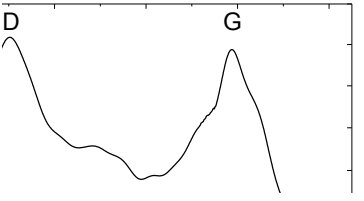

Figure 4.48: Raman spectrum of the MWCNTs that had been grown across the catalytic islands by applying an electric field. Laser: 514.5 nm; X100; 1.29 mW.

Figure 4.49: Electric characterization of a device where 8 CNTs had grown between a 2 μm channel.

extracted. Figure 4.49 shows the electric characteristic of a device where the gap between the catalyst islands was 2 μm and 8 MWCNT had been found to bridge them.

4.4.4 Conclusions on the synthesis of CNTs by nickel silicide

The experiments that have been presented in this section aimed the synthesis of SWCNTs by nickel silicide. The fact that SWCNT synthesis was not achieved is attributed to the nickel layer being too thick as it has been reported that catalyst layers not thicker than 1 nm are mandatory to synthesize SWCNTs [22, 30].

Even if SWCNT synthesis was not attained, the experiments on the nickel silicide formation and on the discussion about the CVD growth mechanism constitute a step forward to the synthesis of CNTs and, in particular, to their synthesis from silicide materials.

Optimization of the nickel deposition in combination with one of the two strategies to control CNT density and the use of the electric field to direct the CNT synthesis across the catalyst islands should lead to the synthesis of low in density and oriented SWCNTs.

Chapter conclusions

In this chapter CNT synthesis optimization by RTCVD and different iron or nickel based catalyst materials has been overviewed.

Iron nitrate has been used, first, to analyse the influence of different parameters of the RTCVD process and to study the synthesis of the CNTs on different material substrates.

- It has been demonstrated that CNT density and morphology can be controlled by selecting a specific synthesis temperature and a specific process gases ratio during the catalyst activation and the CNT synthesis steps.
- CNT synthesis on silicon, silicon oxide, silicon carbide and on silicon nitride has been achieved. CNT synthesis on Pt substrates was not demonstrated but AFM, SEM and EDX characterization of the samples showed formation of elongated structures and carbon traces on the surface.

The second section of the chapter has been devoted to explore the synthesis of CNTs when using other catalyst materials based on iron, in particular, magnetite, ferrocene, ferritin and an iron/molybdenum/alumina composite. CNT synthesis was achieved in all cases.

- CNT synthesis out of the employed magnetite particles has been determined to be analogous to previously reported CNT synthesis by iron nitrate.
- Different in structure and morphology CNT layers (different in comparison with the reported in other sections) were grown when using ferrocene and ferritin particles. CNT synthesis from ferrocene may be of special interest for device fabrication due to the very dense growth. More work is needed to control the synthesis when using these catalyst particles.
- Synthesis of SWCNTs out of iron/molybdenum/alumina has been found to be very robust as satisfactory as SWCNT synthesis was achieved for a broad range of CVD parameters. Additionally, the catalyst solution preparation is easy and its storage is possible.

Regarding the directed and constricted in diameter synthesis of SWCNTs from the channels of zeolite crystals, two different zeolites have been analysed. The main difference between these containers was related to the manner that catalyst material had been deposited in their pores. In the case of AlPO-5 zeolites, catalyst atoms substituted atoms in the structure of the crystals whereas, in the case of the L-type zeolites, the catalyst particles were introduced in their pores

- Synthesis of 0.4 Å in diameter SWCNTs has been demonstrated from AlPO-5 crystals. However, differences in the crystal morphology and the difficulty to relate the SEM and the Raman characterization of the samples hinder, at this point, the use of ALPO-5 to develop technologies to integrate SWCNTs.
- Synthesis of different carbon structures has been demonstrated when using zeolite L crystals. It has been demonstrated that the CNTs tend to grow perpendicular to the surface and straight. The fact that CNT synthesis is controllable and the fact that the crystals morphology can be made homogeneous, make of zeolite L crystals an appropriate supporting material to be used for the integration of SWCNTs into micro- and nano-technologies.

The last section has analysed a route to optimise the formation of a nickel silicide layer that would be thinner than the ones previously developed and the optimization of the CNT synthesis process to grow oriented CNTs by applying an electric field out of the compound material.

- Experiments on the nickel silicide formation determined that the silicide phase formation can only be controlled by the thicknesses of the deposited poly-silicon and nickel layers. If an excess of silicon is deposited, nickel disilicide (the undesired phase) will always be formed at the CNT synthesis temperature.
- Control over the synthesized CNT density and over the CNT growth direction was achieved by controlling the poly-silicon phase and/or the process gases and by applying an electric field. Although the synthesis of SWCNTs was not achieved, this should be possible if the nickel layer thickness would be further decreased to 1 nm or lower. More work would be needed to study this approach.

As a summary, reported in this chapter results when using iron based catalysts served to acquire expertise on the synthesis of CNTs and to optimise the RTCVD process for the synthesis of isolated SWCNT. No reproducible recipe to synthesise MWCNTs could be developed at CNM. The use of zeolite crystals has been demonstrated to be promising but further work is still needed to have the catalyst preparation and the synthesis process optimised in order to achieve total control over the density of the synthesized SWCNTs. The Studies on the synthesis of CNTs by nickel silicides have served to acquire a deeper knowledge about other CNT synthesis strategies.

5
Optimization of the CVD synthesis of carbon nanotubes by non conventional catalyst materials

For some applications it may be of great interest to synthesise the CNTs out of a material different from iron, nickel or cobalt. For example, the use of a bio-compatible or inert material as CNT catalyst would be desirable for the fabrication of devices for bio-sensing where non-biocompatible materials are rejected.

This chapter discusses the use of platinum as CNT catalyst material. Platinum was selected because it was a material that fulfils the bio-compatibility requirements and because it was already being used in the fabrication of the devices where the CNT were to be integrated (Chapter 10). However, it has to be noted that few results have been reported on the synthesis of CNTs out of non-conventional catalyst materials. Regarding the CNT synthesis by platinum, the most clear evidences are found in [9, 10] where CNT synthesis from different metals is achieved. Apart from these, CNT synthesis out of platinum is mentioned in reference [23]. Besides these works, platinum has been reported because of its ability as co-catalyst to favour the formation of the CNTs when using conventional catalyst have been most frequently reported [8].

This chapter is divided in three blocks. The first block analyses the use of different in structure platinum based particles to synthesize CNTs. Performed experiments aimed to evaluate if the developed for the conventional catalysts recipes could be used for the synthesis of CNTs from platinum based particles.

The second block reviews the attained results on the synthesis of dense arrays of vertically aligned CNT layers when using a thin platinum layer as the catalyst material. An approach to grow CNTs on a metallic substrate is proposed and the influence of the catalyst layer thickness and the influence of the CVD process parameters are discussed. Optimised in this chapter CNT synthesis recipes were used to integrate CNTs on the metal electrodes of devices for bio-sensing applications (Chapter 10).

The last block presents and discusses its growth mechanism of a novel CNT-graphene composite which may be obtained from platinum layers.

5.1 Carbon nanotube synthesis optimization by platinum particles

This section reports attained results when using platinum based particles. Two different in morphology particles were used: small diameter platinum particles and small diameter shelled platinum particles.

Used in these experiments catalyst material was prepared and deposited by researchers from the *Instituto de Tecnología Química* (ITQ, CSIC) on samples that had previously been fabricated at IMB in the frame of the CRENATUN project.

5.1.1 Small in diameter platinum particles

The first particles to be utilised were nanoscaled platinum particles. Figure 5.1 shows a TEM image of the particles and their diameter distribution. The nominal diameter was 1.9 nm.

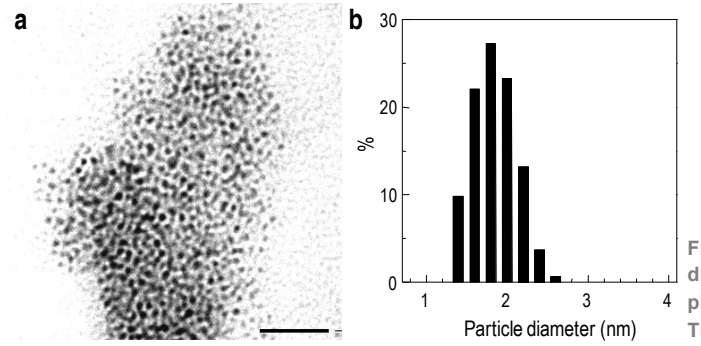

Figure 5.1: (a) TEM image and (b) diameter distribution of the platinum particles. Scale bar in the TEM image is 20 nm.

The particles were solved in chlorobenzene and spin coated on previously patterned silicon/silicon oxide substrates (Figure 5.2-a,b). This catalyst deposition was not homogeneous because the solution and spin coating parameters had not been optimised. The Raman characteristic of these particles showed no resonance that could be attributed to them in the range of the CNT resonance frequencies (Figure 5.2-c).

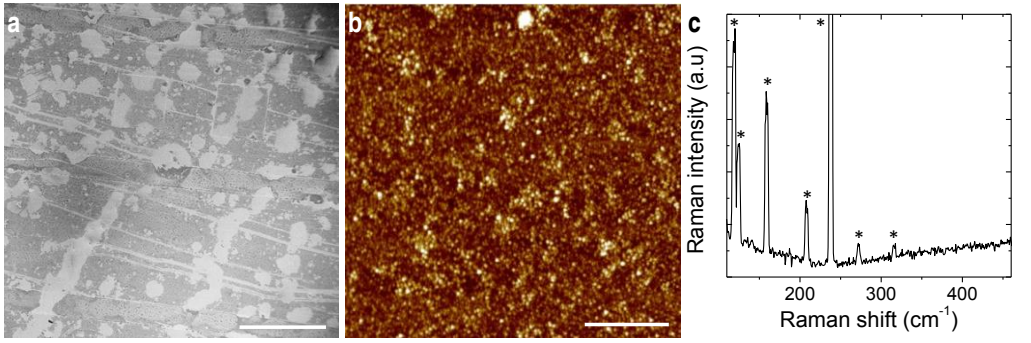

Figure 5.2: (a) SEM and (b) AFM images of particle deposition. Scale bars are 500 µm and 5 µm, respectively. Z scale in (b) is 100 nm. (c) Raman spectrum of the particles. Laser: 541.5 nm; X100; 0.5 mW.

A) CNT synthesis by platinum particles

The best results on the synthesis of the CNTs were attained at 800 ºC, when using a hydrogen flow during activation of the catalyst and only methane in the CNT growth step. The SEM image in Figure 5.3-a shows that CNT synthesis was attained on the silicon oxide and on the silicon surfaces. The fact that similar results were obtained on both materials indicates that the particles did not react with the substrates to form a platinum silicide compounds as it was expected [84, 85], or that the formation of the silicide did not affect CNT synthesis. In this sense, the analysis of the composition of the particle would be needed to confirm whether the CNTs grew out of platinum or out of the silicide compound. The density on the patterned surfaces was not high. On the contrary, as the catalyst particles were more densely deposited on the edges of the patterning due to the catalyst deposition procedure, higher in density CNT layers were also synthesized at those edges. In fact, these CNTs

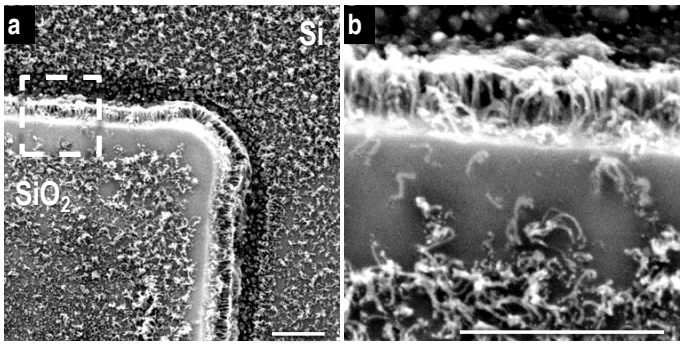

Figure 5.3: SEM images of CNTs that were synthesized out of platinum particles on a silicon/silicon oxide sample. (a) CNT synthesis around one of the patterned structures. (b) Higher in magnification image of the edge of the patterning area that is remarked in (a). Scale bars are 500 nm.

aligned perpendicular to the surface due to proximity between them (Figure 5.3-b). The diameter of the CNTs was estimated, from the SEM images, to be lower than 10 nm, and their length around 200 nm. The AFM characterization of the CNTs was not conclusive because of their short length, their density and because they did not grow parallel to the surface.

SEM image in Figure 5.4 shows that thinner in diameter CNTs were also synthesized on analogous samples (same catalyst material and same CVD process). Differences between the samples were mainly attributed to the non-uniformity of the catalyst deposition though they could also be due to non-uniformities of the temperature during the CNT synthesis process.

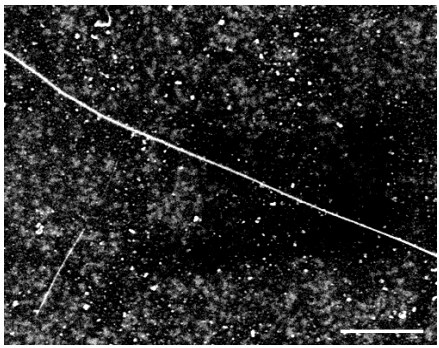

Figure 5.4: (c) Synthesized on silicon oxide isolated (SW)CNT. Scale bar is 500 nm.

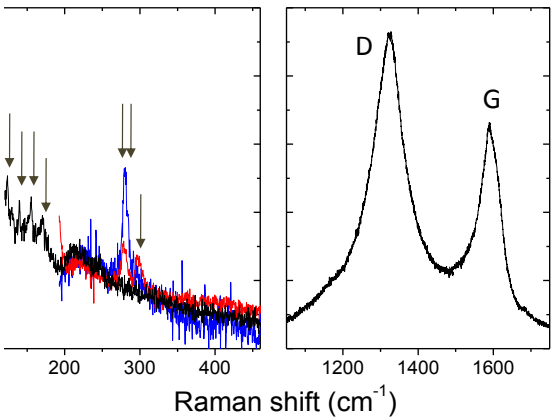

Figure 5.5: Raman spectra of different points of the sample where SWCNTs had been synthesized out of platinum particles at different positions on the sample. Laser: 614.7 nm; X100; laser power between 1.48 and 3.2 mW.

Raman spectroscopy of the samples where thinner CNTs had been observed were analysed by Raman spectroscopy (Figure 5.5). Raman revealed resonance peaks in the RBM. Those resonances, which were not related to plasmas, were associated to SWCNT growth. Strong in intensity D (1350 cm^{-1}) and D' (1620 cm^{-1}) peaks with respect to G peak indicated that defective graphitic flakes and amorphous carbon had also been deposited during the CVD process.

5.1.2 Small diameter shelled platinum particles

The same platinum particles as in the previous case were functionalized with a sulphur compound that acted as a stitching layer when the particles were put in contact with TEOS ($Si(OC_2H_5)_4$) similarly to described in [86]. The schematic of the resultant particles is shown in Figure 5.6-a. The TEM image in Figure 5.6-b shows particle aggregates.

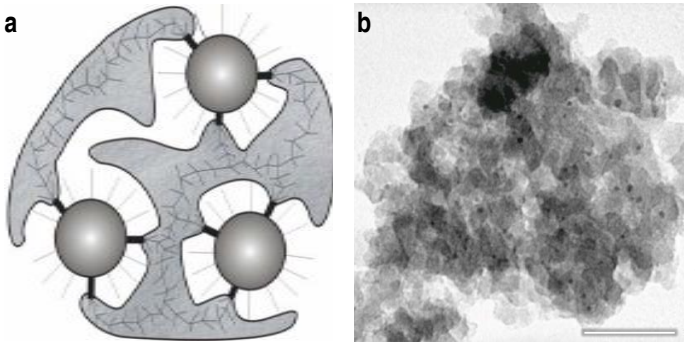

Figure 5.6: (a) Schematic of the platinum shelled particles. (b) TEM image of the synthesized particles. Scale bar in the TEM image is 50 nm.

The catalyst material was spin coated on platinum substrates (Figure 5.7-a,b) to analyse both, the CNT synthesis from the platinum particles, and the capability of the TEOS shell to prevent the diffusion between the platinum forming the particles and the platinum forming the substrate. The SEM image in Figure 5.7-a shows the catalyst material after its deposition on the surface of a sample. According to the AFM characterization of the particles (Figure 5.7-b), their diameter was 20 nm before the CVD process. The Raman spectrum of the deposited particles (Figure 5.7-c) showed two specific resonances at 134.4 cm^{-1} and at 140.4 cm^{-1}. Marked with asterisk peaks correspond to plasma lines.

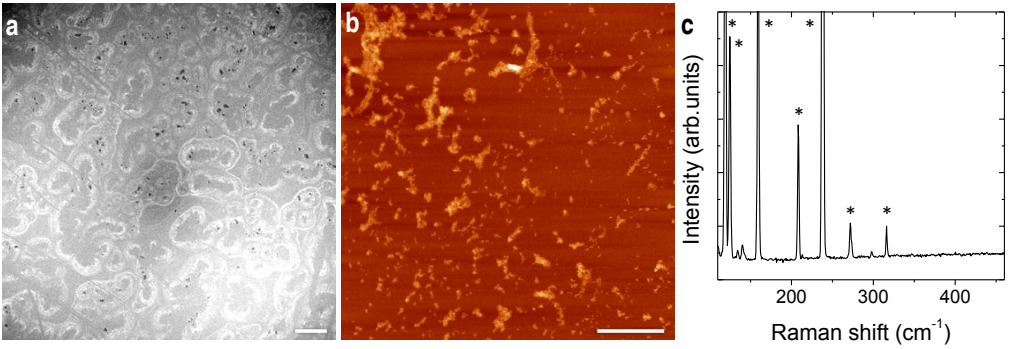

Figure 5.7: (a-b) SEM and AFM images of the platinum shelled particles after they had been deposited on the platinum substrate. Scale bars are 200 µm and 2 µm, respectively. Z scale in (b) is 100 nm. (c) Raman spectrum of the shelled platinum particles. Laser: 514.5 nm: X100; 0.4 mW.

A) CNT synthesis by silicon oxide shelled platinum particles

Similar CVD parameters to those used in the case of the platinum particles were applied but no CNT was observed after the synthesis process on samples containing TEOS shelled platinum particles. SEM (Figure 5.8) and AFM images of the samples showed that the roughness of the surface (which was platinum) had increased because of the high temperature CVD process. Regarding the catalyst material islands, no apparent change in their morphology was observed (Figure 5.8-b,c).

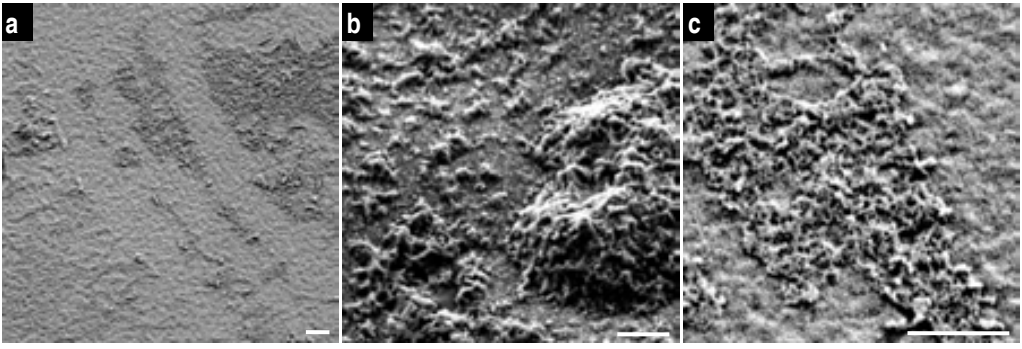

Figure 5.8: SEM images of the surface of the samples where platinum shelled particles had been deposited after the CVD process. Scale bars are 1 μm.

Figure 5.9 shows the Raman spectrum that was obtained at different points of the sample after the RTCVD process. Four resonances at the RBM (100 – 500 cm^{-1}) frequencies and two broad resonances at ~1,350 and at ~1,585 cm^{-1} are observed. However, these resonances do not correspond to SWCNTs but to platinum silicide [87], which must have formed during the RTCVD process because of the reaction between the platinum from the particles or from the substrate and the TEOS forming the shell. The peaks at high frequencies are evidence of carbon deposition and could be indicative of MWCNT formation. However, as SEM and AFM had given no evidence and due to their weak intensity, is it most probable for the resonances to correspond small graphitic flakes that deposited during the synthesis process.

Figure 5.9: Raman spectrum of the sample where shelled platinum particles had been deposited after the RTCVD synthesis process. Laser: 514.5 nm; X100; 0.72 mW.

5.1.3 Conclusions on the synthesis of CNTs by platinum particles

This chapter has presented the achieved advances in the RTCVD synthesis of CNTs from different in morphology catalysts particles based on platinum. Two different in morphology platinum particles have been used.

The first catalyst particles consisted in platinum particles with a nominal diameter of 1.9 nm. RTCVD optimization when using these particles has led to the synthesis of MWCNTs and SWCNTs but not to the control of the CNT structure. The main hitch for not attaining this control was attributed to the non-optimized catalyst deposition procedure. Therefore, the optimization of the catalyst deposition steps to achieve a homogeneous and uniform distribution of the catalyst particles should lead to a CNT synthesis similar to those attained for the ferric nitrate catalyst.

The second catalyst particles consisted in TEOS shelled platinum particles. In this case, the CNT synthesis process resulted in the formation of a platinum silicide. Since this reaction may not be avoided, these particles are not convenient for CNT synthesis unless the CNT growth temperature is significantly decreased.

5.2 Carbon nanotube synthesis optimization by thin platinum layers

Growth of CNTs out of a pre-patterned catalyst layer is the most controllable and uniform strategy to achieve the synthesis of homogeneous CNT layers and, thus, it is the most appropriate strategy to integrate arrays of CNTs on devices. Besides the catalyst deposition method, if the CNTs are to be grown on a metallic substrate, diffusion of the catalyst material to the substrate has to be taken into account (the influence of the CVD process parameters on the diffusion of nickel into silicon was discussed in section 4.4).

This section describes advances on two aspects. On the one side, the section discusses about the optimization of a platinum layer and of the RTCVD conditions to achieve the synthesis of high density of vertically aligned CNT layers. On the other side, the section presents a strategy to inhibit the catalyst material diffusion to a metallic substrate, in particular, a platinum substrate, by means of a thin silicon oxide layer. Advances on both aspects are applied in Chapter 10 for the modification of previously reported metallic microelectrodes [88, 89].

5.2.1 Substrate preparation and catalyst deposition

The sample fabrication process was divided in two steps: substrate and catalyst fabrication. Two different types of samples were used, patterned and un-patterned samples. When the layers forming the substrate and the catalyst were not patterned, CNT synthesis was possible on the whole surface of the sample. On the contrary, when the patterned substrates were used (fabrication process is described in Chapter 10) CNT synthesis only took place where the catalyst had been deposited.

A) Substrate fabrication

Substrates where CNTs were to be synthesized consisted of a 150 nm thick platinum layers that had been deposited on silicon wafers that had previously been thermally oxidised. A 30 nm thick titanium layer was deposited between silicon oxide and platinum to improve the metal adherence to the substrate (Figure 5.10-a). A 3D topographic AFM image of the surface of the platinum layer (Figure 5.10-b) shows the roughness of the metal layer. The root mean squared roughness (R_{RMS}) was measured to be 6.03 nm.

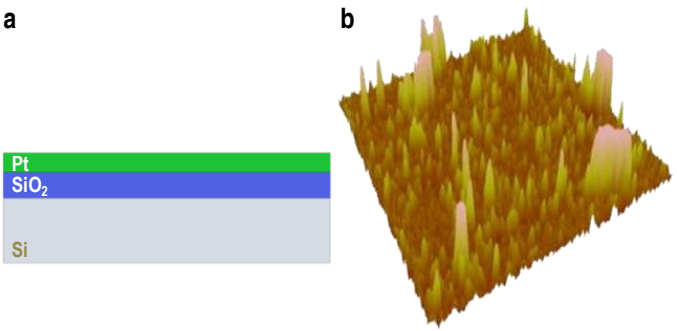

Figure 5.10: (a) Schematic of the layers forming the substrates. (b) 3D AFM image of a 2x2 μm^2 area of the surface of the sample. X,Y: 2 µm; Z: 30 nm.

B) Catalyst deposition

The substrate material being a metal implied that the catalyst and the substrate materials could react between them, especially in this case where the catalyst and the substrate were both platinum. To avoid any possible reaction and to enhance smaller catalyst particle formation, a 15 nm thick silicon oxide layer was deposited by PECVD similarly to [90], prior to the platinum to form the catalyst layer. Finally, a 4 nm thick platinum layer was typically deposited by sputtering. 8, 3, 2 and 1 nm thick platinum layers were also studied (section 5.2.4).

Figure 5.11-a shows the schematic of the substrate after silicon oxide and platinum deposition. Figure 5.11-b is a 3D topographic AFM image of the surface of the platinum layer forming the catalyst. In this case, the root mean squared roughness was calculated to be 0.913 nm. The decrease of the roughness of the surface with respect to the previous step was attributed to the silicon oxide coverage of the substrate.

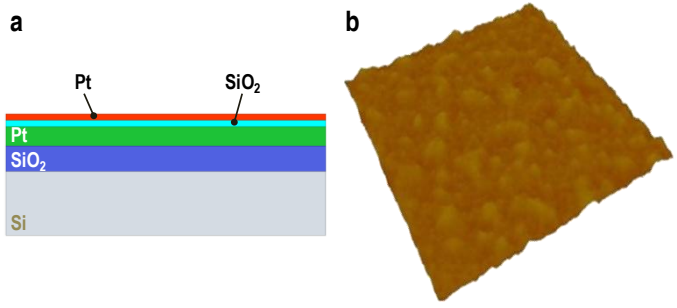

Figure 5.11: (a) Schematic of the layers forming the substrate and the catalyst. (b) 3D topographic AFM image of the surface of the sampole. X,Y: 1 µm, Z: 30 nm.

5.2.2 CNT synthesis by platinum layers

As previously described in section 4.1.2, the CNT synthesis process is composed of two main steps: the catalyst activation step and the CNT growth step.

A) Catalyst activation step

The schematic of the sample just after the activation step is shown in Figure 5.12-a. On the one side, the heating during the catalyst activation step increases the roughness of the platinum forming the substrate and the roughness of the thin silicon oxide layer that may even crack. In addition to the roughness increase, silicon oxide prevents diffusion between the metal forming the substrate and the metal forming the catalyst layer. On the other side, because of its thickness, the 4 nm thick platinum

layer breaks into particles when heated above 500ºC. The morphology of the particles as well as the distance between them depends on the layer thickness and on the substrate roughness [25, 91, 92].

The optimised catalyst activation step consisted in increasing the chamber temperature up to 800ºC in two minutes and in maintaining that temperature for another three minutes. The activation was performed in hydrogen atmosphere. Under these conditions, the diameter of the particles was found to be between 20 and 40 nm and the distance between them around 100 nm (Figure 5.12-b,c). The root mean squared roughness was calculated to be 7.98 nm.

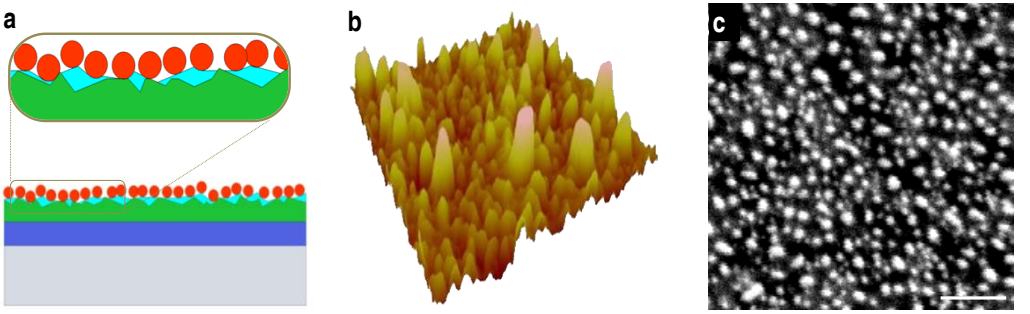

Figure 5.12 (a) Schematic, (b) AFM and (c) SEM characterizations of the samples after the catalyst activation step. The AFM image is 1 x 1 μm^2. Z scale is 30 nm. Scale bar in the SEM image is 200 nm.

B) CNT growth step

Figure 5.13 is a schematic of the CNT formation. The CNTs form out of the catalyst particles and their diameter will depend on the catalyst island diameter. If the catalyst particle density is high enough, the CNTs will align perpendicular to the surface of the sample [93]. As shown in the schematic, CNTs are expected to be in contact with the metal forming the substrate because of the cracking of the silicon oxide inter-layer.

Optimal results on CNT synthesis were achieved when the growth temperature was set to 800ºC and the growth step was divided in two steps, the first one presenting a low methane-hydrogen ratio and the second one with no hydrogen. Although different experiments were performed to analyse the influence of both steps in the formation of the CNTs no conclusion was attained. However, it is most probable that the first step favours nucleation of the carbon around the catalyst particle and hinders carbon saturation, and that the second step enhances CNT growth.

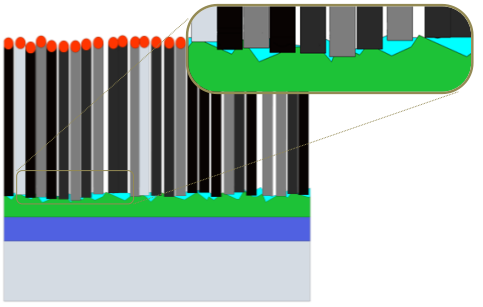

Figure 5.13: Schematic of the different layers forming the sample after the CNT growth step.

5.2.3 Characterization of the synthesized vertically aligned MWCNT layers

Synthesis of dense, uniform and homogeneous CNT layers was achieved at 4 inch wafer level. Figure 5.14 shows two samples before (Figure 5.14-a) and after (Figure 5.14-b) the RTCVD synthesis of the CNTs. Matt black colour of the sample on the right gives evidence of the formation of a uniform and dense CNT layer at chip level (2 x 2 cm^2). Wafer level synthesis of the MWCNT arrays is shown in Chapter 10, where dense arrays of CNTs are integrated into metallic electrodes.

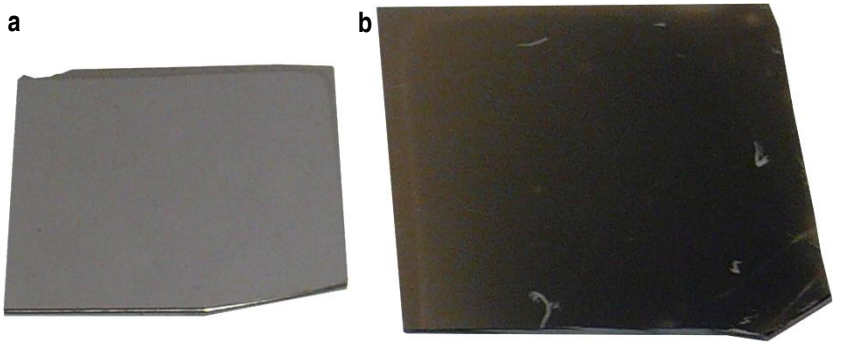

Figure 5.14: Photographs of two samples that were used in the experiments on CNT optimization. (a) Sample before the CVD process. (b) Sample after the CVD process. Sample on the right is 2 x 2 cm^2.

Figure 5.15 shows SEM images of the synthesized MWCNTs. According to the curved shape of the CNT array in Figure 5.15-a, it seems that it had grown in spaghetti configuration. However, lateral view in Figure 5.15-b shows, clearly, a perpendicular alignment of the CNTs with respect to the surface. In this case, vertical alignment of the CNTs was not achieved because of proximity between them but because of the formation of a top CNT crust. This crust formed because of the spaghetti configuration of the CNT layer, and ended by inhibiting growth of the CNTs parallel to the surface and forcing the CNTs to grow perpendicular to the surface all together [33].

With respect to the CNT growth mechanism, it was not concluded whether it was base or tip growth since catalyst particles were observed at both sides of the CNTs (Figure 5.15-b to Figure 5.15-d) and Figure 5.16-a). The fact that the particles on the CNT tips looked too big to be the catalyst particles (as the diameter of the CNT should, in theory, be similar to that of the particle it grows from) suggests base growth mechanism. However, extrusion of the metal particles at the separated from the substrate tip (Figure 5.15-d) and the observation of metal particles in the central part of the MWCNTs may indicate tip growth or even a simultaneous base and tip growth.

TEM observation of the CNTs (Figure 5.16) confirmed they were MWCNTs with diameters ranging between 5 and 20 nm and that their length typically ranged between 1 and 1.5 µm.

A) Graphitization of the MWCNTs and impurity deposition

The graphitization of the MWCNTs and the amorphous carbon deposition around them was analysed by TEM and Raman microscopy.

Regarding the structure of the MWCNTs, their TEM imaging (Figure 5.16) suggested that they were low defective and that their walls were parallel to the MWCNT axis. The distance between the graphitic layers was measured to be 0.34 nm. Characteristics of the D (~1,350 cm^{-1}), G (~1,585 cm^{-1}) and G' (~2,700 cm^{-1}) peaks in the Raman spectra of the CNT (Figure 5.17) corroborated the

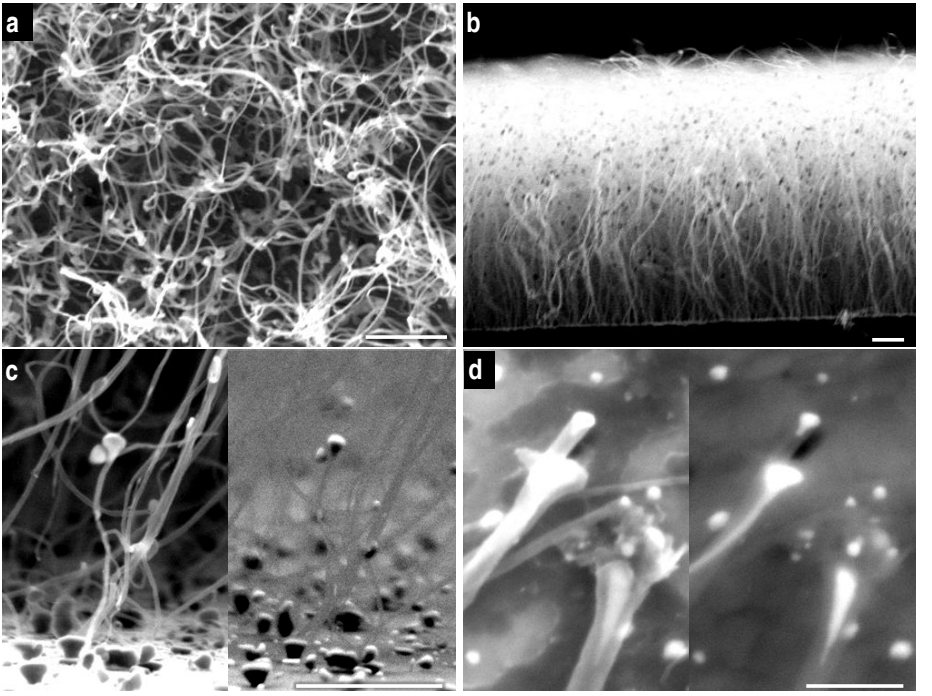

Figure 5.15: SEM images on the synthesized out of platinum layers MWCNTs. The image in (a) and left side images in (c) and (d) were made with the SE2 detector. Image in (b) and right side images in (c) and (d) were made with the InLens detector. Scales bars are 500 nm in (a-c) and 100 nm in (d).

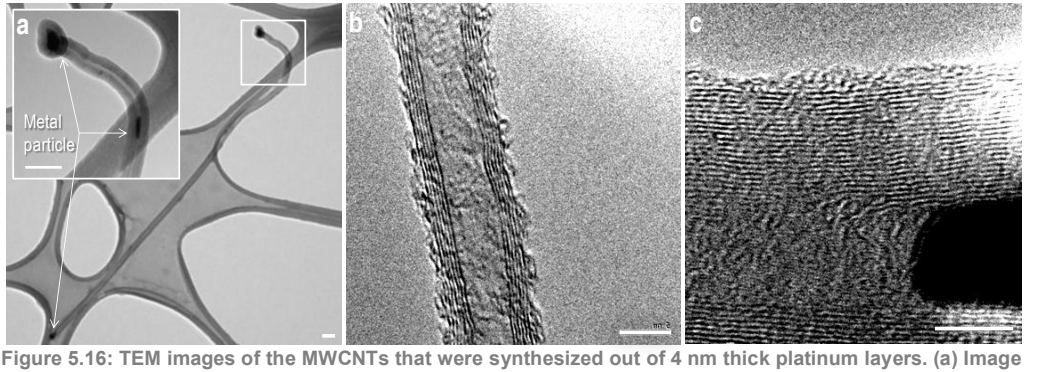

Figure 5.16: TEM images of the MWCNTs that were synthesized out of 4 nm thick platinum layers. (a) Image of a sole MWCNT. Metal particles are observed at both edges and inside the tube. (b) Image of the core of a 8 nm thick MWCNT. (c) Detail of the graphitization level of a MWCNT and of a metal particle inside the core of the tube. This MWCNT is 19 nm in diameter. Scale bars are 50 nm in (a) and 5 nm in (b) and (c).

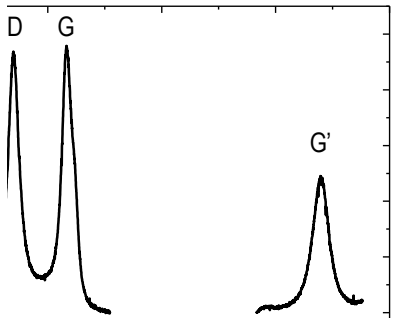

Figure 5.17: Raman spectrum (top view) of the MWCNT layer that was synthesized out of a 4 nm thick platinum layer. Laser: 514.5 nm; X100, 0.74 mW.

synthesis of MWCNTs. The ratio between the intensities of the G' and G peaks, which is indicative of the graphitization, is not high but the fact that Raman measurements were performed from a top view (the edges and, thus, the most curved and defective sections of the CNTs) and not from a lateral view (the straighter section of the CNTs and, thus, their less defective section) is taken into account, it can be concluded that the graphitization of the MWCNT was high [94-96].

The TEM observation showed, also, that the CNTs were most often covered by a thin layer of impurities that was, most probably, amorphous carbon (Figure 5.16-b). Additionally, bigger material aggregates around the MWCNTs were also observed, but these aggregates were not related to amorphous carbon deposition but to contamination from the preparation of the TEM solution. Regarding the analysis of the Raman spectra, the high intensity of the D peak with respect to the G peak indicates the presence of amorphous carbon on the walls of the MWCNTs [94, 95, 97].

5.2.4 Influence of the CNT synthesis parameters

Different variations on the CNT synthesis process were analysed. This section focuses on the optimization of the catalyst pretreatment step and the platinum catalyst layer thickness to achieve different in configuration and/or morphology CNT layers.

A) Influence of the catalyst pretreatment temperature

The capabilities of the RTCVD system (section 2.1.1) were taken into advantage to design a catalyst activation step with a Dirac-delta shape similar to the one described in section 4.3.2 (Figure 5.18).

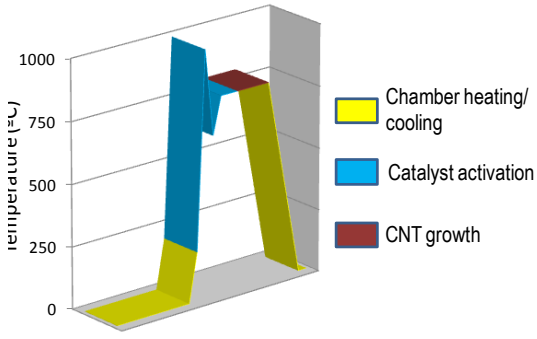

Figure 5.18: Schematic of the CNT synthesis RTCVD process including the Dirac-delta heating during the catalyst activation step.

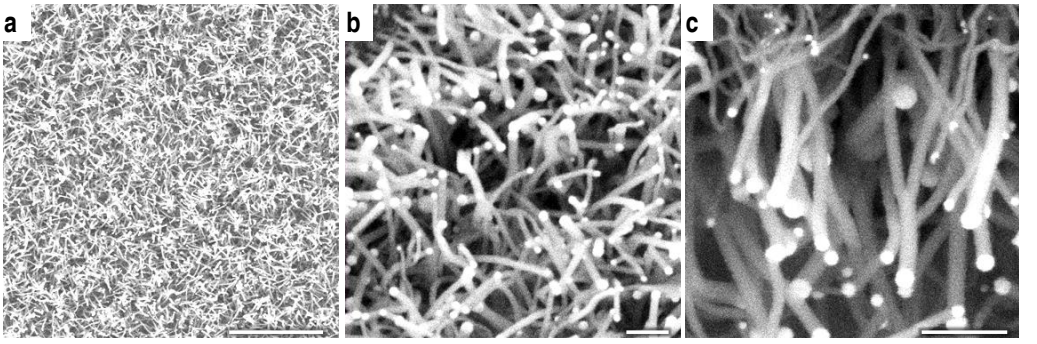

Figure 5.19: SEM images of the carbon structures that were obtained when the Dirac-delta like heating was included to the activation step. (a) Carbon structures layer. (b) Higher in magnification image of part of the layer in (a). (c) Detail of the structures and evidence of heterogeneous distribution of diameters. Scale bars are 2 μm in (a) and 200 nm in (b) and (c).

The maximum temperature during activation reached 1000ºC.

The SEM images in Figure 5.19 show part of the carbon structure material that was obtained when using a 4 nm thick platinum catalyst layer and the Dirac-delta activation was applied. In this case, larger in diameter structures were synthesized in a similar way to what had been observed when the Dirac–delta step had been used for CNT synthesis from zeolites (section 4.3.2) because of the aggregation of the catalyst material. The SEM images evidenced that the diameters of these structures was not homogeneous. Diameters up to 50 nm were measured. Non homogeneity of the diameters was related to different in diameter platinum aggregate formation during the Dirac-delta pretreatment because of a heavy migration of platinum on the surface during the fast heating of the samples. The fact that the structures grew perpendicular to the surface could be due to the structures being larger in diameter MWCNTs or, as shown in [98] for gold particles, to the formation of carbon nanowires instead of CNTs for the larger diameter catalyst particles.

B) Influence of the catalyst layer thickness

Specific samples were prepared to analyse the influence of the catalyst layer on the structure and the morphology of the synthesized CNTs. 8, 3, 2 and 1 nm thick platinum layers were selectively deposited on previously patterned samples (section 10.2). The 8 nm thick layer was deposited by sputtering whereas the other layers by evaporation.[*]

Figure 5.20 and Figure 5.21 summarise the attained results when synthesizing CNTs out of the different catalyst layers. Figure 5.20 refers to the morphology and distribution of the catalyst particles on the surface of the sample and Figure 5.21 to the CNT synthesis out of those particles respectively. Comparison of the grown CNTs with the results that had been obtained when depositing a 4 nm thick platinum layer (Figure 5.15) evidenced that the catalyst layer thickness highly affects the catalyst particle morphology and their distribution on the surface and, thus, it determines the morphology of the CNT layer to be obtained.

(i) Platinum layer thickness influence on the catalyst particle formation

Figure 5.20 shows SEM images of different in thickness platinum layers (8, 3, 2 and 1 nm) after a catalyst activation step at 800ºC in hydrogen atmosphere. SEM images evidence that, as expected

[*] Platinum evaporation was performed at the *Laboratori de Capes Primes* of UAB.

from references [25, 91, 92], the thinner the platinum layer, the smaller in diameter and denser in distribution the catalyst particles that are obtained after the activation step. Observed particle diameter was homogeneous and adequate for the formation of CNTs in the cases of the 3, 2 and 1 nm thick platinum layers (Figure 5.20-b to Figure 5.20-d). Besides the particle diameter, particle to particle distance was measured to be around 75 nm for the 3 nm thick platinum layer case and lower for the 2 and 1 nm thick cases. On the other hand, in the case of the 8 nm thick platinum layer (Figure 5.20-a) the particle diameter was shown to be not homogeneous and large platinum islands were even observed.

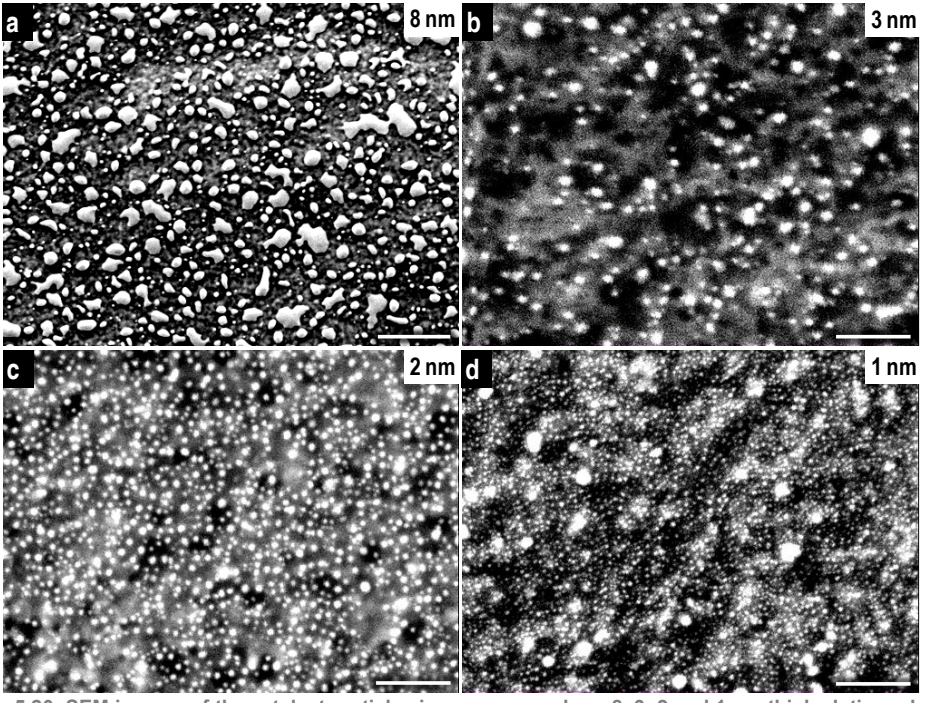

Figure 5.20: SEM images of the catalyst particles in processes where 8, 3, 2 and 1 nm thick platinum layers had been deposited on platinum/silicon oxide substrates. Scale bars are 1 µm in (a) and 200 nm in (b-d).

(ii) Platinum layer thickness influence on CNT synthesis

Regarding CNT synthesis, SEM micrographs in Figure 5.21 served to compare CNT synthesis for the evaluated catalyst layer thicknesses. As it could be expected from the catalyst nanoparticle observation, dense CNT layers were obtained in all cases except for the 8 nm thick platinum layer case, where only few dispersed CNTs were observed (Figure 5.21-a).

The CNT layer that was synthesized out of a 3 nm thick platinum layer (Figure 5.21-b,c) was observed to be analogous to that obtained out of a 4 nm thick platinum layer (Figure 5.15). Again, dense arrays of MWCNTs aligned vertically due to their impossibility to grow parallel to the substrate because of the formation of a CNT top crust. Additionally, SEM imaging of the CNTs showed that the metal particles in the upper tip of the CNTs were smaller to the ones observed when using the 4 nm thick catalyst layer. This size diminution was related to the fact that the formed platinum particles were smaller in diameter.

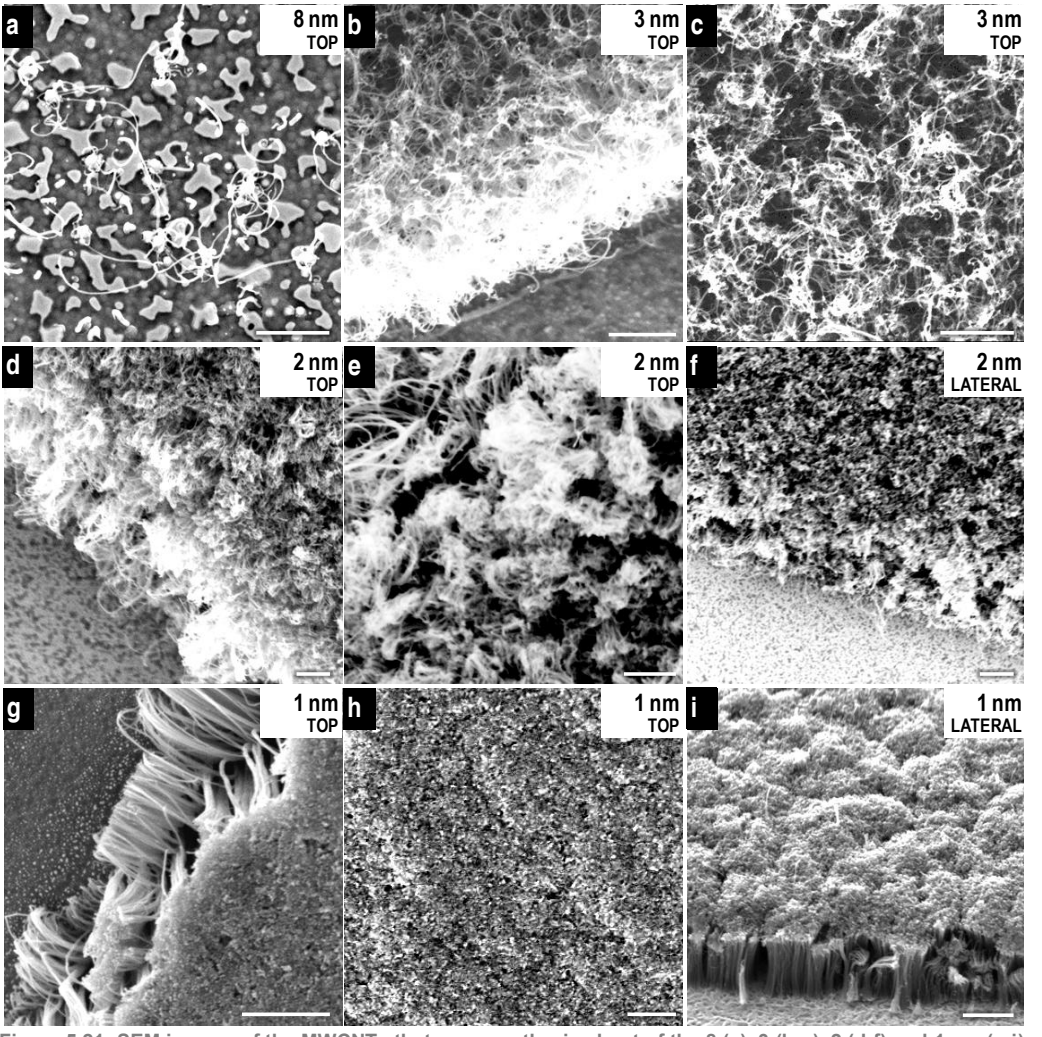

Figure 5.21: SEM images of the MWCNTs that were synthesized out of the 8 (a), 3 (b-c), 2 (d-f) and 1 nm (g-i) thick platinum layers. All the images are a top view of the MWCNTs except for images (f) and (i). Scale bars are 500 nm.

Characterization of the CNTs that had been synthesized out of a 2 nm thick platinum layers (Figure 5.21-d to Figure 5.21-f) showed the formation of very dense arrays of MWCNTs that aligned perpendicular to the substrate not because of a top crust inhibiting horizontal growth (as in the 4 and 3 nm thick platinum layer cases) but because of the very dense CNT synthesis inhibited parallel to the surface growth. The MWCNT layer was estimated to be 1 µm thick.

Observation of the CNTs that had been synthesized out of a 1 nm thick platinum layer (Figure 5.21-g to Figure 5.21-i) confirmed the tendency in the CNT alignment mechanism. In this case, MWCNTs aligned perpendicular to the surface in a similar way to that discussed for the 2 nm thick layer case but, as a result of the even denser particle distribution, synthesized MWCNTs grew straight. The height of the MWCNT layer was measured to be more than 1 µm as in the previous cases.

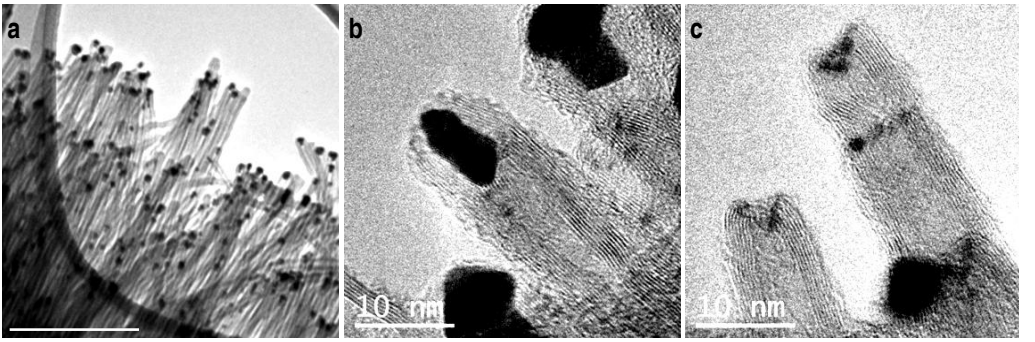

Figure 5.22: TEM images of the MWCNTs that had been synthesized out of a 1 nm thick platinum layer. (a) Bundle of MWCNTs. (b) Detail of one of the edges of the MWCNTs. (c) Detail of the other edge of the MWCNTs. Scale bars are 200 nm in (a) and 10 nm in (b) and (c).

A more in detail characterization of the MWCNTs that had been grown out of the 1 nm thick platinum layers is shown in Figure 5.22 and Figure 5.23. The fact that bundles of perfectly aligned MWCNTs and no sole MWCNT were observed by TEM (Figure 5.22-a) evidenced strong interactions between the CNTs

The diameter of these MWCNTs was measured to be 12 ± 2 nm, analogous to the measured diameters when MWCNTs had been synthesized out of 4 nm thick platinum layers (section 5.2.2), but more homogeneous as a consequence of the more uniform catalyst particle distribution. The diameters being similar in both cases evidenced that the catalyst layer thickness highly affects the CNT distribution but not so much their diameter distributions as it was expected from the previously acquired expertise (section 4.1.4).

In the case of the 1 nm thick platinum layers, metal particles were only detected at one of the tips of the CNTs (Figure 5.22-b,c), unlike for the 4 nm platinum layer case, where metal particles had been found on both edges and in the middle of the CNTs. The diameter of these particles was less than 10 nm. Measured from the TEM images graphene interlayer distance was confirmed to be 0.34 nm.

High graphitization of the CNT layers and little amorphous carbon deposition on the sidewalls of the

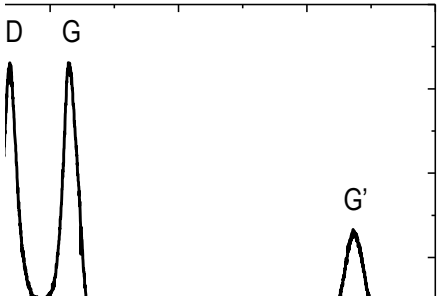

Figure 5.23: Raman spectrum of the synthesized out of a 1 nm thick platinum layer. Laser: 514.5 nm; X100; 0.75 mW,

CNTs was observed by TEM. Opposite conclusions were extracted, on the contrary, out of the Raman spectra of the samples (Figure 5.23) since the G' peak (~2,700 cm^{-1}) intensity against the G peak (~1,585 cm^{-1}) intensity was not very high and since the D peak (~1,350 cm^{-1}) was intense with respect to the G peak. However, as discussed for the 4 nm thick layer case (section 5.2.3), as the top observation of the CNT layer does not give real information of the core of the CNTs but only of their top sections (specially in the case of the CNT layer that was obtained from the 1 nm thick platinum layer because of its vertical alignment) these Raman spectra were not taken into consideration.

5.2.5 Conclusions on the synthesis of CNTs from platinum layers

This section has been devoted to study the viability of growing dense layers of CNTs on platinum substrates by using platinum layers as catalyst material. The main challenges comprised not only the optimization of the CNT synthesis but also the optimization of a strategy to inhibit diffusion between the catalyst layer and the substrate.

It has been demonstrated that the use of a 15 nm thick silicon oxide layer serves to inhibit diffusion and also to enhance the formation of smaller in diameter and denser and uniform platinum islands for the CNTs to grow.

Regarding the synthesis of the CNTs, dense and vertically aligned MWCNT arrays have been synthesised by platinum layers that are 4 nm thick or thinner. Furthermore, experiments on the synthesis optimization have shown that the morphology of the CNT layers can be preselected by tuning the catalyst layer thickness and the RTCVD parameters.

SWCNT synthesis has not been achieved because the appropriate for SWCNT conditions have not been established. In order to achieve SWCNT synthesis, the thickness of the platinum catalyst layer should be further decreased and, maybe, the silicon oxide interlayer should also have to be again optimised to improve the roughening of the surface and the particle formation.

5.3 Synthesis of a carbon nanotube - graphene composites by thin platinum layers

Apart from CNTs, other carbon allotropes have also generated great interest for device applications. Since it was demonstrated that graphene layers could be mechanically isolated by mechanical exfoliation of graphite [99] an increasing interest has grown in the community to develop devices based on this material. In this way, big efforts are being dedicated to the synthesis of graphene at wafer level in order to acquire the capability to massively fabricate graphene based devices [100-103].

Despite the fact that big advances have already been achieved, there are still many aspects regarding CNT and graphene synthesis that are unknown and that require efforts to be solved. These efforts, however, will not only lead to gain knowledge on CNTs and graphene but also on new materials that may even be unknown at this time. In this sense, for example, a new composite material based on MWCNTs and multi-layer graphene was recently presented [104] (Figure 5.24-a). The authors proposed that the graphene layers formed first and that, then, these layers served as a uniform support for the MWCNTs to grow with a vertical orientation. This growth mechanism is similar to that of the Odako growth (*odako* means kite in Japanese) [105] (Figure 5.24-b) or to the sandwich growth mechanism of CNTs [106].

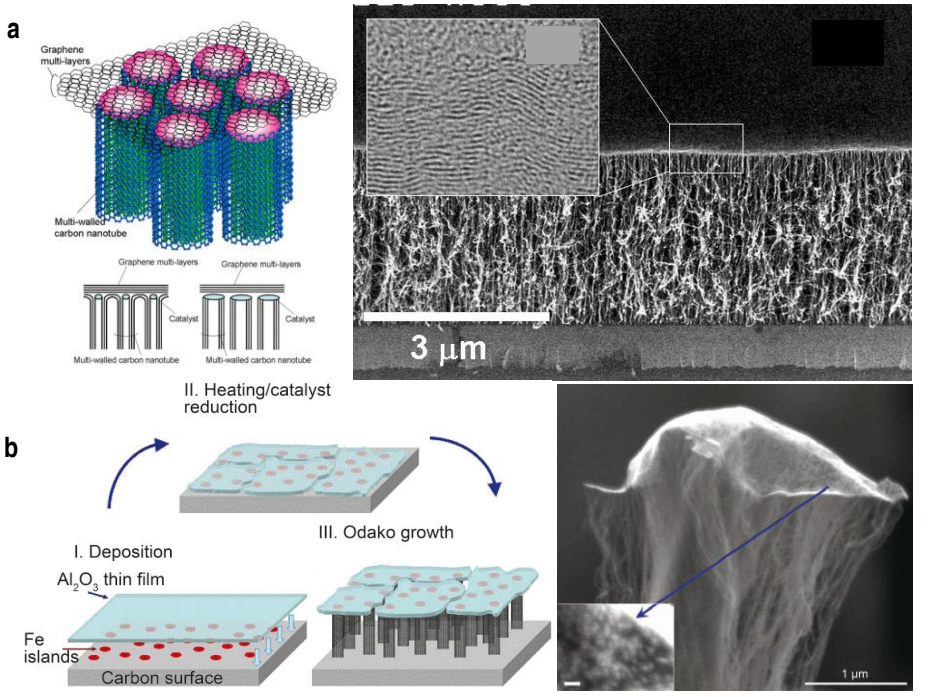

Figure 5.24: Schematics of the composite materials synthesis and SEM images. (a) CNT-multi-layer graphene composite. (b) Odako growth of CNTs by an Al2O3 layer. (b). Images from [104] and [105], respectively.

When using platinum as the CNT catalyst material (section 5.2), the formation of a layer on top of the CNTs was observed on certain samples. The top layer formation was not related to the standard process for the synthesis of dense arrays of CNTs, to the platinum thickness (since it was observed on samples where different platinum thicknesses had been deposited) or to the substrate (since it was synthesised on silicon oxide and on platinum electrodes).

This chapter summarises the results on the synthesis of this composite and discusses, based on SEM imaging, EDX analyses and Raman spectroscopy, its formation and structure.

5.3.1 Observation of the composite material

The composite synthesis, which was matt black in colour, was uniform at sample size. Different SEM images of the composite are shown in Figure 5.25. Figure 5.25-a shows a 50 x 50 μm^2 area where different alignment marks had been patterned by means of FIB[†]. The image shows how the sample (except the positions where the marks had been patterned) was covered by a top layer that seemed to be very rough. A closer look determined, however, that the layer was smooth and that the roughness was related to a CNT array underneath. Cracks in the top layer were only observed close to positions were the CNT layer had been modified because of scratches or because of squashing. Figure 5.25-b,c are SEM images of the composite after a mechanical scratch on the surface. Image in Figure 5.25-b shows how the composite was removed from the substrate and even turned around. Image in Figure 5.25-c, which is a higher magnification image of the left-hand side of Figure 5.25-b,

[†] FIB patterning was performed by Mr. Jordi Llobet Sixto at the Clean Room of IMB-CNM.

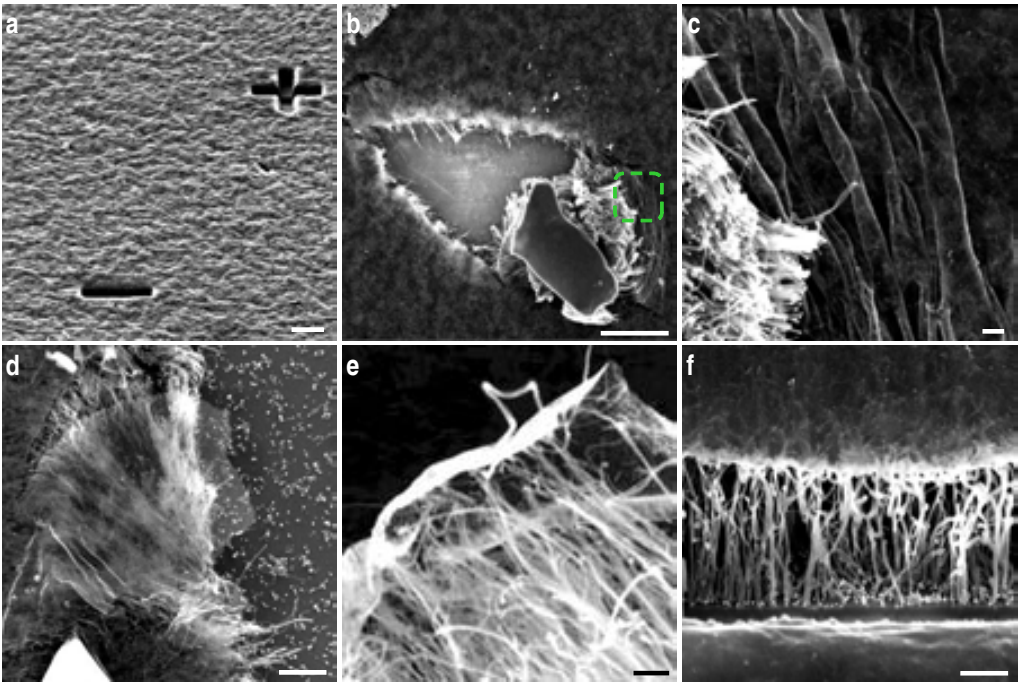

Figure 5.25: SEM images of the composite. (a) Tilted view of two alignment marks on the composite. (b) Image of a scratch on the composite layer. (c) Detail of the marked in (b) area. (d) Top layer shift with respect to the MWCNT layer. (e) Detail of the MWCNT layer in contact with the top layer. (f) High in magnification image of the composite obtained from the bottom alignment mark in (a). Scale bars are 5 µm in (a) and (b), 1 µm in (d) and 200 nm in (c), (e) and (f).

evidences that the top layer was continuous, that it had not cracked and that it had folded intensely when the mechanical force had been applied. The continuity of the layer was also corroborated by AFM.

SEM images in Figure 5.25-d to Figure 5.25-f evidenced that the top crust was a layer that formed on top of the CNT layer. The SEM image in Figure 5.25-d is a flake of the top layer that had been ripped from the CNT layer underneath and had shifted from it. Figure 5.25-e and Figure 5.25-f show detail of the CNT-top film composite and of a section made by FIB milling, respectively. CNTs in Figure 5.25-f seem to be very defective due to the used FIB milling conditions. Both images in Figure 5.25-e and Figure 5.25-f show that the top layer was in contact with the CNTs. SEM image in Figure 5.25-d evidenced that, however, they were not attached.

It has also to be remarked that during SEM imaging the top layer showed the same contrast as CNTs did when using the two detectors that are installed in the SEM system (Section 2.2.1).

5.3.2 EDX characterization of the composite

EDX (section 2.2.1) was used to determine the composition of the film on top of the MWCNTs[‡]. Figure 5.26 shows SEM images of the areas where analyses took place and the qualitative results on

[‡] EDX analyses were performed by Judith Oró at the Electron Microscopy Lab of ICMAB.

the different element detection. In this case, the composite had been synthesised on a silicon/silicon oxide substrate.

The analysis of the surface of the samples where the composite layers had been synthesized but from which it had been removed afterwards is shown in Figure 5.26-a. Highlighted in the SEM image areas were analysed to determine if carbon traces were observed after the composite removal. EDX detected very little quantity of carbon and that its proportion decreased even more with the increase of the accelerating voltage of the electron beam (4 kV up to 10 kV) suggesting its presence on the surface. No platinum traces from the catalyst material were found.

Different analyses (the accelerating voltage ranging from 4 kV to 10 kV) were performed on the CNT composite material (Figure 5.26-b). Carbon was detected as in the previous case but, this time, its proportion with respect to substrate elements resulted much higher. Measurements at 4 kV showed almost no trace of the SiO_2 from the substrate. The low platinum concentration is attributed to the catalyst material.

Last, Figure 5.26-c presents the EDX measurements on the shifted flake in Figure 5.25-d. The SEM image shows the two areas where the measurements were performed. These measurements evidenced that the carbon ratio was higher when the EDX analysis was performed on the flake (A) than when the substrate was directly evaluated (B).

Taking into account these results and the results on substrate and composite characterization, it was concluded that the top layer was formed of carbon.

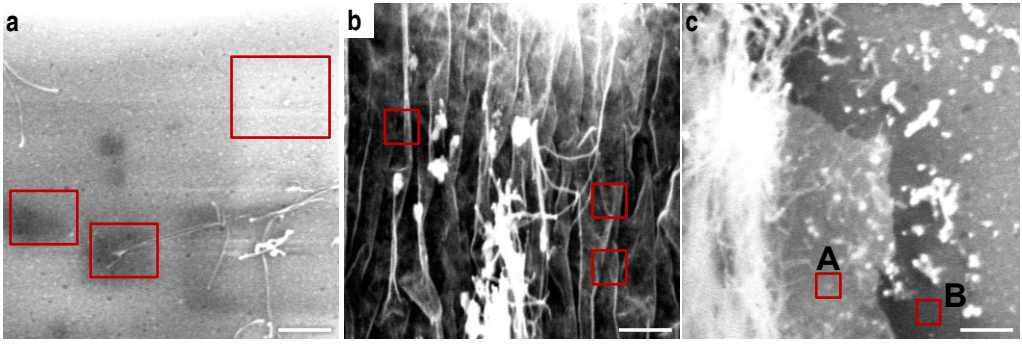

	Energy (kV)		
	4	5	10
C	7	4	3
O	40	51	51
Si	43	44	46
Pt	0	0	0

	Energy (kV)		
	4	5	10
C	82	73	59
O	7	9	16
Si	6	11	20
Pt	5	7	5

	Flake (A)	Substrate (B)
C	11	6
O	47	50
Si	41	43
Pt	1	1

Figure 5.26: SEM images of the areas where the EDX experiments were performed and tables showing the element qualitative analysis. (a) Area of the substrate where the composite had been synthesized and from which it had been mechanically removed afterwards. (b) Area where the composite material had been synthesized. (c) Detail of the shifted flake in Figure 5.25 (d). Scale bars are 10 µm in (a) and 5 µm in (b) and (c).

5.3.3 Raman characterization of the composite

Raman spectroscopy was used to determine the nature of the carbon layer on top of the CNTs. In order to identify different positions on the sample, alignment marks were patterned by FIB (Figure 5.25-a and Figure 5.25-f).

Raman analyses of the MWCNTs forming the composite are shown in Figure 5.27-a and Figure 5.27-b. In this case, the CNTs were laying on the surface because of the squashing of the composite and the removal of the top layer. Comparison of these spectra with the previously reported ones (Figure 5.17 and Figure 5.23), shows, that the intensity of the G' (~2,700 cm^{-1}) peaks was higher. As previously discussed (section 5.2.3), this difference was attributed to observation of the core of the MWCNTs (lateral view) instead of their tips (top view). Therefore, the orientation of the CNTs underneath the top layer has to be taken into account in the Raman discussion.

Raman analyses of the composite material from a top view are shown in Figure 5.27-c and Figure 5.27-d. In this case, the MWCNT layer was perpendicular to the substrate as in the spectra of the MWCNT layers in Figure 5.17 and Figure 5.23. The comparison of these spectra with the previous ones evidence an increase in the G' peak intensity for the composite material and, thus, suggest that, as the structure of the CNTs is the same as in the previous case, the graphitization of the top carbon layer must be high.

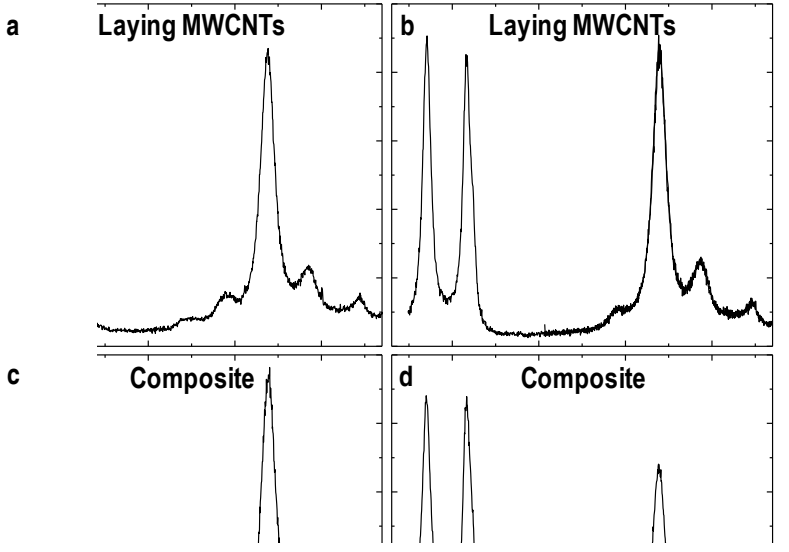

Figure 5.27: Raman spectra of the lying on the surface MWCNT layer (a-b) and of the composite material (c-d). Laser: 514.5 nm; X100; 0.85 mW.

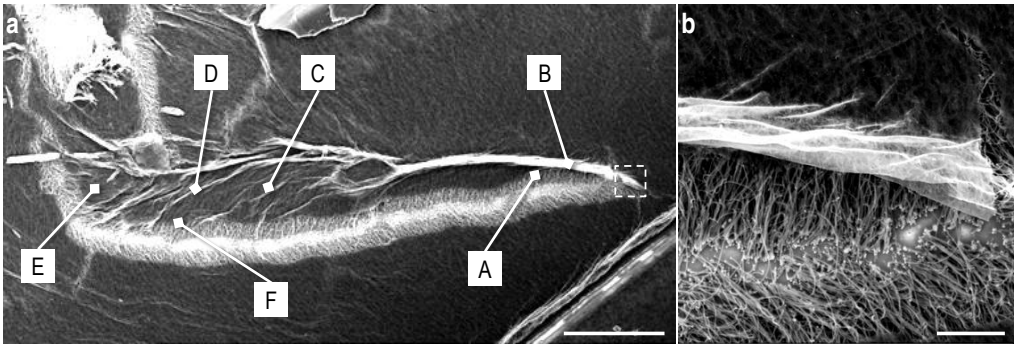

Figure 5.28: (a) SEM image of a crack on the composite material due to squashing. The letters make reference to the points where the Raman analyses were performed. (b) Detail of the folding of the top carbon layer. Scale bars are 5 µm and 1 µm in (a) and (b), respectively.

Figure 5.28 shows the squashed composite area that was selected for the Raman evaluation of the MWCNTs and the carbon top layer. Because of the squashing, the top layer had been ripped and a trench in the CNT layer had been formed (lower part of the squashed region) and, due to the CNTs lying on the surface of the sample, the top layer had folded (central and upper part of the squashed region). SEM image in Figure 5.28-b is a higher magnification SEM image of the folding of the carbon layer on the right hand side edge of the squashed region.

Marked in Figure 5.28-a positions (A-F) correspond to the areas from which the Raman spectra in Figure 5.29-a to Figure 5.29-f were compiled, respectively[§].

Three spectra, Figure 5.29-a, Figure 5.29-e and Figure 5.29-f, stand out of the others because the intensity of their G' peaks (~2,700 cm^{-1}) was much higher than that of their G peaks (~1,585 cm^{-1}).

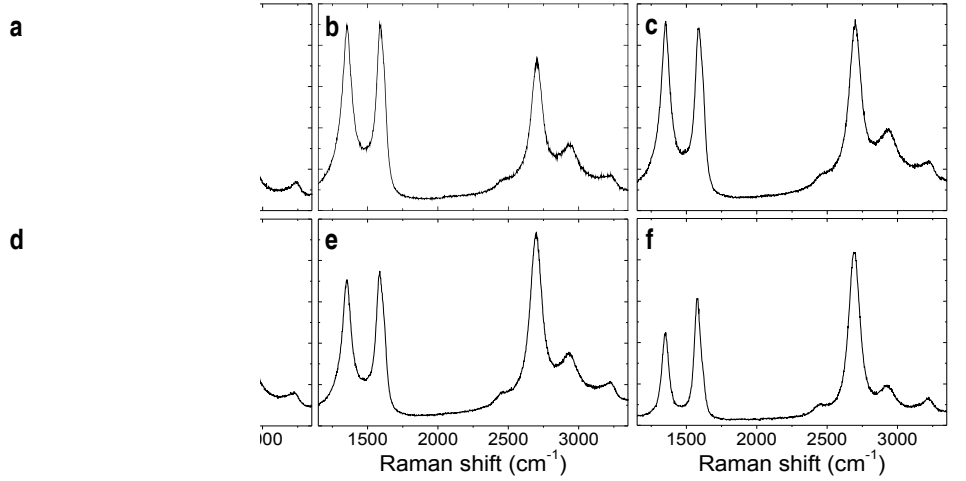

Figure 5.29: (a-f) Raman spectra of the areas labelled A-F in Figure 5.28 (a). Laser: 514.5 nm; X100; 0.4 mW.

§ Because of the optical maximal resolution of the microscope (X100 magnification) that is installed on the Raman system, a little displacement (some micrometres) from the point where the measurement was performed with respect to the marked in Figure 5.28-a positions is possible.

Position A was related to the folded top carbon layer on the laying on the surface MWCNTs (Figure 5.28-b) and positions E and F to the top carbon layer on the lying on the surface MWCNTs.

The relative intensity of the G' peak in the spectra for positions A, E and F cannot be related to the observation of SWCNT, MWCNT, HOPG, amorphous carbon, nor to graphite [76, 94]. The only Raman characteristic that matches with that in those spectra is that of graphene [68]. In particular, the Raman spectra could be attributed to a 1-layer graphene [107, 108] or to a 2-layer graphene where the layers are folded or arranged according to a disordered stacking [109]. These two possibilities match with the observation of a laying on the MWCNT layer graphene monolayer, or with the observation of a laying on a MWCNT layer folded (after squashing) graphene monolayer. More precise analyses on the frequency and the full width at half maximum (FWHM) of the peaks are not possible because of the lower MWCNT layer.

5.3.4 Conclusions and proposed growth mechanism for the MWCNT-graphene composite

This section has analysed the formation of a composite material formed of a vertically aligned MWCNT layer and of a top film that SEM, EDX, and Raman characterization of the samples have suggested being a graphene monolayer.

The synthesized composite is different from the CNT-multi-layer graphene composite reported in [104] in two aspects. First, in the present case, MWCNTs seemed to be in contact with the top layer but they do not seem to be part of it since is able to shift with respect to the CNT array (Figure 5.25-d). Second, the Raman characterization of the composite suggests the formation of a graphene monolayer instead of a graphene multi layer.

The fact that the composite material was observed for different catalyst layer thicknesses, for various substrate configurations and when applying CVD processes that had previously been validated for the synthesis of MWCNT arrays, suggests that the synthesis of the MWCNT-graphene composite is related to some synthesis parameter that is not perfectly controlled. If the substrate materials are excluded (since the composite was obtained for different substrate configurations), the composite formation has to be linked to some reaction related to the RTCVD process.

The graphene layer formation once the MWCNTs had started growing would not be possible as carbon would deposit to result in the growth of the MWCNTs or as amorphous carbon around them.

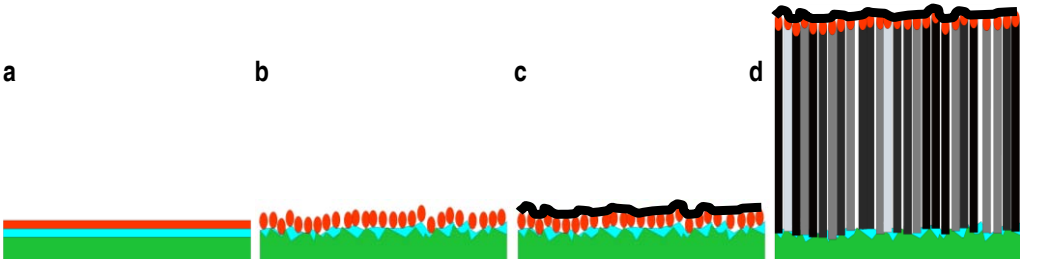

Figure 5.30: Schematic of the layer configuration and of the synthesis process. (a) Substrate configuration: the thin silicon oxide and the catalyst platinum layers are deposited on platinum or on a silicon oxide substrate. (b) Catalyst layer dewetting to form the catalyst islands during the catalyst activation step of the CNT synthesis process. (c) Formation of the graphene monolayer on top of the particles during the first stage of the CNT growth step. (d) Growth of the vertically aligned MWCNT layer during the second stage of the CNT growth step.

Therefore, its formation must take place before the growth of the MWCNTs. As the CNT growth step when using platinum layers as catalyst material is divided in two stages (section 5.2.2), it is most probable for the graphene to form at the first stage and, then, the dense MWCNTs layers to grow during the second stage. This way, the synthesis of dense arrays of vertically aligned MWCNTs could be favoured by a “kite” effect of the graphene layer on the MWCNTs similar to the ones reported in [105, 106]. A schematic of the proposed synthesis sequence is shown in Figure 5.30.

Although graphene synthesis by means of a CVD process and a metal catalyst such as cobalt, nickel or copper has already been reported [100-102, 104], these results are the first ones where graphene is obtained out of platinum. In addition, it is, up to the author knowledge, the first time that graphene is synthesised out of metal particles and not out of a continuous metal layer.

Chapter conclusions

This chapter has presented advances in the synthesis of CNTs from different in morphology catalyst materials based on platinum, which is a non-conventional CNT catalyst.

The first chapter has studied CNT synthesis out of two different structure platinum based particles: pure platinum particles and TEOS shelled platinum particles. This approach aimed to evaluate if the results that were obtained when using iron particle based catalyst materials could be reproduced when using these platinum particles.

- SW- and MWCNT synthesis was achieved when using the pure platinum particles. Control over the growth of neither SW -or MWCNT was achieved, most probably because of non-optimised catalyst deposition conditions. As the nominal diameter of the particles was less than 2 nm, it is supposed that the non-optimised catalyst deposition led to the formation of particle aggregates that, in turn, led to the synthesis of MWCNTs. Optimization of the deposition of the platinum particles should lead to a reproducible synthesis of SWCNTs.
- TEOS shelled platinum particles resulted, in all cases, in the formation of a platinum silicide. This reaction may not be avoided unless the synthesis of the CNTs is performed at temperatures below that of the platinum silicide formation.

The second section has studied the formation of dense arrays of CNTs on platinum substrates where the CNTs aligned perpendicular to the substrate. Developed tasks consisted in the optimization of a barrier to inhibit the diffusion of the catalyst layer into the substrate, in the optimization of the CNT synthesis parameters and in the analysis of the influence of the catalyst layer thickness on the CNT layer.

- Regarding the barrier, a deposited by PECVD 15 nm thick silicon oxide layer was demonstrated to prevent diffusion between the two platinum layers and to enhance the formation of the catalyst islands.
- High density of vertically aligned MWCNT layers were synthesised for platinum catalyst layers between 4 and 1 nm. When they were grown from the 4 nm thick platinum layers, the MWCNTs aligned vertically because of the formation of a top MWCNT crust. On the contrary, when the MWCNTs were grown from the 1 nm thick platinum layers, the MWCNTs aligned vertically because of very high MWCNT packaging.
- The modification of the catalyst activation step was demonstrated to be very valuable for the synthesis of different in structure MWCNTs and carbon fibres.

The third section has reported the synthesis of a CNT composite on some samples that were meant for the synthesis of arrays of vertically aligned MWCNTs.

- Different characterizations of the sample (SEM, EDX, and Raman spectroscopy) suggest that the top layer is a graphene monolayer.
- Although the formation of the composite has not been elucidated, a synthesis process has been proposed based on the RTCVD synthesis process steps.

In conclusion, attained results constitute a step forward to the synthesis of CNTs from non-conventional catalyst materials. The fact that success was attained on the synthesis of isolated SWCNTs as well as on the synthesis of very dense and vertically aligned MWCNT arrays, even on a

metallic substrate, demonstrates that platinum may be considered as a valuable material for CNT synthesis. In this sense, the recipes that have been developed in this chapter are used in Chapter 10 for the integration of vertically aligned arrays of MWCNTs into the metallic electrodes of devices for bio-sensing applications. Additionally, the observation of a new CNT-graphene composite is remarkable. Deducing the synthesis process of this composite could impulse its integration into devices and could elucidate the CNT and graphene synthesis mechanisms.

Outlook

This section on the synthesis of CNTs by RTCVD has overviewed the acquired expertise on the synthesis of SW and MWCNTs by iron, nickel and platinum based catalyst materials. The developed methods are used in the next sections for the integration of SWCNTs into single CNT devices and for the integration of dense arrays of vertically aligned MWCNTs into metal electrodes.

Two aspects must be emphasized over the rest respect the reported results. First, even if SWCNT synthesis from zeolites has not been fully optimised, the use of these crystals as catalyst supports may contribute to overcome the main challenges on SWCNT integration into one CNT devices. Second, the fact that platinum may be used as CNT catalyst material in a similar way to iron or nickel opens a range of possibilities for this metal to be used in applications where the conventional catalysts are forbidden. Some of these applications are devices for bio-sensing and catalysis. Apart from these accomplishments, the synthesis of the MWCNT-graphene monolayer composite has also to be highlighted as it could lead to the fabrication of novel device concepts.

However, even if the achievements have been many, there are still methods to be optimised. Regarding the synthesis of SWCNTs, the main objective would be to improve the synthesis of SWCNTs from zeolite-L crystals in order to achieve the total control on the density of SWCNTs that grow from each zeolite. Regarding the synthesis of dense CNT layers from platinum, the catalyst layer should be further optimised to achieve the synthesis of arrays of SWCNTs. In addition, the use of other CVD conditions, such as plasma, should be considered to grow bamboo like MWCNTs. Besides, a simple strategy to fabricate a barrier to inhibit the diffusion between the metal substrate and the CNT catalyst material and that, at the same time, would not hinder electric transfer, should also be addressed.

In summary, the bases for the integration of SWCNTs into single CNT devices and of dense MWCNTs layers have been established. These methods are used in the next chapters for the fabrication of SWCNT based CNT-FET and for the fabrication of MWCNT based electrodes.

References

1. R.T.K. Baker, Catalytic growth of carbon filaments, Carbon, 1989. **27**(3): p. 315-323.
2. A. Gohier, C.P. Ewels, T.M. Minea, and M.A. Djouadi, Carbon nanotube growth mechanism switches from tip- to base-growth with decreasing catalyst particle size, Carbon, 2008. **46**(10): p. 1331-1338.
3. S. Hofmann, R. Sharma, C. Ducati, G. Du, C. Mattevi, C. Cepek, M. Cantoro, S. Pisana, A. Parvez, F. Cervantes-Sodi, A.C. Ferrari, R. Dunin-Borkowski, S. Lizzit, L. Petaccia, A. Goldoni, and J. Robertson, In situ observations of catalyst dynamics during surface-bound carbon nanotube nucleation, Nano Letters, 2007. **7**(3): p. 602-608.
4. M. Lin, J.P.Y. Tan, C. Boothroyd, K.P. Loh, E.S. Tok, and Y.-L. Foo, Dynamical Observation of Bamboo-like Carbon Nanotube Growth, Nano Letters, 2007. **7**(8): p. 2234-2238.
5. M. Marchand, C. Journet, D. Guillot, J.-M. Benoit, B.I. Yakobson, and S.T. Purcell, Growing a Carbon Nanotube Atom by Atom: "And Yet It Does Turns", Nano Letters, 2009. **9**(8): p. 2961-2966.
6. F. Ding, A.R. Harutyunyan, and B.I. Yakobson, Dislocation theory of chirality-controlled nanotube growth, Proceedings of the National Academy of Sciences, 2009. **106**(8): p. 2506-2509.
7. X. Wang, W. Yue, M. He, M. Liu, J. Zhang, and Z. Liu, Bimetallic Catalysts for the Efficient Growth of SWNTs on Surfaces, Chemistry of Materials, 2004. **16**(5): p. 799-805.
8. C.J. Lee, J. Park, J.M. Kim, Y. Huh, J.Y. Lee, and K.S. No, Low-temperature growth of carbon nanotubes by thermal chemical vapor deposition using Pd, Cr, and Pt as co-catalyst, Chemical Physics Letters, 2000. **327**(5-6): p. 277-283.
9. S. Esconjauregui, C.M. Whelan, and K. Maex, The reasons why metals catalyze the nucleation and growth of carbon nanotubes and other carbon nanomorphologies, Carbon, 2009. **47**(3): p. 659-669.
10. D. Takagi, Y. Homma, H. Hibino, S. Suzuki, and Y. Kobayashi, Single-walled carbon nanotube growth from highly activated metal nanoparticles, Nano Letters, 2006. **6**(12): p. 2642-2645.
11. W. Zhou, Z. Han, J. Wang, Y. Zhang, Z. Jin, X. Sun, C. Yan, and Y. Li, Copper catalyzing growth of single-walled carbon nanotubes on substrates, Nano Letters, 2006. **6**(12): p. 2987-2990.
12. S. Bhaviripudi, E. Mile, S.A. Steiner, A.T. Zare, M.S. Dresselhaus, A.M. Belcher, and J. Kong, CVD Synthesis of Single-Walled Carbon Nanotubes from Gold Nanoparticle Catalysts, Journal of the American Chemical Society, 2007. **129**(6): p. 1516-1517.
13. D. Takagi, H. Hibino, S. Suzuki, Y. Kobayashi, and Y. Homma, Carbon nanotube growth from semiconductor nanoparticles, Nano Letters, 2007. **7**(8): p. 2272-2275.
14. S.A. Steiner Iii, T.F. Baumann, B.C. Bayer, R. Blume, M.A. Worsley, W.J. MoberlyChan, E.L. Shaw, R. Schlögl, A.J. Hart, S. Hofmann, and B.L. Wardle, Nanoscale zirconia as a nonmetallic

catalyst for graphitization of carbon and growth of single- and multiwall carbon nanotubes, Journal of the American Chemical Society, 2009. **131**(34): p. 12144-12154.

15. Y.S. Park, E.C. Choi, and B. Hong, Growth of carbon nanotubes using nanocrystalline carbon catalyst, Applied Surface Science, 2009. **255**(11): p. 6028-6032.

16. H. Liu, D. Takagi, H. Ohno, S. Chiashi, T. Chokan, and Y. Homma, Growth of single-walled carbon nanotubes from ceramic particles by alcohol chemical vapor deposition, Applied Physics Express, 2008. **1**(1): p. 014001.1 - 014001.3.

17. D. Takagi, Y. Kobayashi, and Y. Homma, Carbon nanotube growth from diamond, Journal of the American Chemical Society, 2009. **131**(20): p. 6922-6923.

18. Y. Yao, C. Feng, J. Zhang, and Z. Liu, "Cloning" of Single-Walled Carbon Nanotubes via Open-End Growth Mechanism, Nano Letters, 2009. **9**(4): p. 1673-1677.

19. H. Liu, D. Takagi, S. Chiashi, and Y. Homma, The growth of single-walled carbon nanotubes on a silica substrate without using a metal catalyst, Carbon, 2010. **48**(1): p. 114-122.

20. P. Serp, M. Corrias, and P. Kalck, Carbon nanotubes and nanofibers in catalysis, Applied Catalysis A: General, 2003. **253**(2): p. 337-358.

21. J. Kong, H.T. Soh, A.M. Cassell, C.F. Quate, and H.J. Dai, Synthesis of individual single-walled carbon nanotubes on patterned silicon wafers, Nature, 1998. **395**(6705): p. 878-881.

22. H. Cui, G. Eres, J.Y. Howe, A. Puretkzy, M. Varela, D.B. Geohegan, and D.H. Lowndes, Growth behavior of carbon nanotubes on multilayered metal catalyst film in chemical vapor deposition, Chemical Physics Letters, 2003. **374**(3-4): p. 222-228.

23. A. Javey and H.J. Dai, Regular arrays of 2 nm metal nanoparticles for deterministic synthesis of nanomaterials, Journal of the American Chemical Society, 2005. **127**(34): p. 11942-11943.

24. S. Hofmann, M. Cantoro, B. Kleinsorge, C. Casiraghi, A. Parvez, J. Robertson, and C. Ducati, Effects of catalyst film thickness on plasma-enhanced carbon nanotube growth, Journal of Applied Physics, 2005. **98**(3): p. 036101.1 - 036101.4.

25. M. Cantoro, S. Hofmann, S. Pisana, C. Ducati, A. Parvez, A.C. Ferrari, and J. Robertson, Effects of pre-treatment and plasma enhancement on chemical vapor deposition of carbon nanotubes from ultra-thin catalyst films, Diamond and Related Materials, 2006. **15**(4-8): p. 1029-1035.

26. S.S. Fan, M.G. Chapline, N.R. Franklin, T.W. Tombler, A.M. Cassell, and H.J. Dai, Self-oriented regular arrays of carbon nanotubes and their field emission properties, Science, 1999. **283**(5401): p. 512-514.

27. H. Ago, K. Murata, M. Yumura, J. Yotani, and S. Uemura, Ink-jet printing of nanoparticle catalyst for site-selective carbon nanotube growth, Applied Physics Letters, 2003. **82**(5): p. 811-813.

28. Y.S. Min, E.J. Bae, J.B. Park, and W. Park, Direct photolithographic route to selective growth of single-walled carbon nanotubes using a modified photoresist with ferrocene, Nanotechnology, 2006. **17**(1): p. 116-123.

29. K. Gjerde, T. Schurmann, I. Bu, K.B.K. Teo, W.I. Milne, and P. Boggild, Integration of carbon nanotubes with controllable inclination angle into microsystems, Carbon, 2006. **44**(14): p. 3030-3036.

30. K. Hata, D.N. Futaba, K. Mizuno, T. Namai, M. Yumura, and S. Iijima, Water-assisted highly efficient synthesis of impurity-free single-waited carbon nanotubes, Science, 2004. **306**(5700): p. 1362-1364.

31. G.Y. Zhang, D. Mann, L. Zhang, A. Javey, Y.M. Li, E. Yenilmez, Q. Wang, J.P. McVittie, Y. Nishi, J. Gibbons, and H.J. Dai, Ultra-high-yield growth of vertical single-walled carbon nanotubes: Hidden roles of hydrogen and oxygen, Proceedings of the National Academy of Sciences of the United States of America, 2005. **102**(45): p. 16141-16145.

32. A.R. Harutyunyan, G. Chen, T.M. Paronyan, E.M. Pigos, O.A. Kuznetsov, K. Hewaparakrama, S.M. Kim, D. Zakharov, E.A. Stach, and G.U. Sumanasekera, Preferential Growth of Single-Walled Carbon Nanotubes with Metallic Conductivity, Science, 2009. **326**(5949): p. 116-120.

33. L. Zhang, Z.R. Li, Y.Q. Tan, G. Lolli, N. Sakulchaicharoen, F.G. Requejo, B.S. Mun, and D.E. Resasco, Influence of a top crust of entangled nanotubes on the structure of vertically aligned forests of single-walled carbon nanotubes, Chemistry of Materials, 2006. **18**(23): p. 5624-5629.

34. S. Hofmann, B. Kleinsorge, C. Ducati, A.C. Ferrari, and J. Robertson, Low-temperature plasma enhanced chemical vapour deposition of carbon nanotubes, Diamond and Related Materials. **13**(4-8): p. 1171-1176.

35. W.H. Chiang. and R.M. Sankaran, Linking catalyst composition to chirality distributions of as-grown single-walled carbon nanotubes by tuning NixFe1-x nanoparticles, Nature Materials, 2009. **8**(11): p. 882-886.

36. S.M. Huang, X.Y. Cai, and J. Liu, Growth of millimeter-long and horizontally aligned single-walled carbon nanotubes on flat substrates, Journal of the American Chemical Society, 2003. **125**(19): p. 5636-5637.

37. Y.G. Zhang, A.L. Chang, J. Cao, Q. Wang, W. Kim, Y.M. Li, N. Morris, E. Yenilmez, J. Kong, and H.J. Dai, Electric-field-directed growth of aligned single-walled carbon nanotubes, Applied Physics Letters, 2001. **79**(19): p. 3155-3157.

38. J. Xiao, S. Dunham, P. Liu, Y. Zhang, C. Kocabas, L. Moh, Y. Huang, K.-C. Hwang, C. Lu, W. Huang, and J.A. Rogers, Alignment Controlled Growth of Single-Walled Carbon Nanotubes on Quartz Substrates, Nano Letters, 2009. **9**(12): p. 4311-4319.

39. C. Feng, Y. Yao, J. Zhang, and Z. Liu, Nanobarrier-terminated growth of single-walled carbon nanotubes on quartz surfaces, Nano Research, 2009. **2**(10): p. 768-773.

40. T. Kamimura and K. Matsumoto, Controlling Direction of Growth of Carbon Nanotubes on Patterned SiO_2 Substrate, Applied Physics Express, 2009. **2**(1): p. 015005.1 - 015005.3.

41. S.J. Wind, R. Martel, and P. Avouris. Localized and directed lateral growth of carbon nanotubes from a porous template. in Papers from the 46th International Conference on Electron, Ion, and Photon Beam Technology and Nanofabrication. 2002. Anaheim, California (USA): AVS.

42. M.S. Arnold, A.A. Green, J.F. Hulvat, S.I. Stupp, and M.C. Hersam, Sorting carbon nanotubes by electronic structure using density differentiation, Nature Nanotechnology, 2006. **1**(1): p. 60-65.

43. A. Vijayaraghavan, S. Blatt, D. Weissenberger, M. Oron-Carl, F. Hennrich, D. Gerthsen, H. Hahn, and R. Krupke, Ultra-Large-Scale Directed Assembly of Single-Walled Carbon Nanotube Devices, Nano Letters, 2007. **7**(6): p. 1556-1560.

44. J.H. Hafner, C.L. Cheung, T.H. Oosterkamp, and C.M. Lieber, High-yield assembly of individual single-walled carbon nanotube tips for scanning probe microscopies, Journal of Physical Chemistry B, 2001. **105**(4): p. 743-746.

45. A.M. Dean, Detailed Kinetic Modeling of Autocatalysis in Methane Pyrolysis, Journal of Physical Chemistry, 1990. **94**(4): p. 1432-1439.

46. L.X. Zheng, M.J. O'Connell, S.K. Doorn, X.Z. Liao, Y.H. Zhao, E.A. Akhadov, M.A. Hoffbauer, B.J. Roop, Q.X. Jia, R.C. Dye, D.E. Peterson, S.M. Huang, J. Liu, and Y.T. Zhu, Ultralong single-wall carbon nanotubes, Nature Materials, 2004. **3**(10): p. 673-676.

47. S.M. Huang, M. Woodson, R. Smalley, and J. Liu, Growth mechanism of oriented long single walled carbon nanotubes using "fast-heating" chemical vapor deposition process, Nano Letters, 2004. **4**(6): p. 1025-1028.

48. N.R. Franklin, Y.M. Li, R.J. Chen, A. Javey, and H.J. Dai, Patterned growth of single-walled carbon nanotubes on full 4-inch wafers, Applied Physics Letters, 2001. **79**(27): p. 4571-4573.

49. W. Wasel, K. Kuwana, P.T.A. Reilly, and K. Saito, Experimental characterization of the role of hydrogen in CVD synthesis of MWCNTs, Carbon, 2007. **45**(4): p. 833-838.

50. S.R.C. Vivekchand, A. Govindaraj, M.M. Seikh, and C.N.R. Rao, New method of purification of carbon nanotubes based on hydrogen treatment, Journal of Physical Chemistry B, 2004. **108**(22): p. 6935-6937.

51. A.R. Harutyunyan, B.K. Pradhan, U.J. Kim, G. Chen, and P.C. Eklund, CVD Synthesis of Single Wall Carbon Nanotubes under "Soft" Conditions, Nano Letters, 2002. **2**(5): p. 525-530.

52. A.C. Dupuis, The catalyst in the CCVD of carbon nanotubes-a review, Progress in Materials Science, 2005. **50**(8): p. 929-961.

53. E.F. Kukovitsky, S.G. L'vov, N.A. Sainov, V.A. Shustov, and L.A. Chernozatonskii, Correlation between metal catalyst particle size and carbon nanotube growth, Chemical Physics Letters, 2002. **355**(5-6): p. 497-503.

54. J.I. Sohn, C.J. Choi, S. Lee, and T.Y. Seong, Effects of Fe film thickness and pretreatments on the growth behaviours of carbon nanotubes on Fe-doped (001) Si substrates, Japanese Journal of Applied Physics Part 1-Regular Papers Short Notes & Review Papers, 2002. **41**(7A): p. 4731-4736.

55. A.A. Puretzky., D.B. Geohegan, S. Jesse, I.N. Ivanov, and G. Eres, In situ measurements and modeling of carbon nanotube array growth kinetics during chemical vapor deposition, Applied Physics a-Materials Science & Processing, 2005. **81**(2): p. 223-240.

56. J. Lacaze and B. Sundman, An Assessment of the Fe-C-Si System, Metallurgical Transactions a-Physical Metallurgy and Materials Science, 1991. **22**(10): p. 2211-2223.

57. H. Okumura, Present status and future prospect of widegap semiconductor high-power devices, Japanese Journal of Applied Physics, Part 1: Regular Papers and Short Notes and Review Papers, 2006. **45**(10 A): p. 7565-7586.

58. N.G. Wright, A.B. Horsfall, and K. Vassilevski, Prospects for SiC electronics and sensors, Materials Today, 2008. **11**(1-2): p. 16-21.

59. G.Q. Zhang, Y. Hashimoto, A. Nakamura, A. Tanaka, J. Temmyo, and Y. Matsui, Very thin single-walled carbon nanotubes self-assembled on 6H-SiC(0001) substrate by surface decomposition method, Japanese Journal of Applied Physics Part 2-Letters & Express Letters, 2007. **46**(1-3): p. L53-L56.

60. Y. Kobayashi, H. Nakashima, D. Takagi, and Y. Homma, CVD growth of single-walled carbon nanotubes using size-controlled nanoparticle catalyst, Thin Solid Films, 2004. **464-65**: p. 286-289.

61. S.H. Sun and H. Zeng, Size-controlled synthesis of magnetite nanoparticies, Journal of the American Chemical Society, 2002. **124**(28): p. 8204-8205.

62. A. Jorio, R. Saito, J.H. Hafner, C.M. Lieber, M. Hunter, T. McClure, G. Dresselhaus, and M.S. Dresselhaus, Structural (n, m) determination of isolated single-wall carbon nanotubes by resonant Raman scattering, Physical Review Letters, 2001. **86**(6): p. 1118-1121.

63. F. Tuinstra. and J.L. Koenig, Raman Spectrum of Graphite, Journal of Chemical Physics, 1970. **53**(3): p. 1126-1131.

64. Y.M. Li, W. Kim, Y.G. Zhang, M. Rolandi, D.W. Wang, and H.J. Dai, Growth of single-walled carbon nanotubes from discrete catalytic nanoparticles of various sizes, Journal of Physical Chemistry B, 2001. **105**(46): p. 11424-11431.

65. J.M. Bonard, P. Chauvin, and C. Klinke, Monodisperse Multiwall Carbon Nanotubes Obtained with Ferritin as Catalyst, Nano Letters, 2002. **2**(6): p. 665-667.

66. W. Kim, H.C. Choi, M. Shim, Y. Li, D. Wang, and H. Dai, Synthesis of Ultralong and High Percentage of Semiconducting Single-walled Carbon Nanotubes, Nano Letters, 2002. **2**(7): p. 703-708.

67. L. Durrer, T. Helbling, C. Zenger, A. Jungen, C. Stampfer, and C. Hierold, SWNT growth by CVD on Ferritin-based iron catalyst nanoparticles towards CNT sensors, Sensors and Actuators, B: Chemical, 2008. **132**(2): p. 485-490.

68. M.S. Dresselhaus, A. Jorio, M. Hofmann, G. Dresselhaus, and R. Saito, Perspectives on Carbon Nanotubes and Graphene Raman Spectroscopy, Nano Letters, 2010. **10**(3): p. 751-758.

69. C. Baerlocher, W.M. Meier, and D.H. Olson, *"Atlas of Zeolite Framework Type", 5th Edition*. 2001, Elsevier.

70. A. Corma, State of the art and future challenges of zeolites as catalysts, Journal of Catalysis, 2003. **216**(1-2): p. 298-312.

71. T. Hayashi, Y.A. Kim, T. Matoba, M. Esaka, K. Nishimura, T. Tsukada, M. Endo, and M.S. Dresselhaus, Smallest freestanding single-walled carbon nanotube, Nano Letters, 2003. **3**(7): p. 887-889.72. Lee, S.H., P.S. Alegaonkar, J.H. Han, A.S. Berdinsky, D. Fink, Y.U. Kwon, J.B. Yoo, and C.Y. Park, Carbon nanotubes growth in AlPO4-5 zeolites: Evidence for density dependent field emission characteristics, Diamond and Related Materials, 2006. **15**(10): p. 1759-1764.

73. N. Wang, Z.K. Tang, G.D. Li, and J.S. Chen, Single-walled 4 angstrom carbon nanotube arrays, Nature, 2000. **408**(6808): p. 50-51.

74. G.J. Yu, J.L. Gong, D.Z. Zhu, S.X. He, J.Q. Cao, and Z.Y. Zhu, Efficient synthesis of carbon nanotubes over rare earth zeolites by thermal chemical vapor deposition at low temperature, Diamond and Related Materials, 2006. **15**(9): p. 1261-1265.

75. J.M. Bennett, J.P. Cohen, E.M. Flanigen, J.J. Pluth, and J.V. Smith, Crystal-Structure of Tetrapropylammonium Hydroxide-Aluminum Phosphate Number-5, Acs Symposium Series, 1983. **218**: p. 109-118.

76. M.S. Dresselhaus, G. Dresselhaus, R. Saito, and A. Jorio, Raman spectroscopy of carbon nanotubes, Physics Reports-Review Section of Physics Letters, 2005. **409**(2): p. 47-99.

77. Z.K. Tang, N. Wang, X.X. Zhang, J.N. Wang, C.T. Chan, and P. Sheng, Novel properties of 0.4 nm single-walled carbon nanotubes templated in the channels of AlPO4-5 single crystals, New Journal of Physics, 2003. **5**: p. 146.1–146.29.

78. J.P. Zhai, Z.M. Li, H.J. Liu, I.L. Li, P. Sheng, X.J. Hu, and Z.K. Tang, Catalytic effect of metal cations on the formation of carbon nanotubes inside the channels of AlPO4-5 crystal, Carbon, 2006. **44**(7): p. 1151-1157.

79. R.M. Barrer and H. Villiger, Crystal Structure of Synthetic Zeolite L, Zeitschrift Fur Kristallographie Kristallgeometrie Kristallphysik Kristallchemie, 1969. **128**(3-6): p. 352-370.

80. C. Lan, P. Srisungsitthisunti, P.B. Amama, T.S. Fisher, X. Xu, and R.G. Reifenberger, Measurement of metal/carbon nanotube contact resistance by adjusting contact length using laser ablation, Nanotechnology, 2008. **19**(12): p. 125703.

81. C. Lan, D.N. Zakharov, and R.G. Reifenberger, Determining the optimal contact length for a metal/multiwalled carbon nanotube interconnect, Applied Physics Letters, 2008. **92**(21): p. 213112.1 - 213112.3.

82. F.F. Zhao, J.Z. Zheng, Z.X. Shen, T. Osipowicz, W.Z. Gao, and L.H. Chan, Thermal stability study of NiSi and NiSi2 thin films, Microelectronic Engineering, 2004. **71**(1): p. 104-111.

83. S. Esconjauregui, C.M. Whelan, and K. Maex, Carbon nanotube catalysis by metal silicide: Resolving inhibition versus growth, Nanotechnology, 2007. **18**(1): p. 015602.1 - 015602.11.

84. C. Kumpf, R. Nicula, and E. Burkel, Growth and Structure of Thin Pt_2Si and PtSi Layers on Si(111) and (001) Characterized with *In Situ* Grazing Incidence Diffraction, Journal of Applied Crystallography, 1997. **30**(6): p. 1016-1021.

85. C.-A. Chang and A. Segmuller, PtSi contact metallurgy formed by three-temperature annealing sequences and short annealing time, Journal of Applied Physics, 1987. **61**(1): p. 201-205.

86. P. Botella, A. Corma, and M.T. Navarro, Single Gold Nanoparticles Encapsulated in Monodispersed Regular Spheres of Mesostructured Silica Produced by Pseudomorphic Transformation, Chemistry of Materials, 2007. **19**(8): p. 1979-1983.

87. J.C. Tsang, Y. Yokota, R. Matz, and G. Rubloff, Raman-spectroscopy of PtSi formation at the Pt/Si(100) interface, Applied Physics Letters, 1984. **44**(4): p. 430-432.

88. G. Gabriel, I. Erill, J. Caro, R. Gómez, D. Riera, R. Villa, and P. Godignon, Manufacturing and full characterization of silicon carbide-based multi-sensor micro-probes for biomedical applications, Microelectronics Journal, 2007. **38**(3): p. 406-415.

89. G. Gabriel, R. Gómez, M. Bongard, N. Benito, E. Fernández, and R. Villa, Easily made single-walled carbon nanotube surface microelectrodes for neuronal applications, Biosensors and Bioelectronics, 2009. **24**(7): p. 1942-1948.

90. F. Javier del Campo, J. Garcia-Cespedes, F. Xavier Munoz, and E. Bertran, Vertically aligned carbon nanotube based electrodes: Fabrication, characterisation and prospects, Electrochemistry Communications, 2008. **10**(9): p. 1242-1245.

91. M. Chhowalla, K.B.K. Teo, C. Ducati, N.L. Rupesinghe, G.A.J. Amaratunga, A.C. Ferrari, D. Roy, J. Robertson, and W.I. Milne, Growth process conditions of vertically aligned carbon nanotubes using plasma enhanced chemical vapor deposition, Journal of Applied Physics, 2001. **90**(10): p. 5308-5317.

92. S. Hofmann, M. Cantoro, B. Kleinsorge, C. Casiraghi, A. Parvez, J. Robertson, and C. Ducati, Effects of catalyst film thickness on plasma-enhanced carbon nanotube growth, Journal of Applied Physics, 2005. **98**(3): p. 034308.1 - 034308.8.

93. L. Zhang, Y.Q. Tan, and D.E. Resasco, Controlling the growth of vertically oriented single-walled carbon nanotubes by varying the density of Co-Mo catalyst particles, Chemical Physics Letters, 2006. **422**(1-3): p. 198-203.

94. E.F. Antunes, A.O. Lobo, E.J. Corat, V.J. Trava-Airoldi, A.A. Martin, and C. Verissimo, Comparative study of first- and second-order Raman spectra of MWCNT at visible and infrared laser excitation, Carbon, 2006. **44**(11): p. 2202-2211.

95. E.F. Antunes, A.O. Lobo, E.J. Corat, and V.J. Trava-Airoldi, Influence of diameter in the Raman spectra of aligned multi-walled carbon nanotubes, Carbon, 2007. **45**(5): p. 913-921.

96. H. Nii, Y. Sumiyama, H. Nakagawa, and A. Kunishige, Influence of diameter on the Raman spectra of multi-walled carbon nanotubes, Applied Physics Express, 2008. **1**(6): p. 0640051-0640053.

97. R.A. DiLeo, B.J. Landi, and R.P. Raffaelle, Purity assessment of multiwalled carbon nanotubes by Raman spectroscopy, Journal of Applied Physics, 2007. **101**(6): p. 064307.1 - 064307.5.

98. D. Takagi, Y. Kobayashi, H. Hibino, S. Suzuki, and Y. Homma, Mechanism of gold-catalyzed carbon material growth, Nano Letters, 2008. **8**(3): p. 832-835.

99. K.S. Novoselov, A.K. Geim, S.V. Morozov, D. Jiang, Y. Zhang, S.V. Dubonos, I.V. Grigorieva, and A.A. Firsov, Electric field in atomically thin carbon films, Science, 2004. **306**(5696): p. 666-669.

100. A. Reina, X. Jia, J. Ho, D. Nezich, H. Son, V. Bulovic, M.S. Dresselhaus, and J. Kong, Large Area, Few-Layer Graphene Films on Arbitrary Substrates by Chemical Vapor Deposition, Nano Letters, 2008. **9**(1): p. 30-35.

101. K.S. Kim, Y. Zhao, H. Jang, S.Y. Lee, J.M. Kim, K.S. Kim, J.-H. Ahn, P. Kim, J.-Y. Choi, and B.H. Hong, Large-scale pattern growth of graphene films for stretchable transparent electrodes, Nature, 2009. **457**(7230): p. 706-710.

102. X. Li, W. Cai, J. An, S. Kim, J. Nah, D. Yang, R. Piner, A. Velamakanni, I. Jung, E. Tutuc, S.K. Banerjee, L. Colombo, and R.S. Ruoff, Large-Area Synthesis of High-Quality and Uniform Graphene Films on Copper Foils, Science, 2009. **324**(5932): p. 1312-1314.

103. Y.M. Lin, C. Dimitrakopoulos, K.A. Jenkins, D.B. Farmer, H.Y. Chiu, A. Grill, and P. Avouris, 100-GHz Transistors from Wafer-Scale Epitaxial Graphene, Science, 2010. **327**(5966): p. 662.

104. D. Kondo, S. Sato, and Y. Awano, Self-organization of novel carbon composite structure: Graphene multi-layers combined perpendicularly with aligned carbon nanotubes, Applied Physics Express, 2008. **1**(7): p. 0740031-0740033.

105. C.L. Pint, N.T. Alvarez, and R.H. Hauge, Odako growth of dense arrays of single-walled carbon nanotubes attached to carbon surfaces, Nano Research, 2009. **2**(7): p. 526-534.

106. Z. Chen, J. Merikhi, I. Koehler, and P.K. Bachmann, Sandwich growth of carbon nanotubes, Diamond and Related Materials, 2006. **15**(1): p. 104-108.

107. A.C. Ferrari, J.C. Meyer, V. Scardaci, C. Casiraghi, M. Lazzeri, F. Mauri, S. Piscanec, D. Jiang, K.S. Novoselov, S. Roth, and A.K. Geim, Raman spectrum of graphene and graphene layers, Physical Review Letters, 2006. **97**(18).

108. J.S. Park, A. Reina, R. Saito, J. Kong, G. Dresselhaus, and M.S. Dresselhaus, G' band Raman spectra of single, double and triple layer graphene, Carbon, 2009. **47**(5): p. 1303-1310.

109. Z. Ni, Y. Wang, T. Yu, Y. You, and Z. Shen, Reduction of Fermi velocity in folded graphene observed by resonance Raman spectroscopy, Physical Review B - Condensed Matter and Materials Physics, 2008. **77**(23): p. 235403.1 - 235403.5.